DEVELOPMENT OF A CARBON NANOTUBE FIELD EMISSION BASED MICROBEAM CELLULAR IRRADIATOR

David E. Bordelon

A dissertation submitted to the faculty of the University of North Carolina at Chapel Hill in partial fulfillment of the requirements for the degree of Doctor of Philosophy in the Curriculum in Applied Sciences and Engineering.

Chapel Hill
2009

Approved by

Advisor: Otto Zhou

Reader: Sha Chang

Reader: Adrienne Cox

Reader: René Lopez

Reader: Sean Washburn

ABSTRACT

DAVID BORDELON: Development Of A Carbon Nanotube Field Emission Based Microbeam Cellular Irradiator

(Under the direction of Otto Zhou)

Microbeam irradiation has been a growing area of interest in recent years. Microbeam techniques provide radiobiology researchers with the capability of irradiating cells and even subcellular regions with precise doses over precise time intervals. A variety of systems exist using beams of various ions, X-rays, as well as electrons. Multiple locations are irradiated by scanning the particle or photon beam or by translating the cell targets over the beam. While each of these has its own advantages no one has yet demonstrated a multi-beam system, which could increase experimental efficiency and versatility.

We have been working to develop a carbon nanotube (CNT) based multi-pixel cellular irradiator to demonstrate this as yet unfulfilled possibility. Formation of the microbeam via carbon nanotube field emission represents a great advantage in that the beam generation can take place in a compact area, has significant advantages over thermionic electron generation, and is readily scaleable using microfabrication methods. Use of CNT based electron field emission along with other microfabrication techniques will readily facilitate the development of a multi-pixel system and allows for a greater degree of miniaturization as compared to other systems, particularly those based on particle accelerators.

The CNT based system provides reliable, controllable electron beams with excellent dose rate capabilities. With the potential for smaller, more accessible systems this project

demonstrates a development that could make microbeam irradiation available to a broader group of scientists, accelerating the growth of knowledge about the effects and use of radiation on cells and the human body.

To Anna

ACKNOWLEDGEMENTS

It is with great gratitude that I approach the completion of this degree for the many people who have supported and encouraged me throughout this process. While an advanced degree demonstrates, to a measure, the ability to do independent research it is even more so the case that I have learned the importance of working with, gleaning from, and relying on others throughout the process.

First off I would like to thank my advisor, Dr. Otto Zhou, for giving me the opportunity, despite my advanced age, to work in his lab as a graduate student. I have greatly appreciated Dr. Zhou's scientific mentorship and his steady and patient personal demeanor both of which have been instrumental in seeing me through my research.

I would also like to thank Dr. Sha Chang who, as the Principal Investigator on my project, made this research possible by developing ideas and funds to see it and me move forward. Both Drs. Zhou and Chang have been greatly generous throughout this process.

Also I would like to thank my other committee members who reviewed the work at various times: Dr. Adrienne Cox, Dr. Sean Washburn, Dr. Lu-Chang Qin, and Dr. Rene-Lopez, in particular to Dr. Cox for her collaboration enabling the cell irradiation studies to demonstrate the system's capabilities and to Dr. Cox and Dr. Washburn for their thorough and helpful feedback on my manuscript. And thanks to Dr. Tom Clegg for useful discussions regarding the high voltage system.

I have also been extremely grateful for my fellow members of the Zhou research group. Thanks to Soojin Oh, Huaizhi Geng, Peng Wang, Guang Yang who all went ahead of me and helped show me the way. And thanks to Ramya Rajaram, Rui Peng, Xiomara Calderon-Colon, Matthew McIntosh, Shabana Sultana, and Tuyen Phan for walking with me as fellow students through this process and to my office mates for putting up with me and for making life in the office both comfortable and fun. Thanks to the post-docs in our lab, Lei An, Sigen Wang, Guohua Cao, and Xin Qian, who have lent their experience and friendship to me over these past several years. And many thanks to Christy Redmon for being a friend and sounding board and for keeping so many things in our group from spinning out of control! Finally many, many thanks to Jian "Jerry" Zhang for your friendship, co-labor, and leadership as we worked together to see this project realized. I would not have made it without your encouragement and guidance. I wish each of you great success and joy in life.

Thanks to those in Radiobiology and Radiation Oncology for their collaboration. To Eric Schrieber for the completion of helpful simulations and to Sarah Graboski and Jared Snider for their excellent and enthusiastic work in carrying out the cell culture, irradiation, and fluorescence work.

Thanks to the Physics and Applied Science administrative staff, Carolyn, Beverly, Sally, Jean, Cassandra, Leslie, Donna, and others, doing the behind the scenes work to keep

everything running smoothly. And to Phil, Steve, Cliff, and Neal in the machine shop, thanks for keeping it down to earth and for your patience and diligence in making many essential components for our system. Thanks to J.P Alarie for the use of the dicing saw and to Carrie Donley and Tina Stacy at CHANL for establishing and making available equipment critical to our project. And a special thanks to Tina for the many hours of assistance with the DRIE and SEM which allowed me to get such great results.

Additionally this research would not have been possible with the financial support of the NIH and the North Carolina Biotechnology Center.

I must also thank my family and friends who have supported me through this process. To my amazing wife Anna, thank you for your love, encouragement, and patience in allowing me to see this through, for being willing to marry a poor graduate student, and for delivering the best graduation present ever, our beautiful son, Zachary. I love you and hope that this degree will bring good things for our nascent family.

To my father, John Bordelon, thanks for instilling in me a love for wisdom and the knowledge of things both divine and mundane and for inspiring me to do this by getting your own degree at an even more advanced age. In those ways in which my life has been patterned after yours I have not gone wrong. To my mom, Carole Bordelon, thanks for praying for me and leading me to life at UNC many years ago. It was my dream to finish undergrad at UNC; little did I know that it would become my home for so many years and that a second degree from our alma mater would be in my future. To Tommy, Amber, Jenny, Jon, Harry, Grace, Cindy, and Jon thanks for your support, prayers, and patience.

I am also indebted to a great fellowship of friends in Christ who have made my time at UNC and in the Triangle a great pleasure. Thanks to Doug and Rachel, Jeff S., Brent and Amber, Chot and Katie, Dr. Keita Ikeda, Ross and Cathy, Pat and Brenda, Jacob L., Scott K., Amin A., Grant and Nancy, The Monks, Bob and Bonnie, John and Alison, Bryon and Betsy, Charles and Jamie, David and Christina, and many others at Church of the Good Shepherd. I am grateful for your friendship, encouragement, and prayers and will recall fondly for many years shared meals, trips, hilarity, co-labor, and time spent with each of you. Thanks to each of you for your walk of faith and for the ways in which you have made my life here so rich. If Anna and I ever return to the Triangle it pains me to think of any of you not being there. A special thanks to Doug, Brent, Keita, Bryon and other fellow science geeks who helped me maintain perspective.

Finally I am grateful to God for his grace in Jesus Christ that has been poured out on me in so many ways, in being able to complete this work, through the support of the people mentioned here, in the blessings of a new family. He is truly, “The Lord, the compassionate and gracious God, slow to anger and abounding in love and faithfulness” Exodus 34:6. He also allows me to make sense of the world around me both in faith and in science. Rather than abandon one or divorce the two He allows their integration. As Pascal said “Faith certainly tells us what the senses do not, but not the contrary of what they see; it is above, not against them” or in the words of Paul to the Romans, “For since the creation of the world God’s invisible qualities—his eternal power and divine nature—have been clearly seen, being understood from what has been made, so that men are without excuse.”

TABLE OF CONTENTS

CHAPTER ONE

MICROBEAM CELLULAR IRRADIATION

The human body is regularly exposed to ionizing radiation from a variety of sources. Cosmic rays bombard the body from outer space, while radioactive isotopes from terrestrial sources, such as radon, can also be a source of unwanted exposure. In other cases concentrated or mined radioactive materials are used in experiments or for commercial purposes, requiring extra precautions for those performing the experiments.

And while some exposures are unintentional, other exposures to ionizing radiation are done purposefully. Linear Accelerator systems are commonly used to expose the body to energetic photons and electrons for therapeutic purposes, such as the treatment of cancerous tumors (Fig. 1.1). And for imaging purposes X-rays are routinely used in a variety of techniques, such as the standard radiograph as well as CT imaging. Irradiation

Figure 1.1: Cut-away Schematic of Linear Accelerator for radiation therapy; Modern Computed Tomography system for diagnostic imaging (courtesy of Siemens; www.medical.siemens.com)

can also take place by other fundamental particles, such as neutrons or protons, in some cases therapeutic. And radioactive isotopes are also used in clinical settings, whether radioactive seeds implanted for brachytherapy of prostate cancer or short-lived isotopes generated for use in Positron Emission Tomography.

1.1 Biological Effects of Radiation

As one might infer from their use in therapeutic techniques, these energetic photons, particles, and isotopes can have a significant effect on cells and tissues. As these forms of ionizing radiation interact with matter generally, and more specifically with organic matter, changes take place as a result of the energy that is deposited there.

A desire for a greater understanding of the effects of ionizing radiation on the body, by itself, provides motivation for the development of new tools to investigate the intracellular and intercellular processes that take place following exposure. Following radiation exposure cells may be observed to initiate repair processes or on the other extreme become apoptotic. Further motivation lies in the possibility that greater knowledge of these processes can lead to improvements, for example, in the treatment of cancer by radiation or conversely in the understanding of the effects of radiation exposure on oncogenesis. Cancer outcome data show that there is still room for improvement in the treatment of cancer. While death rates for several types of cancer have shown steady but moderate decline none of the major technological improvements in cancer evaluation and therapy seem to have brought about large increases in life expectancy or large decreases in mortality (Figure 1.2). Investigation into these cellular processes in conjunction with radiation could generate a greater understanding of their operation and lead to greater improvement in therapeutic outcomes.

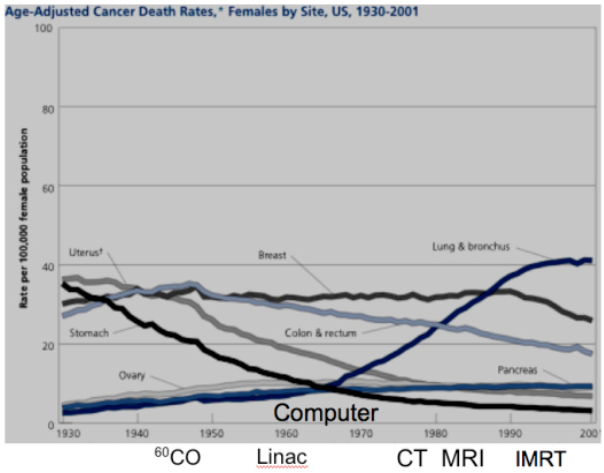

Figure 1.2: Age adjusted cancer death rate of US women from 1930 to 2001,with the major development of cancer diagnosis and treatment technologies indicated. Reproduced from the American Cancer Society, www.cancer.org.

1.2 Microbeam Irradiation

One area of research which is designed to facilitate increased study and knowledge in this area is that of microbeam irradiation. Cells can be readily irradiated by a number of means, such as a Cesium irradiator (Figure1.3). In the case of most Cesium irradiators the intention is to broadly irradiate an entire sample dish of cells. By this means the effects of irradiation on an entire population of cells can be studied. Microbeam techniques, on the other hand allow for selective photon or particle irradiation over areas measured in micron diameters.

Figure 1.3: J.L. Shepherd Mark 1 Model 30 Cesium Irradiator for irradiation of biological samples. Reproduced from: http://www.immunology.umn.edu/

Cells and even sub-cellular components can be targeted and irradiated with great selectivity giving microbeam systems unprecedented spatial irradiation control. Examples of these types of experiments could include the irradiation of every nucleus within a population, irradiation of the cytoplasm of a group of cells, and as in Figure 1.4 the irradiation of a single

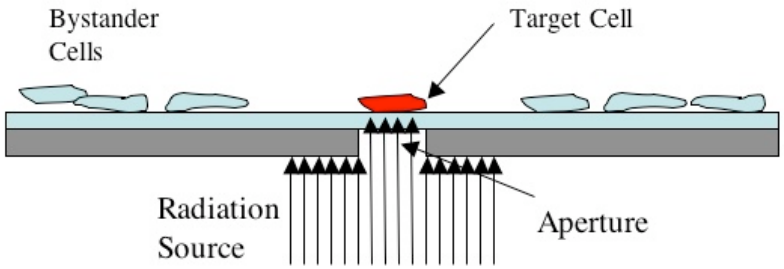

Figure 1.4: Schematic of Single-cell Microbeam Irradiation via small aperture. A small aperture allows radiation to be selectively applied to particular cells with the neighboring (bystander) cells receiving no direct exposure. The material in which the aperture is formed is opaque to the radiation source, whether photons or particles, preventing irradiation of adjacent structures.

cell within a population[1]. And while other irradiation techniques may also have excellent temporal and dosimetric accuracy, combining time and dose control with spatial control adds a new layer to those capabilities. Targeted cells can be irradiated at specific times relative to

one another, dose rate can be controlled, the dose can be delivered in pulses spread out over various time intervals, and dose can be applied to a particular cell while avoiding dose deposition in a neighboring cell.[2]

1.2.1 Cellular Response To Radiation

It is hoped that microbeam research will bring about a greater understanding of the responses of cells and tissues to ionizing radiation given their unique capabilities. These cellular responses could conceivably be apoptotic or possibly protective. Figure 1.5 graphically represents several of the possible effects of radiation on groups of cells. As can be seen the damage to cellular structures can be direct or indirect and the final effect on cells can also be direct or indirect. Whatever the post irradiation outcome, studying cellular response could shed light on intracellular damage and repair that takes place as well as the intercellular communication processes that may occur following radiation deposition.

One response of particular interest is the so-called bystander response. Studies of the bystander response attempt to measure radiation effects in the unirradiated neighbors of irradiated cells (Figure 1.6). Previous experiments point to two main means by which irradiated cells communicate with neighboring cells: via secreted soluble factors and via gap junction communication[3]. For experiments performed in cultured cell monolayers a higher bystander response has been observed, as might be expected, in cells with higher packing density. Data exists showing a bystander effect at distances up to 1 mm away. Nevertheless for both of these experimental motifs microbeams are currently the best technology for investigating these effects as a result of their high spatial resolution in irradiation.

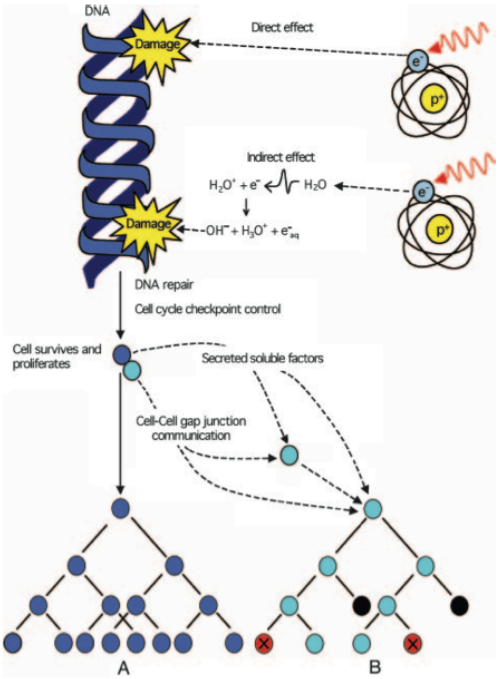

Fig. 1.5: Ionizing radiation induces direct DNA damage and indirect damage through the radiolysis of water. This damage is either eliminated or fixed in the cell as a mutation or chromosomal rearrangement by DNA repair processes. After release by cell cycle checkpoint control mechanisms, an irradiated surviving cell (blue) may proliferate, passing on the legacy of radiation to its progeny (diagram A), potentially initiating the carcinogenic process. The irradiated cell (blue) can also communicate with nonirradiated neighboring cells (cyan) by cell-to-cell gap junction communication and eliciting nontargeted apoptosis (black) or micronucleation (red) in cells that have never been exposed to radiation (diagram B). Reproduced from reference [4]

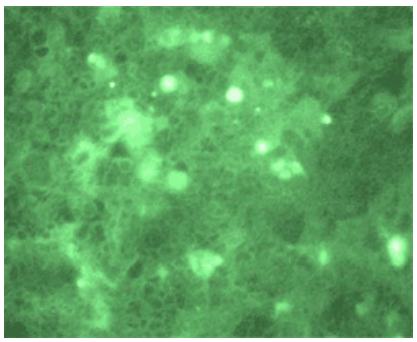

Figure 1.6: Cellular example of the Bystander Response. Bright regions in the image show increased oxidative activity in multiple human colon cancer cells whereas only a single cell near the center of the image was targeted with protons. http://www.gci.ac.uk/research/rad_science.htm

1.2.2 History of Cell Irradiation

Cell irradiation history goes back to as early as the 1930s. One early technique was to focus UV light into a micron scale beam to be used in cell irradiation; in some cases this is still performed today. Other techniques utilized higher energy radiation[5]. Many of these techniques were limited in that it was difficult to direct the beam to specific sites of a cell or to a particular cell. In some cases the technique relied on the utilization of particularly large cells.

In 1953 Zirkle and Bloom published a paper recording the first cell irradiation that would be considered a microbeam by current standards. Zirkle constructed a microbeam from a 2 MeV Van de Graff accelerator proton beam which he was able to collimate to 2.5

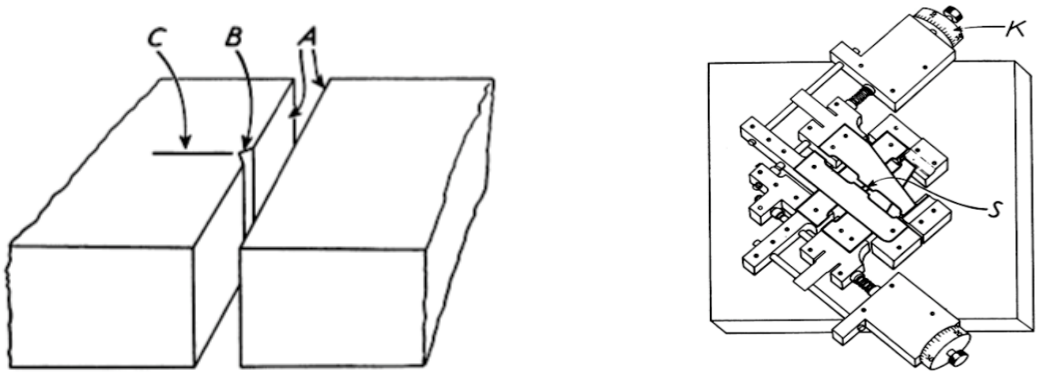

Figure 1.7: Two types of collimators mechanisms designed and utilized by Zirkle and Bloom: (a) optically flat metal blocks are joined, one having a mechanically formed V-groove (b) pairs of adjustable crossed slits with optically flat surfaces, with 0.5 um to 5mm openings. Reproduced from reference [5]

um in diameter. Although the accelerator was also capable of producing alpha particles Zirkle chose the proton output as the alpha particles were more easily stopped by the mica windows through which the beam was extracted into air from the vacuum. Collimation was

achieved by two different means (Fig. 1.7). Optically flat metal blocks, one with a mechanically formed V-groove, were joined to form a triangular collimator for the protons. Another version consisted of two micrometer-adjustable crossed slits with an opening range of 0.5um to 5mm. Each face of each slit was also optically flat and the two slits were aligned orthogonally to form a microbeam collimator.

Zirkle's system lacked the digital imaging capabilities and software which have helped to facilitate the resurgence in microbeams in the recent past. Nevertheless he was able to image cells using standard light microscopy and was able to take 16mm film of cells progressing through mitosis following irradiation. Figure 1.8 depicts the results of one such experiment performed in a culture of amphibian heart cells. In these images the

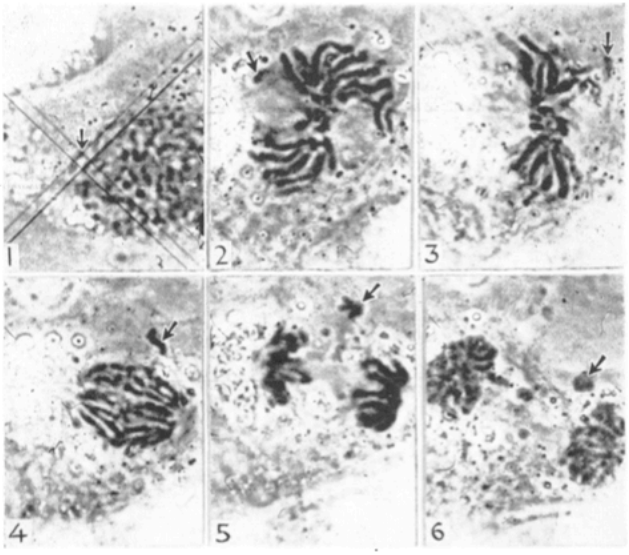

Figure 1.8: Development of an accessory nucleus. (Prints from 16-mm motion-picture film.) (1) Bombardment (arrow). (2) Position of bombarded chromosomes (arrow) in early metaphase. (3-5) A chromatin clump consisting of one or more chromosomes (arrows) is detached from the rest of the chromosome group. (6) Membrane (arrow) has formed around this clump. Two other accessory nuclei lie between the two large nuclei. (Area shown in each frame is 45 x 60 um.) Reproduced from reference [5]

chromosomes of a cell entering metaphase are bombarded by protons. As the cell progresses through mitosis the irradiated area proceeds to break away from the other chromosomes

forming an “accessory nucleus”. Similar effects were observed in irradiated cells with unirradiated cells exhibiting few of these abnormalities. Zirkle’s results demonstrated that microirradiation effects could easily be generated and that cellular processes could be studied using these special techniques.

Since the advent of early microbeams like this a large variety of microbeams have been developed and are being used in the United States, Europe, and Asia. This development has taken place particularly over the past ten years (Figure 1.9) and has seen an approximately ten fold increase over that time period. Among the many facilities that now

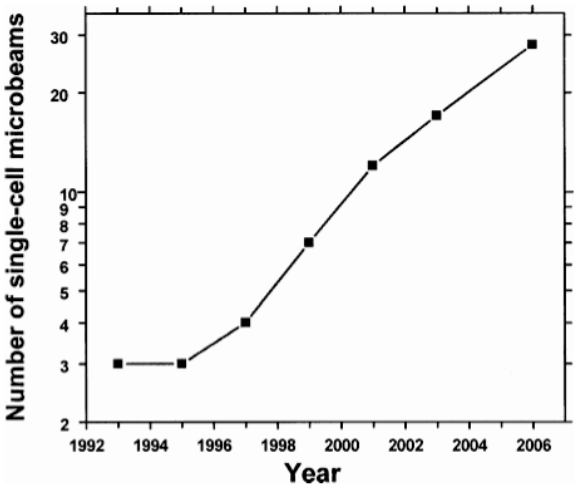

Figure 1.9: Number of single-cell microbeams, operational or under development, reported at past international microbeam workshops. Reproduced from [6]

exist the main microbeam methodologies are charged particle irradiation, X-ray irradiation, and electron irradiation [7-10]. A regular meting, the International Workshop: Microbeam Probes of Cellular Radiation Response, is held approximately every two and half years to bring together those working in the field of cellular irradiation. The most recent advances in microbeam technology and microbeam radiobiology experimentation are discussed.

1.3 Current Microbeam Technology

Given the proved usefulness as well as the potential usefulness of microbeam irradiation, as we consider the development of a new type of microbeam system it is necessary that we evaluate the current state of microbeam research. In this section we examine some of the more advanced microbeam systems based on charged particles, X-rays and electrons. Each has their own advantages and disadvantages, and their current capabilities will inform our development process.

1.3.1 Charged Particle Microbeams

Charged particle irradiators utilize a particle accelerator to create beams of alpha particles, protons, or in other cases heavier charged particles (O, F, C, Ne, Ar, Xe, Au)[6]. The use of an accelerator allows for a wide variety of particles to be used at very high energy. Heavy particle irradiation also typically has high linear energy transfer (LET) because of the size and mass of the elemental atoms. Collisions with other nuclei or electron interactions in a typical plated cell monolayer are much more likely when compared with many photon beams. In this way most of the energy of the particle is transferred to the target cell over a relatively short distance.

Two facilities that have utilized charged particle microbeams and that have been extremely prolific in microbeam research are the Gray Cancer Institute in the United Kingdom and the Columbia University Radiological Research Accelerator Facility (RARAF)[6].

The most recent work in developing modern particle based microbeams began in the 1990s[8, 11], and the microbeam at the Gray Cancer Institute (GCI) was one of the earliest accelerator based systems developed. Using a 4 MV Van de Graff accelerator GCI produces beams of $^{3}He^{2+}$ alpha particles as well as protons for cellular irradiation (Figure 1.10). The beam is collimated using a fused silica capillary with an inner diameter bore of 1 um, which is placed at the end of the beamline. The target cell dish is placed near the tip of the capillary collimator. Distance between the tip of the capillary and the cell dish is minimized in order to reduce scatter. Beam particles are then able to strike the target cells with high accuracy.

The GCI system also has full computer control of the beam shuttering, particle counting, and cell dish positioning instrumentation. With these components integrated together irradiation rates of up to 10,000 cells per hour are possible. Large experimental sample sizes of cells allow for the potential observation and statistical relevance of effects whose occurrence is only observed in a small fraction of cells. Figure 1.10 shows a schematic of the GCI microbeam components.

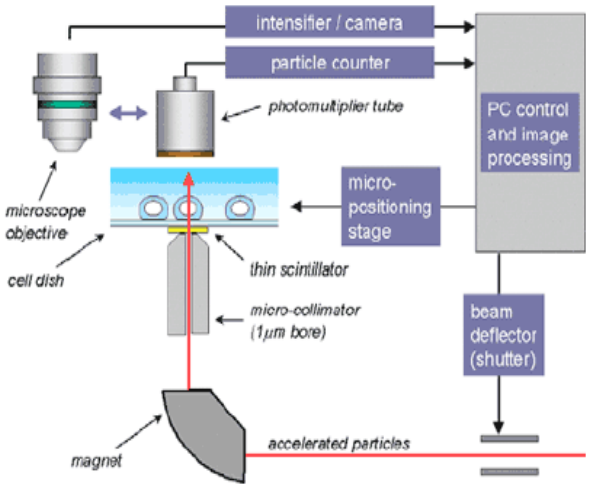

Figure 1.10: Schematic illustration of the 4 MV Van de Graff GCI microprobe irradiation system. Reproduced from http://www.gci.ac.uk/research/rad_science.htm.

Another example is the Columbia University Radiological Research Accelerator Facility (RARAF) particle microbeam. It is also one of the oldest and most used cell irradiation systems in existence today. The original system consisted of a 4.2 MV Van de Graff accelerator used to produce beams of H and He ions with an LET range of 30 to 220 keV/um. This system was predominantly used to generate a 6 MeV alpha particle beam. This system used a collimator formed from two ~5um laser drilled apertures separated by a 300um spacer, providing an ~60:1 aspect ratio.[2]

The system has been updated by replacing the old accelerator with a new 5 MV accelerator (Figure 1.11). This newer system provides higher voltage and acceleration energy with a lower noise voltage ripple resulting in a more steady beam[12]. The beam in this case is not physically collimated, but uses an electrostatic focusing method consisting of

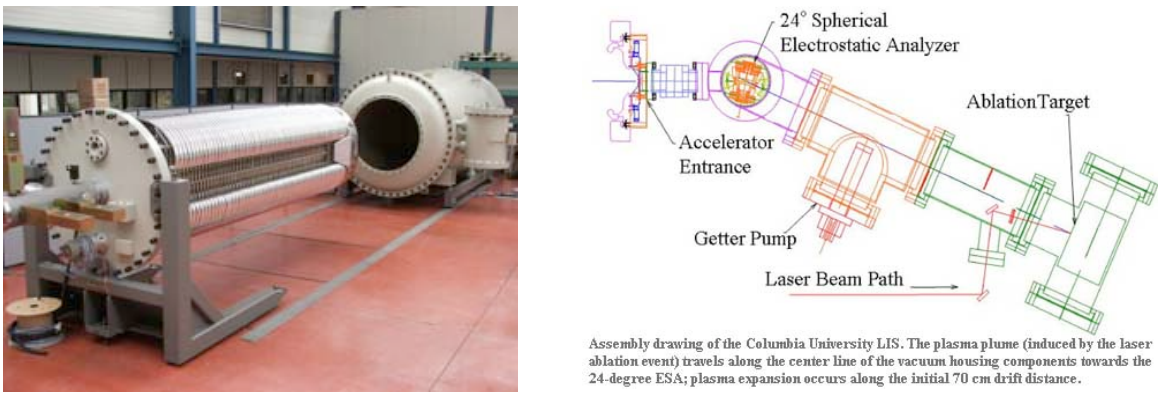

(a) (b)

Figure 1.11: (a) Image of the 5MV Van de Graff accelerator at RARAF. (b) Schematic of the Laser Ion Source at RARAF for the production of heavy ion species for high LET irradiations. Reproduced from www.raraf.org.

a quadrupole triplet operating at around 10 kV. This has allowed for ^{4}He ions to be repeatably focused down to a beam diameter of 0.8 um[13]. Protons and He nuclei for the microbeam, typically limited to LET values of up to 200 keV/um, are produced by an RF ion source. An additional laser ion source has been developed to allow for heavier ion beams to

be produced. This source uses laser ablation to form a plasma plume from a particular target element. Ions as light as Beryllium and as heavy as Iron can be produced by the source, electrostatically analyzed, and injected into the accelerator. These larger ions can provide LET values for microbeam irradiation ranging from 150 keV/um to over 4000 keV/um[14].

In addition to the two mentioned here numerous other particle based microbeam systems exist. Various configurations and systems are used to achieve the basic microbeam requirements. Some use horizontal while others use vertical beamlines. Microbeam formation is achieved via collimation in some cases and focusing in others. In addition to these components various methods are used for cell positioning and recognition. In particular more recent developments in cell recognition and sample positioning software have allowed for the high cell irradiation rates reported. The ability to scan a microbeam also provides another means of increasing the cell irradiation rate while reducing the need for sample dish translation. While many of the particle based beams have a broad range of capabilities and have a substantial performance history there are some disadvantages. Accelerators add a degree of cost and/or size that is not practical for every lab environment, and their coverage of the low end of the LET spectrum can be lacking. Smaller, less expensive systems may promote expansion of microbeam research into the hands of a broader set of scientists increasing microbeam accessibility. Yet these systems are by no means obsolete as they are unrivaled in irradiation rates and in resolution, and many represent the most advanced microbeams available.

1.3.2 X-ray Microbeam Systems

In addition to ion microbeam research there has been significant work done in the development of X-ray microbeam systems. X-ray based irradiation systems utilize various X-ray sources and various forms of focusing or collimation to produce micron sized beams of X-ray radiation. And while LET may be relatively high with heavy particles, with many of the X-ray based systems the LET from the X-ray energy may be quite a bit lower, especially the higher the energy of the photon. This can be attributed to at least two factors. First, as compared with particle interactions, photon interactions with matter take place over a much larger mean free path between incidences of interaction. Second, many of the X-ray energies produced by these cell irradiators are usually in the range of 1-10 keV. Because of this lower LET, studies looking at low dose effects are possible. Also low energy X-rays experience very little scattering confining their energy deposition to the area of irradiation, a necessary element of microbeam irradiation. Both GCI and RARAF have developed X-ray microbeams to complement their existing ion microbeams, discussed earlier.

The GCI X-ray microbeam is a table top system utilizing a custom built electron gun to generate X-rays from a multi-target anode. The system (Figure 1.12) can produce C_K (0.28 keV), Al_K (1.48 keV) and Ti_K (4.5 keV) X-rays depending on the target selected. X-rays produced are reflected off of a mirror to remove unwanted bremsstrahlung radiation. X-ray optics, including a zone plate mounted below the irradiation target, are used to focus the beam. With the Carbon target the K shell X-rays can be focused down to 1 um with a dose of 0.2 Gy/s[9, 15]. For the Al and Ti targets focusing is on the order of several microns with similar dose output.

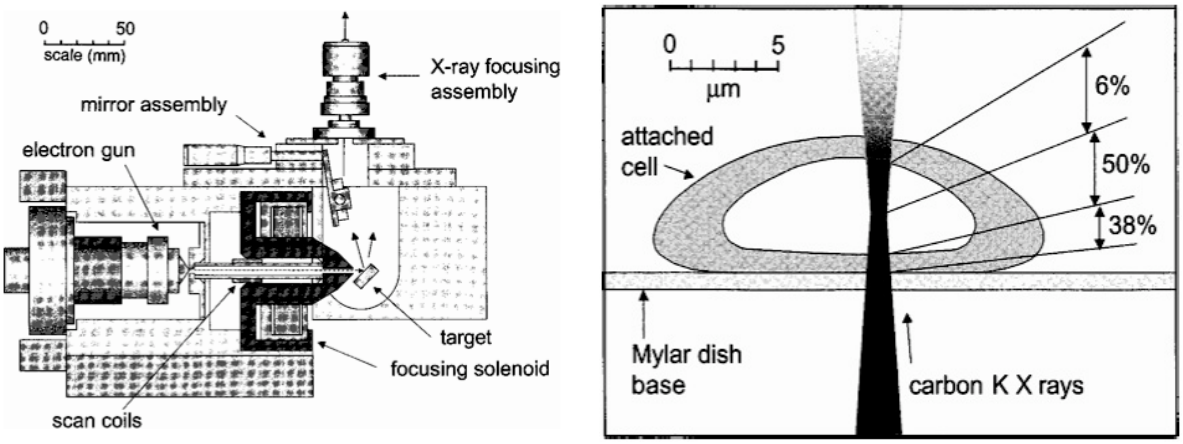

(a) (b)

Figure 1.12: (a) X-ray microfocus source. Electron bombardment is used to generate a micrometer sized source of characteristic X-rays. A mirror between the source and focusing assembly removes unwanted bremsstrahlung radiation. (b) Reproduced from reference [9].

The RARAF X-ray microbeam is similar but utilizes a few different features. The X-ray microbeam shares an endstation with the particle microbeam at RARAF. This enables the use of the proton beam from the accelerator to be used for X-ray generation by impinging the beam on thin, Helium cooled, target foils of Al and Ti, producing Al_K (1.48 keV) and Ti_K (4.5 keV) X-rays. Using the proton source allows the X-ray focal spot to be on the order of 10 um while also producing a narrower energy spectrum of X-rays that are nearly monochromatic. This minimizes the requirements placed on the zone plate, which is used to focus the beam. A beam diameter of 2um is achieved with a dose rate of 30 cGy/min.[16-18]

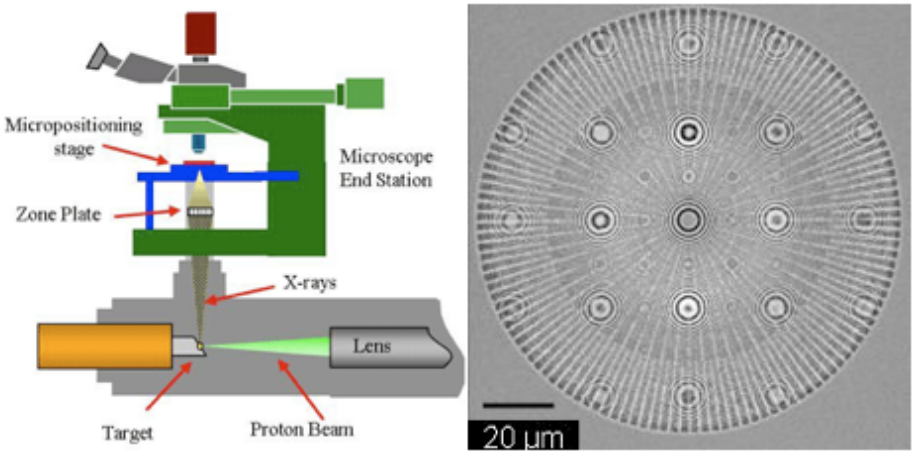

(a) (b)

Figure 1.13: (a) The RARAF endstation used for X-ray microbeam experimentation, showing the use of a proton beam to produce a relatively monochromatic X-ray source. (b) Image of the zone plate optic used to focus the X-ray beam down to an area of 2um.
http://www.raraf.org/new_developments.htm

A slightly different example of the X-ray microbeam is the one developed at Osaka University. This system utilizes a more standard X-ray tube with a Rhodium target (Figure 1.14(a)). The source is not monochromatic, but is focused by means of a tapered 100 mm glass capillary after which the beam travels an additional 30 mm to the target cells. The minimum beam size achieved is 14 um with 0.05 Gy/s dose rate [19]. Experiments utilizing human fibroblast cells have been performed. [20]

Simulations were performed in the development of the Osaka system using an electron-photon transport simulation code, EGS4. These demonstrate one of the main capabilities and rationales behind X-ray irradiation. In Fig 1.14(b) we see the locations of scattered electrons produced by two narrow diameter beams of 10 and 20 keV X-rays. The dose is confined laterally as is essential for microbeam irradiation, but at these energies it is also spread over the path of the beam through the sample to depths of 50 um or

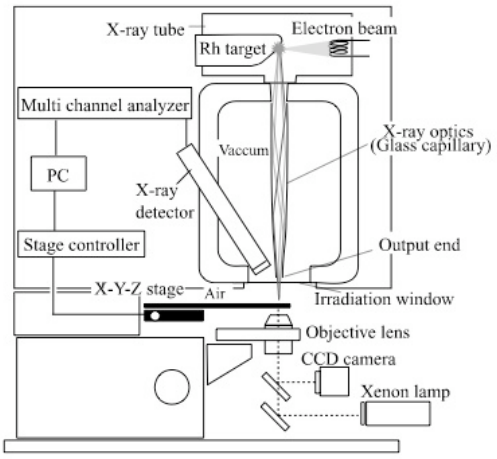

(a)

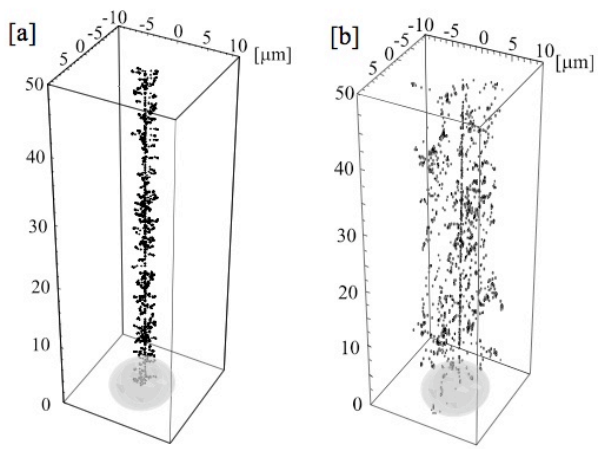

(b)

Figure 1.14: (a) Layout of tabletop X-ray beam irradiation system. X-ray tube voltage could be up to 50kV. Output end of glass capillary is set at 10mm from irradiation window. (b) Scattered electrons spread along X-ray beam path. X-ray beam ([a]E=10keV, [b]E=20keV) traced on the center axis. A cell (grayed sphere, size:10 um) is located at the end of the X-ray beam path. This shows the general shape of X-ray irradiation over a larger depth range. Reproduced from reference[19]

more. While the C_K (0.28 keV) and Al_K (1.48 keV) X-rays only penetrate 1.9 um and 7 um respectively Ti_K (4.5 keV) X-rays can penetrate well over 100um[21]. This capability opens the door to bulk tissue irradiation whereas most particle based microbeams are limited to one or two cell layers.

Given the way the microbeam is formed in many of the X-ray systems the dose delivery rate is much lower than that available in particle based systems, although many of those have been used for low dose single or few ion hit evaluation. A few recent studies have also suggested that a small dose of X-rays may be able to initiate repair mechanisms in cells to protect against subsequent higher irradiation exposure.

1.3.3 Electron Microbeams

1.3.3.1 Role of electrons in radiation dose deposition

X-rays primarily interact with matter via the Compton effect but also via the photoelectric effect. The Compton Effect or incoherent scattering describes an event in which the incident X-ray photon inelastically collides with an atomic electron ejecting that electron from the atom while also producing a secondary X-ray photon with reduced energy as compared to the incident photon. This secondary photon may then take part in future events. At higher incident energies (>100k eV) Compton scattering dominates the interactions.

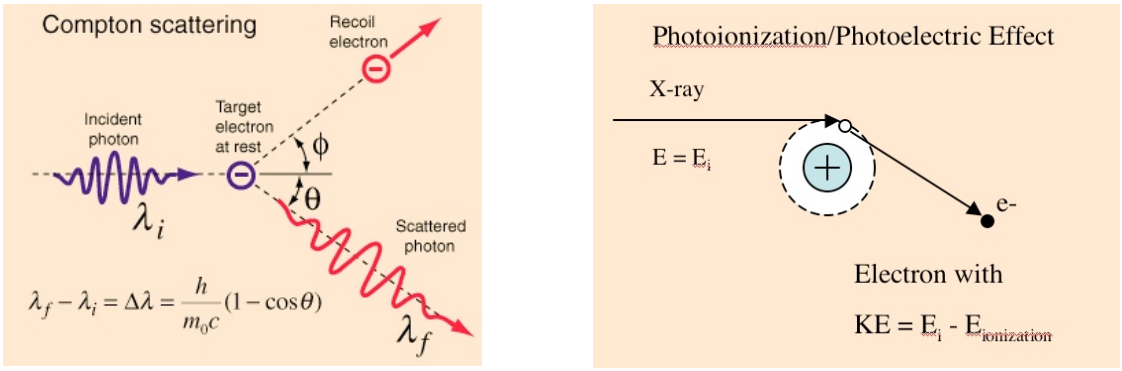

Figure 1.15: Modes of photon energy deposition in matter: (a) schematic of Compton Scattering in which the incident photon produces a photon of reduced energy along with a recoil electron. Reproduced from http://hyperphysics.phy-astr.gsu.edu/hbase/HFrame.html (b) schematic of the photoelectric effect in which an incident photon ejects an electron and imparts its remaining energy as kinetic energy.

Incidence of the photoelectric effect increases though with decreasing energy of the incident photons. In the photoelectric effect X-rays impinge on a bound electron ejecting it from the atom but with a kinetic energy equal to the photon energy minus the work function of the atom. In this case no future Compton or photoelectric events will take place, but rather energy will be deposited via liberated electrons.

In each of these cases the sum of the possible occurrences is a series of X-ray interactions resulting in scattering, reduced X-ray energy, and numerous ejected electrons. Some photons may pass through a material and experience no interaction, but those that do interact and deposit energy do so eventually by the absorption of electron kinetic energy.

A similar statement could be made about the absorption of energy from charged particles. Their energy is also deposited largely by the production of energetic electrons.

1.3.3.2 Current Electron Microbeam Systems

Given these modes of energy loss and deposition it becomes clear that an electron microbeam is also feasible method of irradiating cells[22]. Although the incident energy

source is of a different form the final energy deposition method is the same, and it is typically low-LET. Several electron microbeams have been developed for low-LET studies since the year 2000 including those at the Pacific Northwest National Laboratory (PNNL), at Texas A&M University, and at the Korea Institute of Radiological and Medical Sciences (KIRAMS).

The PNNL system utilizes a commercially available electron gun capable of electron energies between 10 and 80 keV (Figure 1.16). The beam current can be varied between 1 pA and 10 uA and is measured using a Faraday cup that is placed in the beam path. In vacuum the beam is several millimeters in diameter but is collimated down to several microns utilizing a laser drilled aperture. The aperture is an approximately 5um diameter hole laser drilled through a 250 um thick Tantalum foil, yielding an aspect ratio of 50:1. Dose measurements were performed using GafChromic HD-810 film and then correlated to the beam current.

The PNNL system had, since its development, been moved to the University of Maryland where recent data obtained has actually shown no apparent bystander effect[23]. The system was recently moved back to the PNNL.

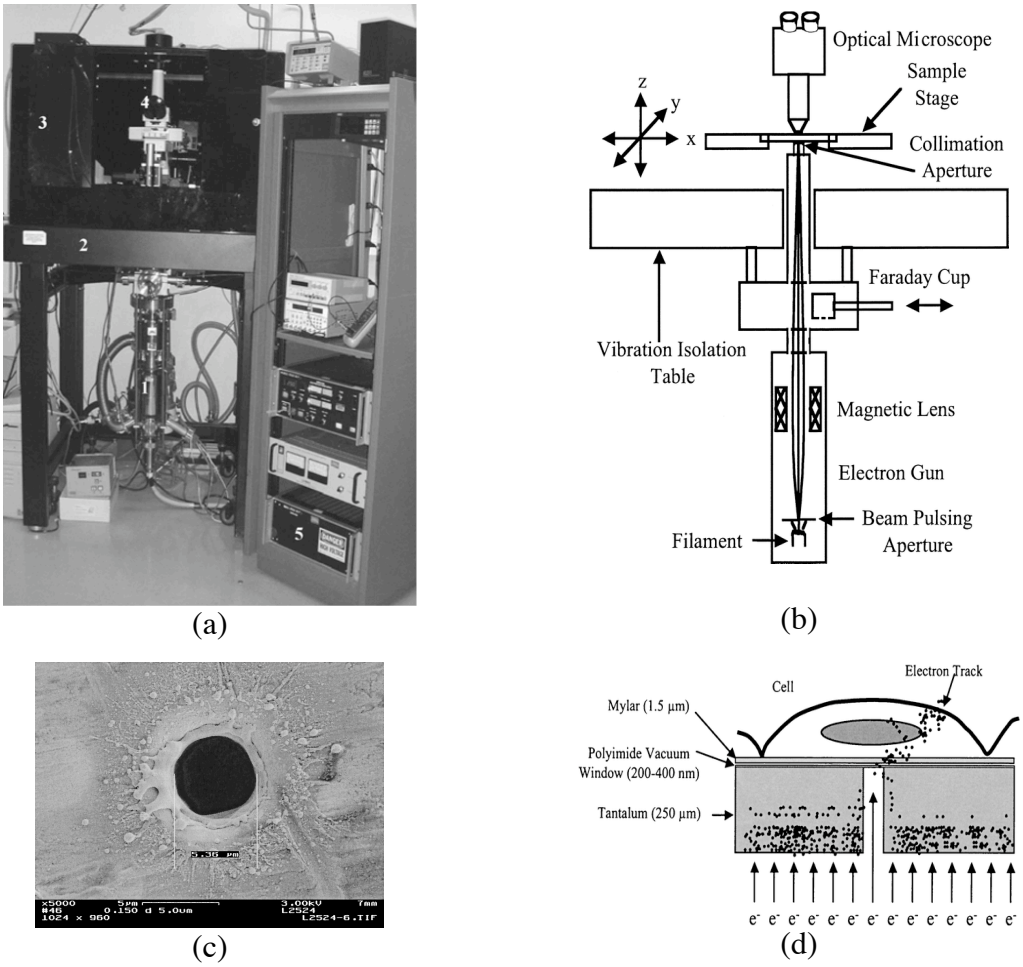

Figure 1.16: (a) Photograph of the PNNL microbeam with its primary components: (1) pulsed electron gun, (2) vibration isolation table, (3) temperature controlled enclosure, (4) automated epi-fluorescence imaging system with CCD camera, (5) controls electronics. Reproduced from [22] (b) schematic of electron beam control components. (c) Schematic of cell irradiation via laser drilled aperture of subcellular scale. (d) SEM micrograph of laser drilled aperture in Tantalum foil. (b), (c), & (d) reproduced from reference [10]

The Korea Institute of Radiological and Medical Sciences (KIRAMS) has also developed an electron microbeam based on the same electron gun as the PNNL microbeam. The electron beam is focused down to a 2 mm beam via electromagnetic focusing, but final collimation for irradiation is accomplished via a 5 um etched aperture in a thin stainless steel foil, 12.5 um thick in at least one instance[24]. The system bears many similarities to microbeam systems previously described. The electron gun, microscope, and cell translation

stages are all situated on an optical table to minimize vibration (Figure 1.17). Because of the long beam path (70 cm) between the cathode and the anode significant magnetic deflection of the beam (2-5 mm) was measured. Corrective measures were taken to remove magnetic materials and to provide magnetic insulation to minimize this effect.

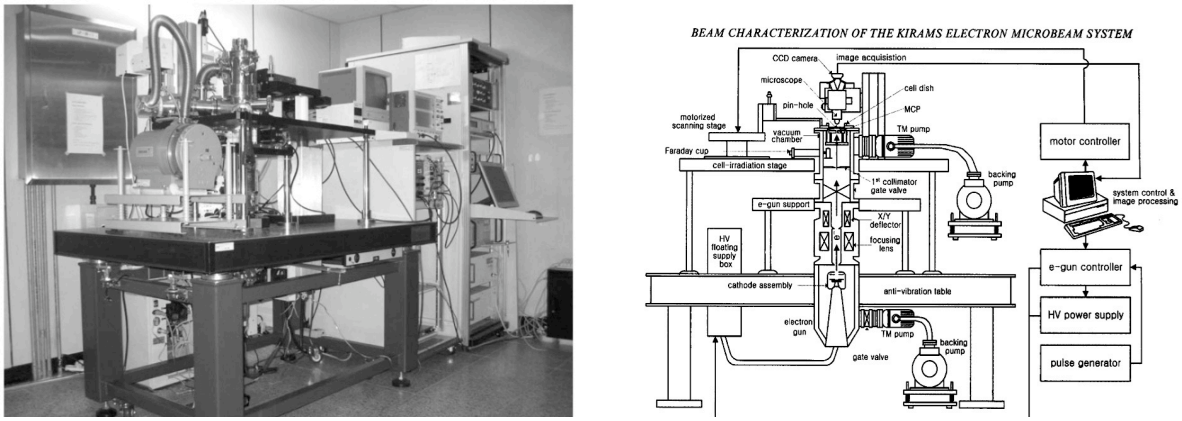

(a) (b)

Figure 1.17: Photo (a) and schematic (b) of the KIRAMS electron microbeam system. Depicted are the electron gun, alignment system, pumping system, and control electronics. Reproduced from reference [25]

The instrument has a variable beam energy of 1-100 keV utilizing a grounded anode. Beam current ranges from 100 pA to 100 nA with the beam pulse width as little as 2 us, although at lower currents some beam stability problems exist. Extensive study and calculation has been performed to correlate beam current, electron count, electron energy, and measured dose. Table 1 shows data on the number of electrons needed to produce a certain dose response, compared with that for alpha particles and protons.

Beam source	Alpha		Proton	Electron			
Energy	3.5 MeV	5.3 MeV	3 MeV	70 keV		30 keV	
Cellular dose	0.21 Gy/α	0.14 Gy/α	0.02 Gy/p	0.01 Gy (±100%[a])	5 e's[b]	0.01 Gy (±90%)	7 e's
				0.1 Gy (±37%)	50 e's	0.1 Gy (±30%)	70 e's
				1 Gy (±12%)	500 e's	1 Gy (±10%)	700 e's
				10 Gy (±4%)	5000 e's	10 Gy (±3%)	7000 e's

Table 1. Comparison of cellular doses with different microbeam sources. Reproduced from reference [26]

1.3.3.3 Electron Microbeam Simulation Data

Figure 1.18 schematically illustrates the possible interactions that an incoming electron can experience upon irradiating a cell. Collisions and interactions result in direction change or possibly secondary electron production. Given these interactions in the cell volume it is clear that the electron effects may not solely be limited to the area equal to the dimensions of the aperture but may affect a broader diameter around the aperture. Typical cell sizes are in the range of 15 um in diameter[27], but cells may vary widely in size with some muscle and nerve cells 30 cm or longer[28]. Given that many cells have lengths in this range, then for single cell irradiation it is necessary to keep the largest percentage of the dose deposition within a radius of 5-10 um from a relatively small electron collimator.

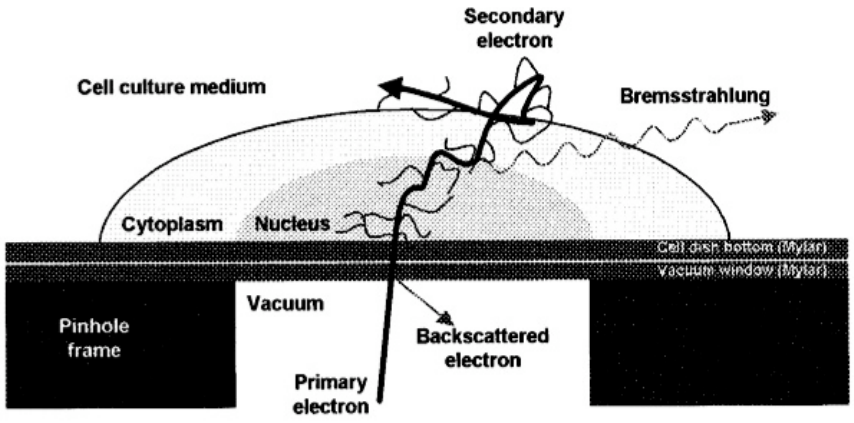

Figure 1.18: Schematic illustration of the possible interactions of a primary electron incident upon a mylar layer and a cell monolayer in media. Secondary electrons as well as Bremsstrahlung radiation may be formed. The electron may be backscattered or exit the cell completely. Reproduced from reference [24].

In order to evaluate this need simulations have been performed to determine the effective irradiation radius of an electron microbeam, and in particular to optimize the beam energy, as a large range of beam energies are available. These data help to inform choices about both aperture size as well as choice of cells for irradiation experiments. In Figure 1.19(a) simulation data obtained by the KIRAMS group using the EGSnrc Monte Carlo code

[24] graphically depicts the dose deposition occurring after electrons pass through the 5 um aperture. As can be seen in the case of the 30 keV beam most of the dose is deposited within a depth of 10 um after passing through the Mylar layer. At higher energies a large percentage of the dose deposition and/or beam energy is deposited beyond the first layer of cells, making these energies less efficient for cell monolayer irradiation in that a smaller portion of the total energy is deposited in the first layer. In the 50 keV case the lateral beam spread, although at greater depths is substantial, possibly leading to the irradiation of adjacent untargeted cells. In the 70 keV case the beam spread at the greater depths is lower than the 50 keV case, but the dose deposition in the monolayer is not too dissimilar from the 25 keV case, which would suggest that the lower energy irradiation would be equally effective for monolayer irradiation.

At Texas A&M University an additional electron microbeam has been developed and used for microbeam experiments. The system itself bears many similarities to the other electron microbeams described above. For its collimation mechanism a glass capillary is used. A variety of dosimetry simulations have also been completed for this system as well[29, 30]. Data in general agreement with that of the KIRAMS microbeam group was found by simulation (Figure 1.19(b)). These data also show that for the 25 keV beam energy 90% of the dose is deposited within a radius of 8.65 um of a pencil beam, and at 50 keV this values triples to 27.1 um. The 25 keV results are the best fit for irradiation of cells in a monolayer.

Other simulations completed by the Texas A&M group provide excellent insight into the differences between low and high LET radiation and possible differences in bystander effects as a result[31]. Most notable is the vast difference in the amount of dose that can be

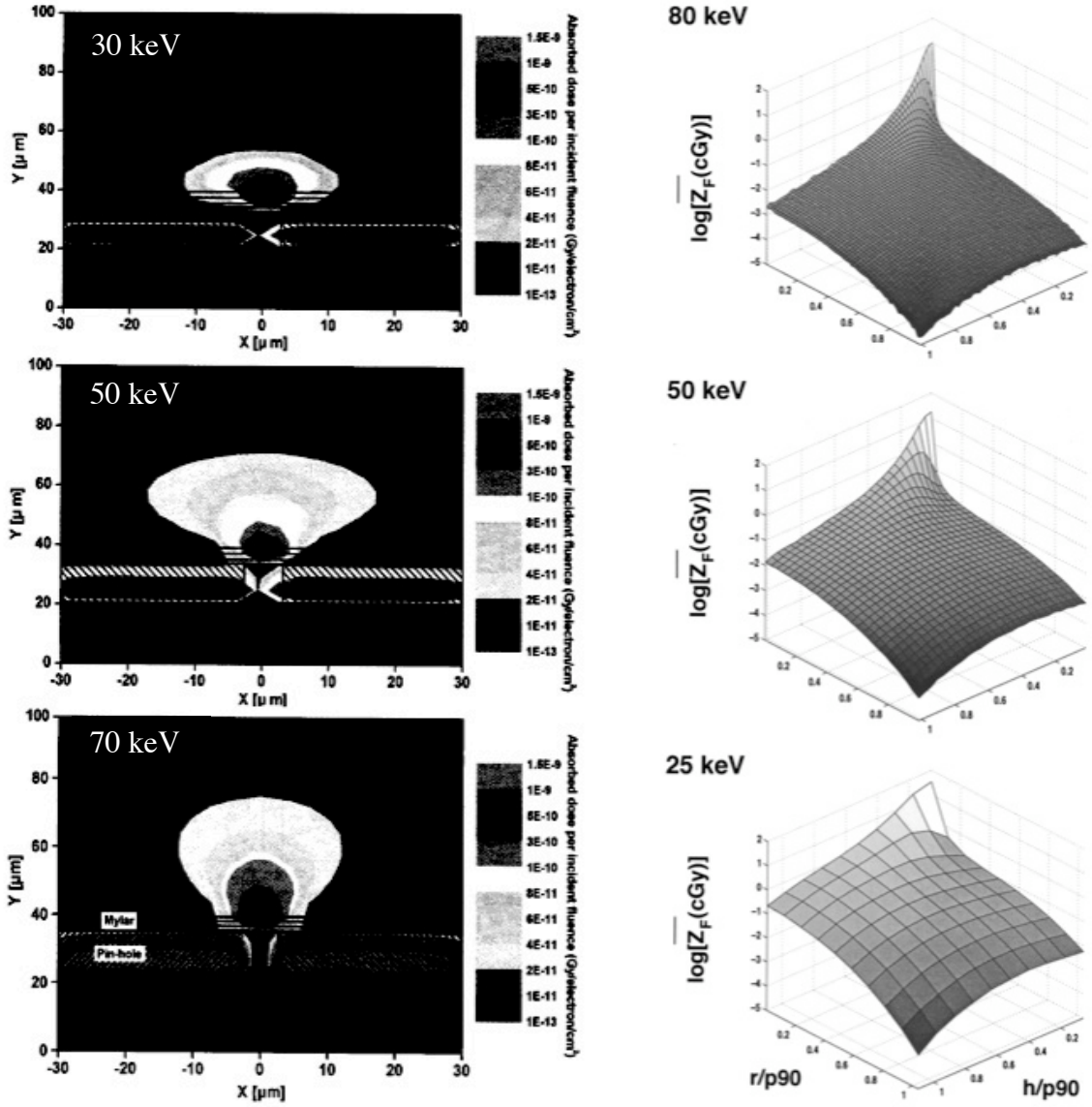

(a) (b)

Figure 1.19: (a) KIRAMS Simulated dose contour plots of 30, 50 & 70 keV electron beams passing through a 5um aperture and entering a water medium (at ~ 35um on the y-axis); 30 keV data shows the best dose localization for a cell monolayer as at higher energies much of the dose passes through the cell thickness. Reproduced from reference[24]. (b) Texas A&M simulated plots of the frequency mean of specific energy deposited in 1 um spherical sites by 25, 50, and 80 keV primary electrons a function of lateral (*r*) and forward (*h*) penetration, scaled by the distance from the beam entry point within which 90% of the energy is absorbed. The radial distance values calculated for 25, 50 and 80 keV incident beams at which 90% of the dose is absorbed were 8.65, 27.1 and 56.2 um, respectively as can be seen from the number of data squares in each figure, again showing 25 keV to be in the energy range appropriate for cell monolayer irradiation. Reproduced from reference [30].

deposited in small volumes of a cell. While almost all of the energy of an electron will be deposited in a particular cell or target volume that energy is spread out over many small volumes such that any 0.5 um diameter sphere might absorb only 0.3 keV of energy. In the case of alpha particles or low energy X-rays perhaps not all of the energy will be deposited in the cell, but the energy that is deposited may leave as much as 66 keV of energy in that same small volume. This concentration of energy and therefore potential cell damage represents a very different picture from the results of low-LET radiation.

Simulation data completed at UNC showed a similar result to the published simulation data. A Monte-Carlo simulation using the PITS code employed by the Texas A&M group[32-34] was performed for a pencil beam of a small number of electrons showing their respective electron tracks. Incident energies of 10, 30, and 60 keV were used with all the electrons entering a water equivalent medium. Beam diameters of approximately 2, 12, and 30 um respectively were obtained (Figure 1.20).

The first conclusion from these simulations is that a beam energy in the neighborhood of 25-30 keV, along with a small collimator of perhaps 5 um, should provide the electron penetration and beam width appropriate to irradiation of single cells in the size range of 20-25 um. Smaller cells would make this more challenging, while larger cell-to-cell spacing would provide some simplification.

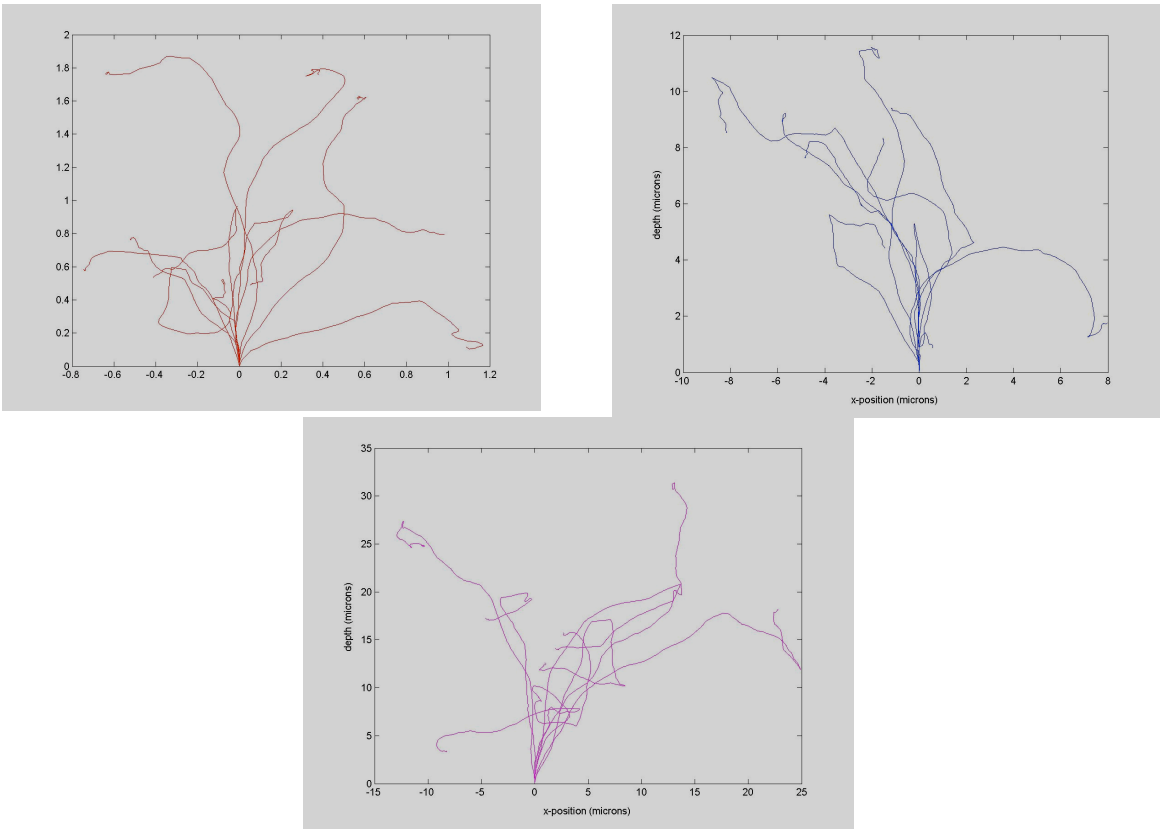

Fig 1.20: Graphical representation of Monte Carlo data of multiple electron tracks for electron energies of 10, 30, and 60 keV, showing distribution of electrons in a water medium. The distribution diameter of the beams is approximately 2, 12, and 30 um for each energy. Simulation data courtesy of Eric Schreiber, UNC Radiation Oncology.

In looking at the lower and higher energy ranges there may be some opportunities for their use, but each of these have some disadvantage. Lower energies, perhaps 10-20 keV, may provide better dose localization, i.e. a smaller irradiation diameter, which is desirable. Unfortunately though the electron window and cell dish bottom layers reduce beam penetration into the cell monolayer. The 10 keV data presented show a dose deposition radius of only 1 um and a depth of 2 um. When using a cell dish bottom layer thickness of 3 um along with the possibility of air gaps between the beam exit window and the cell dish only a small percentage of the beam might actually penetrate into the cells. As for the higher energies the 50 keV data suggest that the beam spread is much larger, and that the

depth of penetration might result in irradiation beyond the cell immediately over the aperture. For the 70 and 80 keV data it appears that forward scattering of the electrons is more significant than at 50 keV. Therefore the profile of the beam up through the thickness of the cell monolayer may be compatible with single cell irradiation, with the additional dose deposition above the cells in the cell media. But this introduces a somewhat uncontrolled dose deposition, requiring that cells be firmly attached in the monolayer. It also adds an additional 40keV high voltage requirement to the system. Therefore, while there may be some potential for the use of higher or lower energies, focusing first on the goal of 30 keV electron acceleration energies for the prototype CNT based single and multi-pixel systems is best supported by the available data.

1.4 Summary and Motivation

We have seen that the area of microbeam research has been growing substantially in depth and diversity in recent years. Systems based on a variety of radiation sources have been developed. Each of these systems has unique advantages. The particle accelerator based systems have reached a remarkable level of functionality and precision with extremely high rates of single cell irradiation and excellent control systems for microscopy and cell translation. The X-ray based systems utilize a variety of techniques for producing radiation, and are in many cases able to produce very narrow diameter beams. And the electron based systems provide a simple and functional system for basic cell irradiation and, along with the X-ray based systems, are able to explore the low-LET range.

At the same time some disadvantages are present in each system. The charged particle microbeams have cost, size, and engineering issues that limit their use to those with

the resources, space, and manpower to maintain and operate the system or at minimum the proximity to be a user of the system. The X-ray microbeams have shown themselves to be somewhat limited in terms of dose rate. The ability to discreetly irradiate a particular cell at a particular moment at any reasonable desired dose may be somewhat lacking in these systems. And for all of the systems discussed, particle, X-ray, and electron microbeams, each has been limited to a single beam. In some cases the ability to translate between cellular targets in a dish at high speeds mitigates this limitation, but the development of a multiple beam irradiator would open doors for different types of irradiation experiments involving simultaneous irradiation.

Also for the low-LET systems size minimization is limited as a result of the large commercial electron guns utilized, the electron focusing optics that are used, or the distances over which X-ray beams are focused or collimated. These limitations can be addressed through the capabilities associated with carbon nanotube (CNT) based field emission cathodes. CNT cathodes can be utilized in relatively compact systems and they can be designed to produce multiple, individually controllable cathodes in a compact area. Along with the proper collimation and cross-talk prevention multiple cathodes could be used for irradiation separated from one another over ranges measured in millimeters or less.

The use of CNT cathodes, whose capabilities we will discuss further in the next chapter, have the possibility of making a new and important contribution to the area of microbeam research.

References

1. K.M. Prise, O.V. Belyakov, and M. Folkard, *Investigating the cellular effects of isolated radiation tracks using microbeam techniques*. Adv. Space Res., 2002. **30**(4): p. 871-876.

2. G. Randers-Pehrson, C.R. Geard, G. Johnson, et al., *The Columbia University single-ion microbeam*. Radiation Research, 2001. **156**: p. 210-214.

3. E.J. Hall, S. Mitchell, and D.J. Brenner, *How Many Bystander Effects are There?*, in *6th International Workshop on Microbeam Probes of Cellular Radiation Response*. 2004, Radiation Research: Oxford, UK. p. 117-118.

4. W.F. Morgan and M.B. Sowa, *Effects of ionizing radiation in nonirradiated cells*. Proceedings of the National Academy of Sciences of the United States of America, 2005. **102**(40): p. 14127-14128.

5. R.E. Zirkle and W. Bloom, *Irradiation of Parts of Individual Cells*. Science, 1953(8 May 1953): p. 487-493.

6. *Proceedings of the 7th International Workshop: Microbeam Probes of Cellular Irradiation Response*. 2006. Columbia University, New York, New York: Radiation Research.

7. S. Gerardi, *A comparative review of charged particle microbeam facilities*. Radiation Protection Dosimetry, 2006. **122**(1-4): p. 285-291.

8. M. Folkard, B. Vojnovic, K.M. Prise, et al., *A charged-particle microbeam: I. Development of an experimental system for targeting cells individually with counted particles*. Int. J. Radiat. Biol., 1997. **72**: p. 375-385.

9. M. Folkard, G. Schettino, B. Vojnovic, et al., *A focused soft X-ray microbeam for targeting cells individually with submicrometer accuracy*. Radiation Research, 2001. **156**: p. 796-804.

10. M. Sowa, M.K. Murphy, J.H. Miller, et al., *A variable-energy electron microbeam: A unique modality for targeted low-LET radiation*. Radiation Research, 2005. **164**: p. 695-700.

11. B.D. Michael, M. Folkard, and K.M. Prise, *Meeting Report: Microbeam Probes of Cellular Radiation Response*. Int. J. Radiat. Biol., 1993. **65**(4): p. 503-508.

12. D.J. Brenner. *RARAF Milestones*. 2009 [cited; Available from: http://www.raraf.org/milestones.htm.

13. G. Randers-Pehrson, G.W. Johnson, S.A. Marino, et al., *Sub-micron Charged Particle Beam at Columbia University*, in *8th International Workshop on Microbeam*

Probes of Cellular Radiation Response, H. Imaseki, Editor. 2009, Radiation Research: Chiba, Japan. p. 47.

14. A.W. Bigelow, G. Randers-Pehrson, R.P. Kelly, et al., *Laser ion source for Columbia University*. Nuclear Instruments and Methods in Physics Research B, 2005. **241**: p. 874-879.

15. *8th International Workshop on Microbeam Probes of Cellular Radiation Response*. 2009. Chiba, Japan: Radiation Research.

16. G. Schettino, G. Randers-Pehrson, and D.J. Brenner, *Development of a Soft X-Ray Microbeam at RARAF*. Radiation Research, 2006. **166**: p. 661-662.

17. A. Harken, G. Randers-Pehrson, and D. Brenner, *Development of a Proton-Induced X-Ray Microbeam at Columbia University*, in *8th International Workshop on Microbeam Probes of Cellular Radiation Response*. 2009, Radiation Research: Chiba, Japan.

18. *RARAF - New Developments*. 2009 [cited; Available from: http://www.raraf.org/new_developments.htm.

19. T. Kuchimaru, F. Sato, Y. Higashino, et al., *Microdosimetric Characteristics of Micro X-Ray Beam for Single Cell Irradiation*. IEEE Transactions on Nuclear Science, 2006. **53**(3): p. 1363-1366.

20. F. Sato, T. Kuchimaru, T. Ikeda, et al., *X-ray microbeam measurement with radiophotoluminescent glass plate for single cell irradiation*. Radiation Measurements, 2008. **43**: p. 912-916.

21. M. Folkard, *The Future of the GCI Microbeams*, in *6th International Workshop Microbeam Probes of Cellular Radiation Response*. 2004, Radiation Research: Oxford, UK. p. 88-89.

22. M.S. Resat and W. Morgan, *Microbeam developments and applications: a low linear energy transfer perspective*. Cancer Metastasis Rev, 2004. **23**: p. 323-331.

23. W.F. Morgan, W. Goetz, and M. Sowa, *No Bystander Effect After Irradiation of Mammalian Cells with a Variable Energy Electron Microbeam*, in *8th International Workshop on Microbeam Probes of Cellular Radiation Response*, H. Imaseki, Editor. 2009, Radiation Research: Chiba, Japan.

24. G.M. Sun, E.H. Kim, K.B. Song, et al., *Beam Characterisation of the KIRAMS Electron Microbeam System*. Radiation Protection Dosimetry, 2006. **Vol. 121**(No. 2): p. 84-91.

25. G.M. Sun, E.H. Kim, K.B. Song, et al., *Preliminary Results of the Beam Control and Detection of the KIRAMS Electron Microbeam System*. Nuclear Engineering and Technology, 2005. **37**(2): p. 185-190.

26. E.H. Kim, G.M. Sun, and M. Jang, *An electron microbeam cell-irradiation system at KIRAMS: performance and preliminary experiments* Radiation Protection Dosimetry, 2006. **122**(1-4): p. 297-300.

27. H. Lodish, *Molecular Cell Biology*, ed. S. Tenney. 2000, New York: W. H. Freeman and Company.

28. E. Marieb, *Human Anatomy and Physiology*. 1992, Redwood City, CA: Benjamin/Cummings.

29. W.E. Wilson, D.J. Lynch, K. Wei, et al., *Microdosimetry of a 25 keV Electron Microbeam*. Radiation Research, 2001. **155**: p. 89-94.

30. J.H. Miller, M.T. Batdorf, D.J. Lynch, et al., *Microdosimetry of Electron Microbeams*. Radiation Research, 2004. **162**: p. 474-479.

31. L.A. Braby and J.R. Ford, *Energy Deposition Patterns and the Bystander Effect*, in *6th International Workshop on Microbeam Probes of Cellular Radiation Response*. 2004, Radiation Research: Oxford, UK. p. 113-115.

32. W.E. Wilson and H. Nikjoo, *A Monte Carlo code for positive ion track simulation*. Radiat. Environ. Biophys., 1999. **38**: p. 97-104.

33. J.H. Miller, M.S. Resat, N.F. Metting, et al., *Monte Carlo simulation of single-cell irradiation by an electron microbeam*. Radiat. Environ. Biophys., 2000. **39**: p. 173-177.

34. W.E. Wilson, J.H. Miller, D.J. Lynch, et al., *Analysis of low-energy electron track structure in liquid water*. Radiation Research, 2004. **161**(591-596).

CHAPTER TWO

PROPERTIES, FIELD EMISSION, AND APPLICATIONS OF CARBON NANOTUBES

2.1 Carbon Nanotube History and Structure

As scientific investigation in nanotechnology has grown and developed in recent years one of the materials that has been most investigated is the Carbon Nanotube. The discovery of Carbon Nanotubes is most often credited to Iijima of NEC, Japan based on his article in Nature of November 1991[1]. But an article by Monthioux and Kuznetsov in an August 2006 article in Carbon[2] suggests that the credit for the discovery of the CNT predates Iijima by a decade or even two. Nevertheless Iijima's paper, released at the time that it was, certainly aroused a much greater interest in their study and potential applications.

As Iijima's paper and others clearly demonstrated a tubular form of carbon had been discovered (Figure 2.1). CNTs are now considered a new allotrope of carbon, sharing some similarities with other existing allotropes. The most commonly known and abundant allotropes of carbon are graphite and diamond. CNTs themselves fall under the larger allotrope subgrouping of fullerenes.

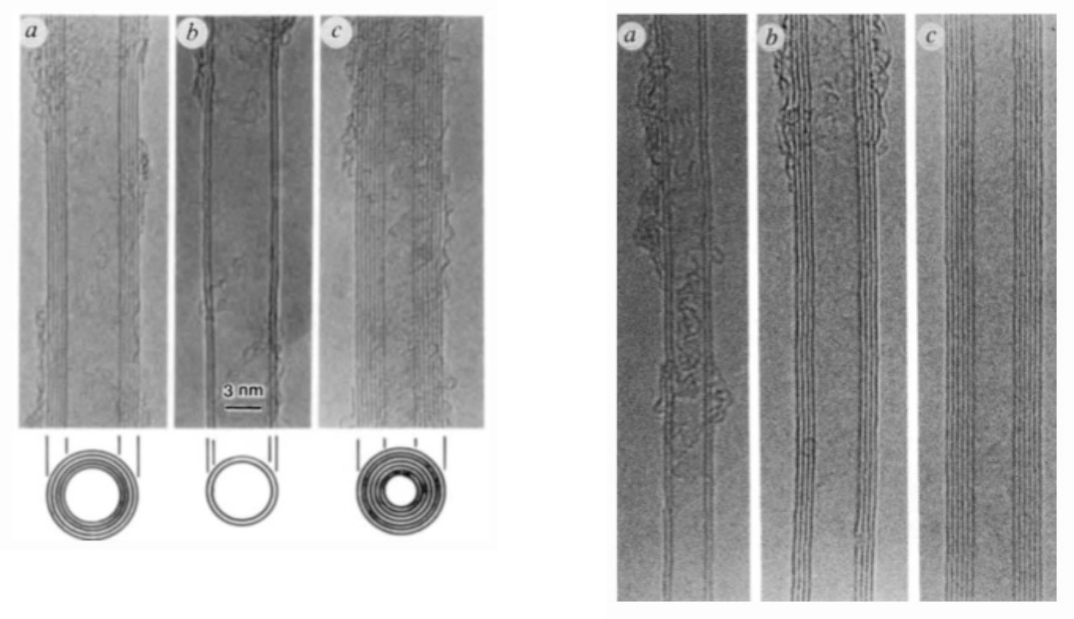

Figure 2.1: Early images of Carbon Nanotubes obtained by Transmission Electron Microscope. (a) Iijima's images of five, two, and seven walled nanotubes with outer diameters of 6.7, 5.5, and 6.5 nm. (b) Ebbesen's images of two, four, and six walled nanotubes with an interlayer distance of 0.34 nm. Reproduced from reference [1, 3]

2.1.1 Bonding Structure

These many allotropes exist as a result of the unique covalent bonding capabilities of carbon. In its atomic, ground state carbon has two electrons in the non-bonding *1s* orbital, and two electrons each in its *2s* and *2p* orbitals. The *2s* and *2p* orbitals are capable of hybridization in ways that allow them to form a variety of bonding options. In each of these cases one electron from the 2*s* orbital is excited into the vacant third 2*p* orbital leaving four orbitals half filled. In sp^3 hybridization these half filled 2*s* and three 2*p* orbitals combine to form four hybrid orbitals with identical character, explaining the tetrahedral structure and equal bond energy of materials with sp^3 bonding. Four bonds then form with separate atoms in sp^3 bonding. In sp^2 hybridization the 2*s* orbital combines with two of the 2*p* orbitals to form three hybrid sp^2 bonds. As these new hybrid orbitals are equally oriented spatially they form three bonds in a plane each with an orientation of 120 degrees to another. The

remaining p orbital electron then serves to form a double bond with an adjacent atom having a free p orbital electron. Finally in *sp* hybridization the 2*s* orbital combines with a single 2*p* orbital to form two bonds each on opposite sides of the atom. The remaining two 2*p* orbitals then are able to contribute to form two double bonds or a single and a triple bond with adjacent atoms.

For the allotropes of carbon mentioned sp^3 hybridization is seen in diamond, for which each diamond carbon exhibits the sp^3 tetrahedral bond structure. Hybridization of the *sp* form is more rare in bulk carbon materials, but it is seen in some organic materials. The sp^2 bond structure is the hybridization that is most useful in understanding carbon nanotubes. As stated, in an sp^2 bond structure three bond directions are formed equally in a plane, resulting in 120 degree angles between the bonds. This structure is most easily seen in graphitic allotropes. Here a hexagonal lattice of carbon atoms is formed each with sp^2 hybridization. These planar sheets of graphite stack together to form bulk graphite. The layers are held together by weak intermolecular forces allowing them to slip and move relative to one another under stress. This accounts for graphite's use as a lubricant. Graphite is also a soft and conducting material.

2.1.2 CNT Structure

The basic structure of graphite is the starting point for understanding the larger grouping of carbon allotropes known as fullerenes. Fullerenes, named because of their resemblance to the geodesic structures designed by the American architect, Buckminster Fuller, take on a variety of shapes, such as spheres, ellipsoids, and tubes. Each of the carbon fullerenes is composed of sp^2 hybridized carbons but with a variety of shapes. The fullerene perhaps most easily recognized is the spherical C_{60} molecule, the Buckyball. It bears some

similarity to graphite, but instead of being composed of a purely hexagonal lattice, it is composed of hexagons and pentagons, 20 and 12 respectively, such that the pentagons are completely surrounded by hexagons. The molecule then resembles a standard soccer ball. Each carbon is generally sp^2 hybridized, but because of the curvature necessary to form a spherical molecule the bonds have some sp^3 character. While C_{60} is the most common of the enclosed fullerenes others exist as well such as C_{70}, C_{80}, and C_{84} [4].

The graphite structure is even more helpful in understanding the structure of carbon nanotubes. While CNTs can come in a variety of sizes and configurations their structure is most easily described as a layer (or layers) of graphite rolled up into a cylinder, although this is not an accurate means of describing their synthesis. Although CNTs are often depicted as single layers or shells of carbon atoms, they may consist of multiple layers as well. In fact the first nanotube discoveries were of multi-wall tubes while it was only later that Iijima in a subsequent paper of his demonstrated the discovery of single wall nanotubes.[5] The terms single wall nanotube (SWNT), few wall nanotube, and multi-wall nanotube (MWNT) are often used to describe the products from different CNT synthesis processes. CNT synthesis samples can be analyzed via Transmission Electron Microscopy (TEM) to determine their general content.

2.2 Synthesis of Carbon Nanotubes

As stated earlier the rolling of graphite into cylindrical structures should not be construed as the process by which a CNT or other fullerene is formed. Rather a more complex formation mechanism takes place in a high-energy environment. Each of the

fabrication techniques used in CNT synthesis provides such a high energy environment and, depending on conditions, may result in the formation of CNTs in varying abundance and kind.

2.2.1 Arc Discharge

The oldest method of producing CNTs is via an arc discharge method. Here an electric arc is produced in a Helium or Argon filled chamber between two carbon electrodes separated by approximately 1mm [6]. The electric arc vaporizes the graphitic carbon, which reforms into various fullerene materials as well as amorphous carbon. Large quantities of reaction material are produced, but the CNT product is not as pure as other available methods. A catalyst or catalytic mixture can also be placed into the electrodes. This changes the type of CNTs formed and potentially the deposition profile in the chamber. One major disadvantage to the arc discharge process is that it requires frequent cleaning of the process chamber.

2.2.2 Laser Ablation

Laser ablation[7] is another common technique for producing CNTs. In this method a graphite or graphite/catalyst target is placed in a reaction chamber, such as a quartz tube, that is heated by an external furnace. A laser, usually pulsed, is focused on and used to irradiate the target. Each pulse vaporizes a small mass of target material creating an energetic plume of the carbon and catalyst. Inert gas is also flowed into the chamber regulating the pressure and carrying the reaction products downstream of the high temperature reaction environment. In another method the laser is still the power source, but the source material is introduced via gas feedstocks. Laser ablation does not produce as much reaction material, but the material is of a much higher purity. CNT material produced by laser ablation may also have a higher

degree of structural perfection and better field emission properties[8].

2.2.3 Chemical Vapor Deposition

Chemical Vapor Deposition is a third means by which CNTs can be synthesized[9, 10]. It differs substantially from the previous methods in that it can be used to grow CNTs attached to a substrate at predetermined locations. In this method a substrate is fabricated with catalyst particles attached to the surface. This can be accomplished by a variety of means, such as spin coating of a catalyst containing solvent over the substrate or by sputtering or evaporation of the catalyst material onto the substrate. The catalyst may be annealed or reflowed to remove organics and reduce the metal or to cause a thin layer of deposited material to transform into tiny catalyst islands on the order of the diameter of the CNTs. The substrate can then be placed in a chamber into which are flowed carbon containing reaction gases. In combination with an energy source, such as an RF generated plasma, and proper reaction conditions CNTs will grow from the catalyst particles.

In CVD as well as in the two previously mentioned methods the Vapor, Liquid, Solid (VLS) growth mechanism provides one helpful means of understanding CNT formation. While this is not the only theory, it provides a robust explanation for several observed phenomenon. In VLS the catalyst particles serve as the real growth substrate for the CNTs. Under the conditions associated with these processes the carbon sources are vaporized and the catalyst particles take on a liquid quality. The vaporized carbon is made soluble in and diffuses into the metallic liquid catalyst material. The carbon may become saturated in the metal solvent and at some point may begin to come out of solution and accumulate on the surface of the catalyst. For a small rounded catalyst particle the carbon nanotube may form a

nascent CNT shell or CNT cap with a diameter approximating the particle size. And in different cases the catalyst particle may remain at the base of the growing nanotube or travel along at the tip during the growth process, hence base growth and tip growth models. TEM images can be very helpful in identifying the location of the catalyst particles in this case. CNT growth may slow or terminate when the carbon ceases to diffuse or associate with the catalyst particles. A reduction in temperature or energy, removal of the carbon source, or possibly hindered diffusion into the catalyst as a result of multiple layers of CNTs on a particle could each serve to cause the CNT to cease growing in length.

2.3 Properties of Carbon Nanotubes

Understanding the CNT growth mechanism provides explanation for one of the most interesting physical properties often exhibited by CNTs, their high aspect ratio. Because CNTs can grow from their base or their tip continually with sufficient carbon source and energy they can be fabricated over great lengths while maintaining a very small diameter. Aspect ratios of 100:1 or greater are easily achieved.

In addition to their high aspect ratio CNTs exhibit a wide range of exceptional properties, which have been discussed thoroughly with an eye towards a large number of applications. CNTs have high thermal conductivity, high mechanical strength, as well as special electrical properties.

2.3.1 Thermal Conductivity

CNTs have extremely high thermal conductivity as compared with other materials. Metals known to be good thermal conductors, such as gold and copper, have thermal

conductivities in the range of 300-400 W/(m K). One experiment records a single 14 nm diameter MWNT having a maximum thermal conductivity measurement of over 3000 W/(m K)[11], nearly ten times higher.

2.3.2 Mechanical Strength

CNTs also exhibit exceptional mechanical properties. Experimental work has been performed demonstrating MWNTs with diameters from 26 to 76 nm having an average Young's modulus (E) value of 1.28 +/- 0.59 TPa[12]. This can be compared with modulus values of ~0.2 TPa for both Kevlar and Stainless Steel. Another study shows an average breaking strength for SWNTs of 30 GPa[13], far surpassing a maximum measured value for stainless steel of 1 GPa and values of several hundred MPa for most metals. For these reasons a great amount of interest has been placed in nanotubes for their potential in making extremely strong composite materials as well as truly fantastical possibilities such as the popularly postulated space elevator.

2.3.3 Electrical Properties and Structural Dependence

A third example of the uniqueness of CNTs is their electrical properties. Depending on their varying structural qualities an individual carbon nanotube can either be metallic or semiconducting with varying bandgaps.

As stated earlier a single wall nanotube can be envisioned as a rectangular section of a graphene sheet rolled into a tube. The structure of each nanotube can be described using the lattice vectors of the graphene sheet, $\mathbf{a}_1$ and $\mathbf{a}_2$, as seen in Figure 2.2(a). Using the hexagonal lattice two lattice points are selected which overlap in the nanotube 3D structure and also represent the vector along the circumference of the nanotube. This is referred to as the chiral vector and labeled as OA or C_h. By decomposing the vector into the sum of unit lattice vectors we find $OA = C_h = n\,\mathbf{a}_1 + m\,\mathbf{a}_2$ with the integer values, n and m, preceding $\mathbf{a}_1$

and $\mathbf{a}_2$, providing the identifying numerals for the nanotube. Therefore the specific structure of any nanotube can be described by the integer coefficients of the vector in the graphene plane describing its circumference. Furthermore the tube axis direction, perpendicular to the chiral vector, is noted by T. The helical angle of the nanotube is defined as the angle in the graphene plane between the chiral vector and the direction of $\mathbf{a}_1$.

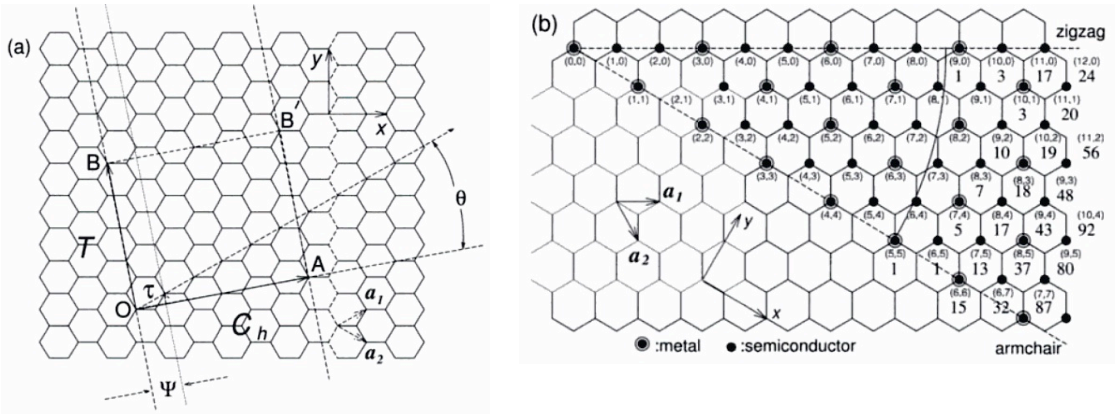

Figure 2.2: (a) Graphene sheet lattice showing its lattice vectors, $\boldsymbol{a}_1$ and $\boldsymbol{a}_2$, along with $\boldsymbol{C}_h$, the chiral vector and $\boldsymbol{T}$, the translation vector. $\boldsymbol{C}_h$ lies along and defines the diameter of the tube, while $\boldsymbol{T}$ lies along the axis of the tube. When rolled into the tube format O and A overlap. (b) Diagram of a number of possible chiral vector coefficients along with their default electronic states of metallic or semiconducting. Reproduced from reference [4].

In Figure 2.2(b) the identifying coefficients associated with each chiral vector are indicated. When n=m the tube is referred to as an armchair tube Figure 2.3(a). When m = 0 the tube is referred to as a zig-zag tube with a helical angle of 0° Figure 3(b). Both of these tubes have a mirror symmetry plane and for this reason are achiral. For all other configurations the nanotube is chiral. Figure 2.3(c) provides a illustration of a (10, 5) chiral tube.

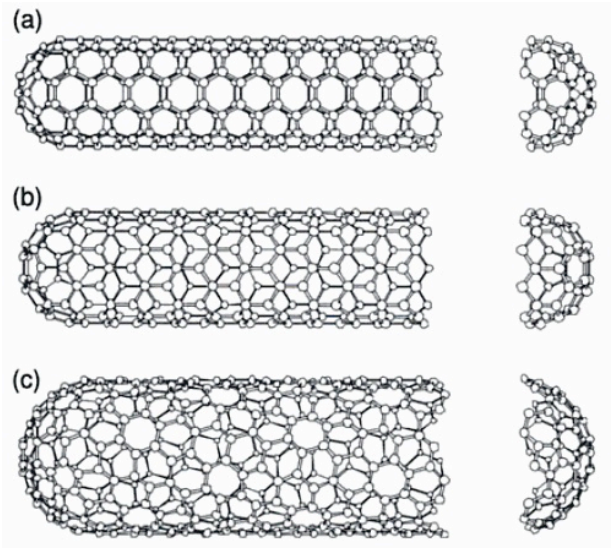

Figure 2.3: (a) armchair nanotube, all armchair nanotubes are metallic. (b) zig-zig nanotube (c) (10, 5) chiral nanotube. Reproduced from reference [14]

This naming convention also provides a quick method for defining the electrical properties of a particular tube. It has been demonstrated that the lattice coefficients for all metallic tubes satisfy the following condition, (n-m = 3q , where q = 0,1,2,…). And semiconducting tubes all satisfy the following condition (n-m = 3q +/- 1, where q = 0,1,2,…) [4, 15]. Given these conditions all armchair tubes are metallic as is every third tube in the zig-zag series [(3,0), (6,0), (9,0), …], in addition to other tubes as well. Figure 2.2(b) illustrates the electrical conductivity properties of tubes of varying structures.

The fact that some nanotubes are conducting while others are semiconductors of varying band-gap has aroused great interest in the direction of CNT microelectronics. On a more fundamental level multiple experiments have been undertaken to determine the electrical conductivity of CNTs particularly that of metallic nanotubes. In measurements of isolated MWNTs current densities exceeding 10^6 -10^7A/cm^2 have been observed[16, 17]. These conductivities far surpass that of many metals.

2.4 Thermionic Emission

Great interest has been shown in obtaining a sample of nanotubes exhibiting electronic uniformity. Attempts have been made to selectively fabricate and separate carbon nanotubes in order to accomplish this. As of yet these attempts have not shown great success. Therefore nanotube samples are typically composed of a mixture of these various types. Nevertheless each sample of nanotubes will contain some conducting and semiconducting nanotubes, meaning that the sample can be electrically conducting, despite being of mixed composition.

As a function of their electrically conducting nature one of the properties of CNTs that has brought about great interest is their ability to serve as high quality field emitters. Field emission is a process by which a material emits electrons in the presence of high electric fields.

Electrons are also emitted from metallic and semiconducting materials via thermionic emission and photoemission. In each of these cases a more classical emission process takes place. In any metal or semiconducting material the material's electrons generally fill the lowest available energy levels, with some occupying higher energy levels as a result of available thermal energy. At 0 K all the electrons reside in the lowest possible energy levels, with the uppermost energy being defined as the Fermi Energy, E_F, or Fermi Level. Still these electrons are bound to the material and typically only escape by obtaining extra energy to jump to an unbound state, referred to as the vacuum level. In the case of thermionic emission the extra energy is obtained from thermal energy usually generated by passing a high electrical current through the material, and for photoemission this energy is obtained from

interaction with a photon. When the thermal or photon energy transferred to an electron exceeds the surface energy barrier of the material, known as the work function, ϕ, the electron is liberated from its bound state in the material to the vacuum level energy. Therefore, in these two methods the current output is increased by elevating the temperature and the incident photon count respectively. In both cases a large amount of energy is invested in producing the electron current, and the source material may experience significant heating, particularly in thermionic emission.

Thermionic emission is described by the Richardson-Dushman equation (2-1). The equation describes the current density of emission from a metal as a function of its temperature:

$$J = \frac{4\pi mek_B^2}{h^3} T^2 \exp(-\frac{\phi}{k_B T}) = AT^2 \exp(-\frac{\phi}{k_B T}) \qquad (2\text{-}1)$$

In this equation e is the electron charge, k_B is the Boltzman constant, T is the temperature, and h is Planck's constant. From this equation we can see that the means by which emission current is increased is by increasing the temperature of the cathode material as all the other factors in the equation are constants. Although current output increases better than linearly with temperature the increased heat must be dissipated for the thermionic cathode to continue to function properly. Over time the cathode material may degrade via oxidation or heat induced transformation. In devices utilizing thermionic cathodes high vacuum conditions and/or adequate gettering are necessary to avoid degradation.

While increased thermal load is one disadvantage a related problem is the limitation on switching rate imposed by using thermionic emission. The cathode must be heated to initiate or allowed to cool to decrease current flow. Therefore a certain upper limit on

switching exists for cathodes operating solely on thermionic emission without additional electrode control of its current. Of course it should be acknowledged that thermionic capabilities exist which enable a wide variety of common and useful devices, such as X-ray tubes and electron sources form electron microscopy. Also thermionic cathode output current can be deflected or altered using additional electrodes, which have much higher switching rates. Nevertheless an additional electrode and power supply are not always desirable leaving an opening for cathodes that can be produced with higher switching rates.

2.5 Field Emission

2.5.1 Field Emission Theory

In contrast to thermionic emission field emission operates on a different principle. When the emitter material is in the presence of an electric field the surface energy barrier is reduced such that at a short distance from the material the energy level in the vacuum is equal to the Fermi Level with the energy level continuing to decrease with increasing distance from the surface (Figure 2.4). The work function is decreased in the process by the amount $\Delta\phi = (eE/4\pi\varepsilon_0)^{1/2}$, where e is the fundamental charge and E is the electric field strength. And while this reduces the height of the potential barrier what is more significant is that the barrier to a lower potential energy state has become finite. This opens up the possibility of significant tunneling through the potential barrier. Tunneling is the process by which particles move through potential barriers not by obtaining sufficient energy to overcome them but as a result of their finite statistical probability of being found on the other side of the potential barrier. Reducing the width of the potential barrier serves to enhance the number of particles that are able to tunnel through the barrier. Increasing the electric field

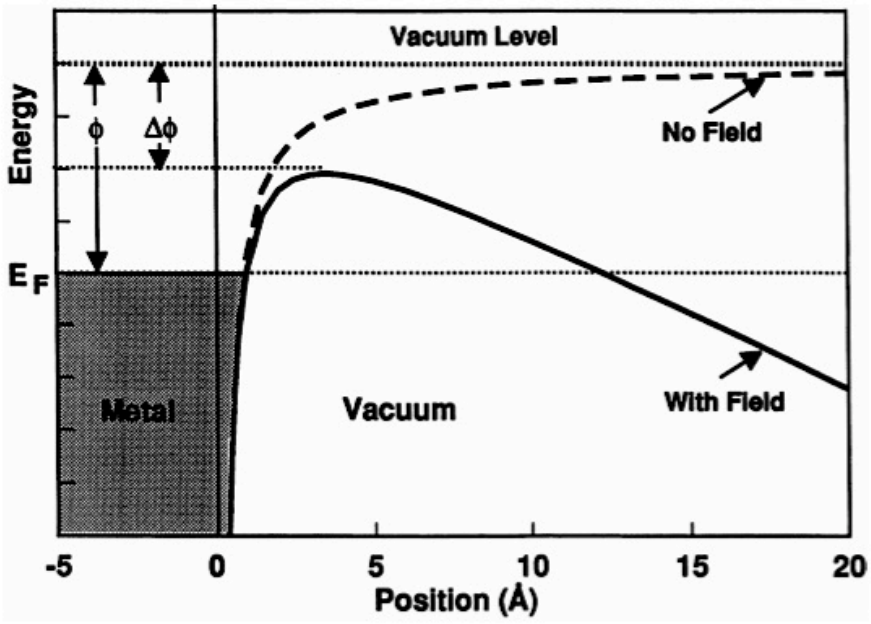

Figure 2.4: Energy diagram of an electron in relation to a metal surface. The dashed curved shows the energy barrier that an electron must overcome to escape to the vacuum with no applied field as is the case in thermionic emission. The solid curve shows the distortion in the energy barrier with an external electric applied field as is the case of field emission. $\Delta\phi$ signifies the reduction in the effective work function in the presence of the applied field. Reproduced from reference [18].

strength further reduces this width. This can be done by increasing the bulk field strength or by an increase in the field strength near the surface of the emitter material.

Fowler and Nordheim completed theoretical calculations of field emission from metals which form the foundation of field emission theory. Their initial equation has been variously investigated and expressed by Gomer[19]:

$$i = 6.2x10^{6} \frac{(\mu/\phi)^{1/2}}{\mu + \phi} E^{2} \exp[-6.8x10^{7} \frac{\phi^{3/2}}{E}]$$

where i is the current density, μ and ϕ are the chemical potential and work function of the emitter material respectively, and E is the electric field. Modinos [20] expresses the equation in a simpler form:

$$i(E) = A' E^{2} \exp[-B' \phi^{3/2} / E]$$

where *i* denotes the current density from the field emitter surface as a function of electric field, *E*, and ϕ is the work function. *A'* and *B'* represent constants similar to those in Gomer's equation.

In Gomer's equation the current density is reported in amp/cm^2 and it can be shown that to achieve current densities of 10^2-10^3 amp/cm^2 that fields of 3-6 x 10^7 V/cm are necessary[19] for significant emission from flat surfaces. Field strengths on this scale are normally impracticable, but field emission becomes feasible when the effect of the localized electric field is taken into account. In the case where the surface contains conducting protrusions with high curvature, as with high aspect ratio structures, an enhancement of the electric field takes place which can produce significant field emission current with much lower applied voltages. In this case the local electric field around the emitter can be alternately expressed as $E_{local} = \beta V/d$, where V is the voltage applied to generate the electric field over distance d and β is a scaling factor indicating the degree to which the local field strength has been increased. The value of the enhancement factor may be as high as 1200[21], more than a three order of magnitude increase over the applied field, and in some cases values over 10,000 have been claimed[22].

Substituting E_{local} in for E in Modinos' equation and multiplying by the area of emission ($I = i \cdot a$) provides a function of the actual current:

$$I = a \cdot A'(\beta V/d)^2 \exp[-B'\phi^{3/2} d/\beta V]$$

By gathering the constants and reducing the equation to a function of V and β it becomes:

$$I = A(\beta V)^2 \exp[-B\phi^{3/2}/\beta V]$$

where $A = a \cdot A'/d^2$ and $B = B' \cdot d$.

From the new equation we can see that for any given system when the voltage is increased a resultant increase in the field emission current is produced that scales with the square of the voltage and with the exponential function. β has the same effect on the field emission current. A small increase in field enhancement can produce large effects on the field emission current. Of course for any given set up the value of β will vary from nanotube to nanotube and the actual field strength will depend on the separation between the cathode and anode. The Fowler-Nordheim equation does give us a means by which to evaluate whether a given emission situation is truly field emission or has other electron emission character in it. The F-N equation does provide a good approximation of CNT field emission although some data suggest that CNTs do not behave perfectly as metals, but rather their emission character is dependent on the surface states at the tip of the CNT[21], although the cylindrical body of a metallic type nanotube will conduct electrons and serve to provide a steady supply of electrons for ongoing field emission.

As mentioned earlier thermionic emission has the distinct disadvantages of excess heat production and a slower and/or more complicated switching mechanism. For these reasons alone field emission has been an attractive alternative to thermionic emission and a great amount of research has been performed to develop devices demonstrating excellent field emission properties.

2.5.2 Development of Field Emitter Arrays

One of the main foci of field emission application research has been the development of so called field emitter arrays. This work got its start in the 1960s and saw moderate development over the next two decades[18]. Spindt and colleagues are well known for their

work in developing field emitters based on the evaporation of metal into small apertures, commonly using molybdenum[23].

Both molybdenum and silicon have served as materials in the development of FEA devices. Techniques developed in microfabrication and semiconductor processing helped to facilitate the development of this technology. Using these techniques small scale and repeatable patterns of these devices have allowed them to be fabricated into relatively large arrays (FEAs). The devices themselves consist of large arrays of sharp tips (>1000) that are collectively gated by a conducting layer.

Depending on which material is used the fabrication process varies slightly. Figure 2.5 shows the process flow for fabrication of molybdenum based tips as well as silicon based tips. In the case of the metal tips holes are etched through a conducting gate layer and an insulating layer down to the base conducting layer. Next metal is deposited through the etched hole, with the hole gradually closing over the course of the deposition, leaving a peaked area of metal deposition in the hole.

While the metal method is based more on deposition to achieve the high sharpness necessary for field emission, the silicon method is based on etching. Typically the sharpness of the tips is achieved by various types of chemical etches while protecting the tip with a masking material. The schematic and SEM image in Figure 2.5 (c) and (d) show one example fabrication process and a cross section of a Si-FEA.

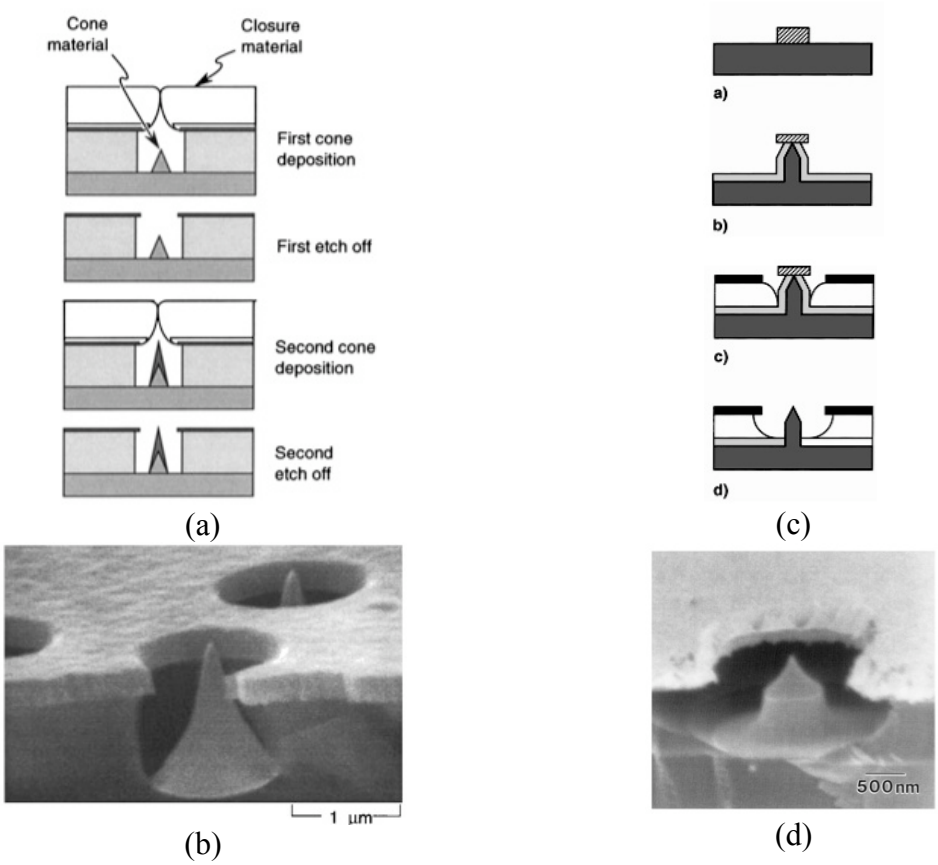

Figure 2.5: (a) Microfabrication scheme for a metal (e.g. Mo) field emitter tip along with (b) an SEM image of an array cross-section. The scheme above shows deposition of two layers of metal so as to form a sharper tip. (c) Microfabrication scheme for a Si-based tip, and (d) an SEM image of a single Si-based field emitter device. A nitride cap is grown, followed by an etch and an oxidation step. Insulator is deposited to form a gate layer. Images (a), (b), (c), and (d) reproduced from references [24], [25], [18], and [26] respectively.

The use of field emitter arrays has produced reasonable field emission results; as a result of their sharp tips they exhibit a high field enhancement factor. But the main disadvantage of these devices is their susceptibility to damage and their resultant diminished lifetime. Ionized species produce some bombardment and deterioration of the tips, which disrupts their field emission qualities[27].

2.5.3 CNT Field Emission

CNTs address some of the shortcomings of the Mo and Si microfabricated field emitters and FEAs. CNTs deposited in bulk can provide a potentially greater number of emitters in a given area than microfabricated tip arrays. Also CNTs are resilient even in the vacuum microelectronics environment and, as a result of their unique structure, continue to maintain a high aspect ratio even if some damage occurs to their tip. CNTs high aspect ratio also allows them to have a higher field enhancement factor and a lower threshold turn on voltage for field emission (Table 1). And while we have primarily compared CNTs to FEA tips, there are other materials, such as diamond, which have been investigated for their field emission properties[28], and most of them still fall short of CNTs. For these reasons CNTs currently hold the most promise for the development of reliable, high performance field emission devices.

Cathode material	Threshold field (V/μm) for a current density of 10 mA/cm^2
Mo tips	50–100
Si tips	50–100
p-type diamond	160
Defective CVD diamond	30–120
Amorphic diamond	20–40
Cesium-coated diamond	20–30
Graphite powders	10–20
Nano-diamond	3–5 (unstable >30 mA/cm^2)
Assorted carbon nanotubes	1–2 (stable >4000 mA/cm^2)

Table 1: Threshold electric field required for a 10 mA/cm^2 emission current density for different materials. Reproduced from reference [27].

2.6 Integration of Carbon Nanotubes

We have already discussed the many different ways in which CNTs can be produced, but in order for CNTs to be useful in various types of applications they must be integrated into various types of devices and systems. Methods exist for generally dispersing CNTs across wide areas such as spray deposition[8], but for integration the CNTs must be placed in a defined area. This a general challenge for all sorts of nanoparticles, and a wide variety of methods have been developed to attempt to address this challenge. Several of the methods used for the integration of carbon nanotubes particularly for electron field emission devices will be described demonstrating the diversity of techniques.

2.6.1 Nanotube Processing

The distribution and placement of CNTs into various devices is often accomplished by the use of solutions of these nanomaterials, as solutions provide a medium wherein the nanotubes can be readily dispersed and subsequently transferred. Depending on the manner in which a CNT sample had been grown it may take on a variety of different forms. The tubes may vary in length, bundle size, diameter, and in their impurity content. As mentioned earlier CNTs may be grown using catalyst particles. Often these catalyst materials in addition to other unwanted carbon products, such as amorphous carbon, may be present. Purification techniques have been developed using oxidants, solvents, and filtration to remove unwanted elements[29]. Because of their structure and relative length as compared to other products the nanotubes will survive an oxidative process better compared to perhaps shorter or less structurally perfect carbon structures.

In addition to purification techniques CNTs may be processed to make them more useable in a given application. In some cases the purified CNTs may be 10-50 um in length or longer and coalesced together into bundles; as such they may be impractical for some applications. Long, bundled, purified CNTs (Figure 2.6(a)) can then be processed in acid, for instance sulfuric and nitric acids to etch them down to more practical lengths. Etching may take place at the terminal ends of the tubes as well as at defect sites, cutting tubes somewhere along their length. The as processed tubes (Figure 6(b) take on a short rod like character, while preserving their diameter, following processing[30].

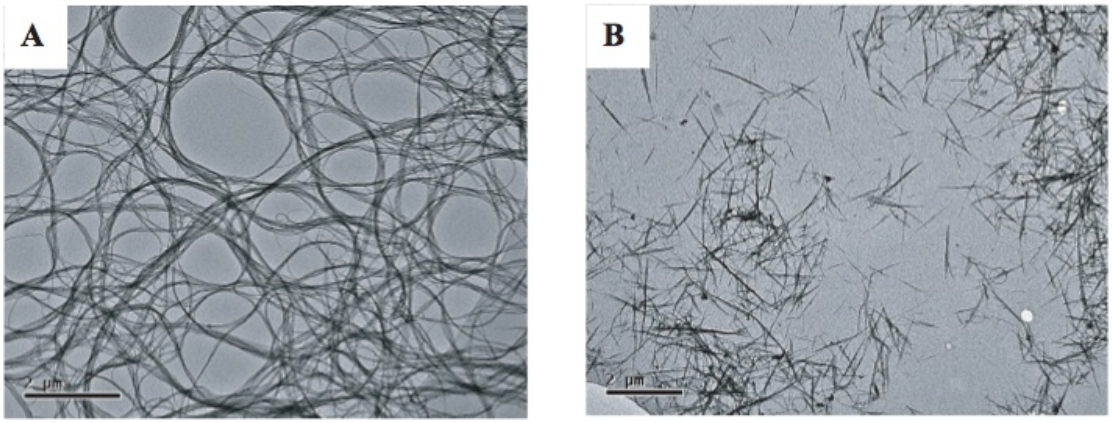

Figure 2.6: (a) Bundles of purified CNTs with ~10um length. Catalyst particles and other impurities have been removed. (b) Short rod like bundles of CNTs following acid "cutting" process with length of ~2um. Reproduced from reference [30].

Solutions of CNTs are relatively easily made using water, alcohol, or a mixture of the two as a predominant solvent, while adding in other solutes to more readily disperse the nanotubes. Ultrasonics are extremely useful in promoting dispersion as well. Additionally methods of attaching functional groups to the CNTs have been produced to allow CNTs to more readily interact with a solvent or to possibly chemically bond with other materials.

2.6.2 Self-assembly

One simple means of integration and placement that has been used is that of self-assembly. In this method a glass substrate may be patterned with photoresist for example and dipped into a solution containing CNTs as mentioned above. With certain surfaces of the substrate experiencing substantial wetting in comparison to other areas a meniscus will form at the junction of the substrate, solvent, and air interface along the hydrophilic

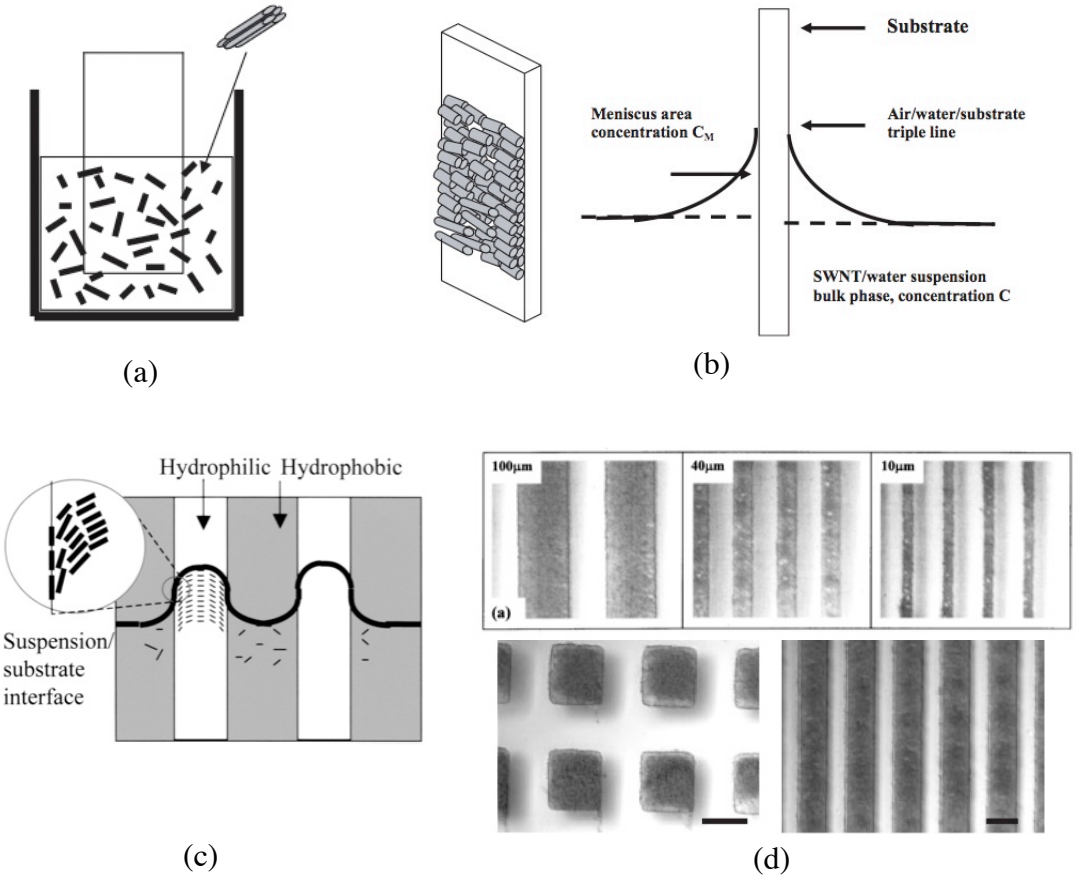

Figure 2.7: (a) Substrate is immersed in a CNT containing suspension; CNTs are deposited on the substrate as the solution evaporates lowering the fluid level or as the substrate is slowly pulled up and out of the solution. (b) On the left a schematic of as deposited CNTs on a substrate. On the right a schematic of the meniscus region at the substrate/air/water interface. The concentration of CNTs is increased in the meniscus region. (c) Schematic of a patterned substrate with hydrophilic and –phobic regions. Shortened CNTs align themselves to the edge of the meniscus effecting their deposition orientation. (d) Images of photoresist patterned glass substrates with CNT deposition in the hydrophilic regions. 10 um lines were easily patterned and square areas of 100um are possible as well. Reproduced from references [30, 31]

areas of the substrate. In the narrowing meniscus CNTs are confined and come into contact with the substrate, becoming aligned parallel to the contact edge of the solution with the substrate. Films with high uniformity and exhibiting field emission have been reported (Figure 2.7) [30, 31].

2.6.3 Dielectrophoresis

Another method that has been utilized is that of dielectrophoresis. This technique also uses liquid dispersed CNTs, but also utilizes an AC electric field applied between the solution and the target substrate. In this technique CNTs are preferentially deposited onto sharp surfaces where the electric field strength becomes concentrated and interactions between the substrate and the nanotubes are strongest. A simple schematic for dielectrophoresis is depicted in Figure 2.8 along with the results of a deposition performed on a sharp Tungsten tip. This method was used to construct nanotube probes capable of providing point electron sources [32] as well for use as scanning probe microscope tips with high aspect ratio[33].

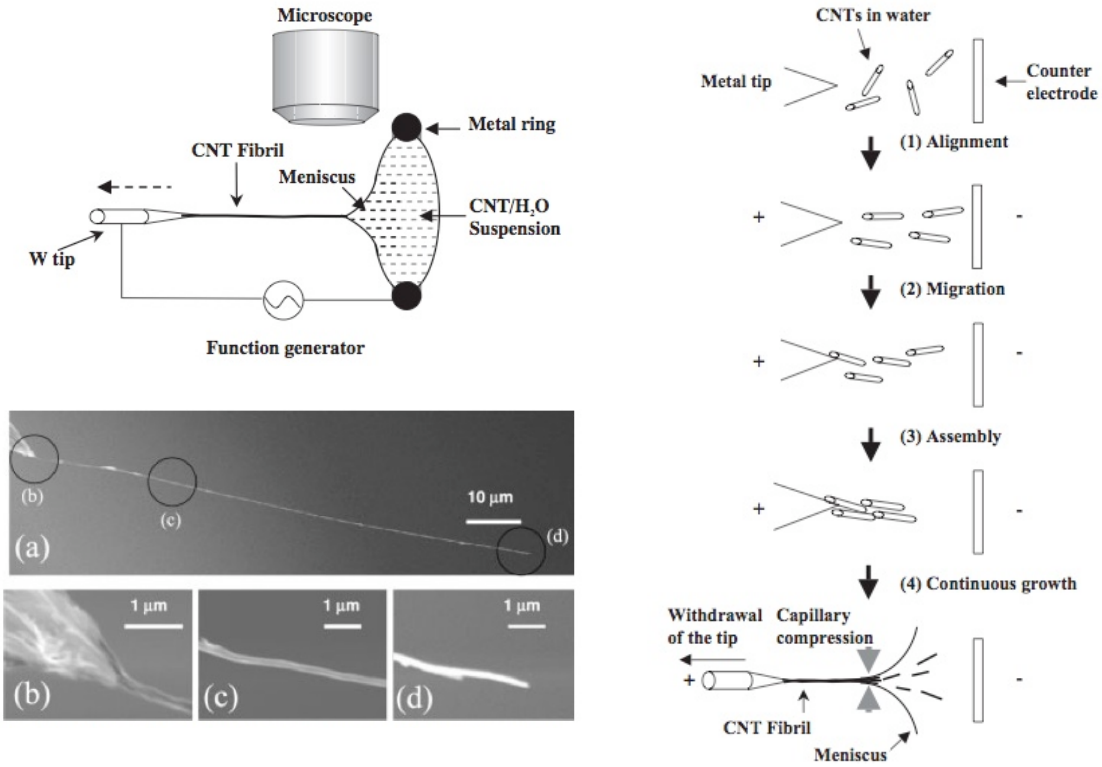

Figure 2.8: (upper left) Schematic of the set up used to perform dielectrophoresis showing an AC field applied between the target tip and the CNT solution. (lower left) SEM images of a CNT structure produced by drawing the metal tip out of the CNT solution under AC current. (a) is the overall image while (b), (c), and (d) show various segments of the fibril. (right) A schematic of the proposed step-wise mechanism of CNT fibril formation for this system.
Reproduced from reference [34]

2.6.4 Electrophoretic Deposition

In our group the method that is predominantly used is that of electrophoretic deposition (EPD)[35]. This method is also a liquid phase method that takes advantage of the molecular polarizability of small molecules in an electric field[36]. An electrode and counter electrode, with one serving as the deposition target substrate, are placed into a CNT containing solution. A DC field is applied between the electrodes in the solution, and the dispersed CNTs selectively attach to the conducting parts of the substrate (Figure 2.9.).

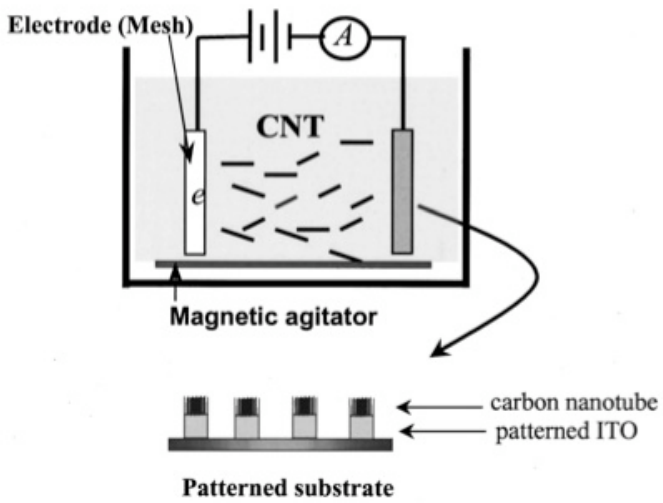

Figure 2.9: Schematic diagram of electrophoretic deposition set-up. CNTs are attracted to the negative electrode and bond to conducting portions of the substrate as seen in the bottom figure. The other electrode serves as a counter electrode in the solution. Substrates with defined conductive regions allow for definition of uniquely shaped cathodes. Reproduced from reference [37]

In contrast to dielectrophoresis a DC voltage is used, and the method does not require that sharp surface protrusions be used to perform the deposition. This makes EPD much more advantageous for depositing CNTs across larger surface areas. Salts or other ion source additives are added to the solution to facilitate the process. When a salt such as $MgCl_2$ is used CNTs migrate to the negative electrode, while NaOH brings about the opposite effect. Salt and electrical polarity can then be chosen to avoid deposition on the counter electrode. Because the CNTs only deposit on conducting regions of the substrate patterning of the conducting areas allows for patterned deposition.

2.6.5 Summary

The methods of CNT integration mentioned here demonstrate a few of the ways that CNTs can be integrated into useful devices. The ones highlighted here have been those by which CNTs can be deposited from solution. Immediately following deposition the CNTs

actually show remarkable stability, for instance they are not easily rinsed away in cleaning solutions. Nevertheless it should be noted that such methods often require drying and annealing of the CNTs on substrate to completely solidify the cathode structure, making them more resilient to either mechanical forces or the effects of high voltage used in vacuum electronics systems. Also in discussing integration of CNTs in systems we should note that CVD, mentioned earlier as a fabrication technique, may also serve as an integration technique. CNTs can be grown and harvested for processing and other purposes or can be grown in place for a predetermined purpose.

2.7 Nanotube Applications

Given their exceptional physical and electrical properties and the varying modes of incorporating them into systems it should be no surprise that CNTs have been used in a wide variety of applications. Some are experimental while others have been prototypes of possible commercial devices.

The focus of our work will be CNT field emission related, and many of the current applications are related to either field emission or other CNT electrical properties. One of the areas of greatest interest, and with a potentially high commercial potential, is that of field emission displays (FED)[38]. Because cathode layouts using CNTs are customizable a variety of display devices have been created, with the possibility for both monochrome and RGB systems included. Other applications have included an electron source for an electron microscope[39], microwave amplifiers[40], as well as electron sources for various X-ray related applications[41-44]. Other applications are related to CNTs potential use as semiconductors[15] and as extremely high aspect ratio atomic probes[33].

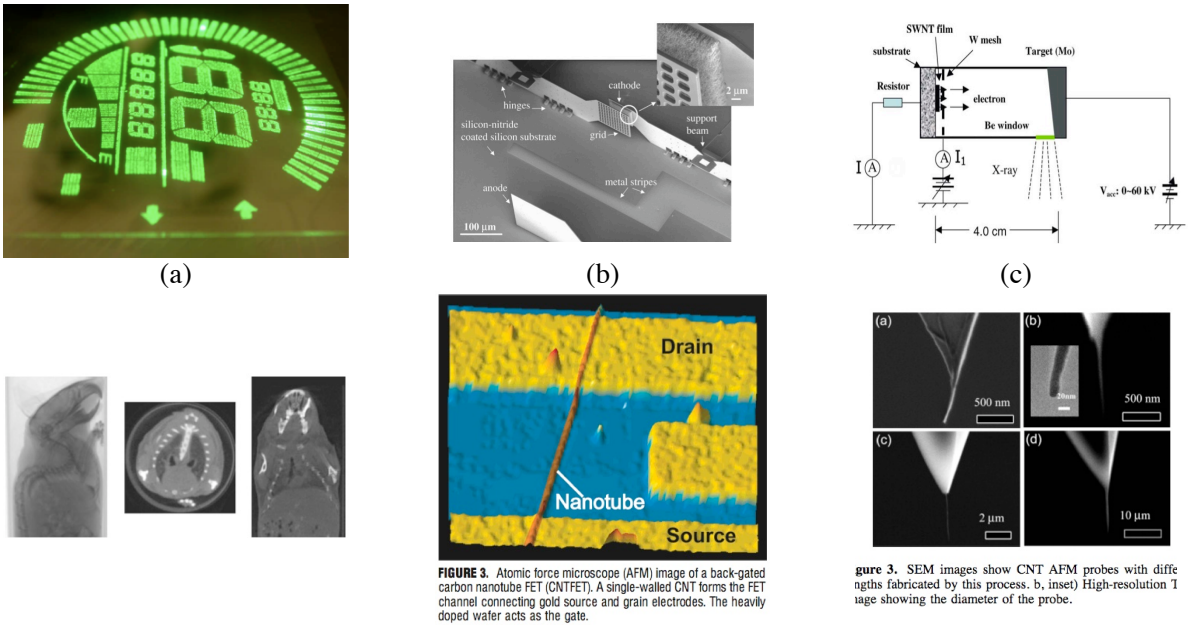

FIGURE 3. Atomic force microscope (AFM) image of a back-gated carbon nanotube FET (CNTFET). A single-walled CNT forms the FET channel connecting gold source and grain electrodes. The heavily doped wafer acts as the gate.

gure 3. SEM images show CNT AFM probes with diffe ngths fabricated by this process. b, inset) High-resolution T age showing the diameter of the probe.

Figure 2.10: CNT applications; (a) monochrome FED display from Xintek, Inc. (b) SEM image of CNTs integrated into micromachined triode structure [40]. (c) Schematic of CNT field emission X-ray tube [27]. (d) Projection image and transverse and coronal slices from CNT field emission based micro-CT [45]. (e) AFM image of prototype CNT Field Effect transistor [15]. (f) SEM images of CNT AFM probes produced by dielectrophoresis [33].

The next chapter will begin to discuss the application of interest for this dissertation, the carbon nanotube based field emission microbeam cellular irradiator. It has been shown that CNT field emission cathodes are suitable for a wide variety of devices. CNT applications have been demonstrated which have both large numbers of individual cathodes as well as CNTs functioning within high voltage systems. Both of these capabilities will be important in developing the prototype cellular irradiator.

References

1. S. Iijima, *Helical Microtubules of Graphitic Carbon*. Nature, 1991. **354**: p. 56-58.

2. M. Monthioux and V. Kuznetsov, *Who should be given credit for the discovery of carbon nanotubes?* Carbon, 2006. **44**(9): p. 1621-1623.

3. T.W. Ebbesen and P.M. Ajayan, *Large-scale synthesis of carbon nanotubes*. Nature, 1992. **358**: p. 16.

4. M.S. Dresselhaus, G. Dresselhaus, and P.C. Eklund, *Science of Fullerenes and Carbon Nanotubes*. 1996, New York: Academic Press.

5. S. Iijima and T. Ichihashi, *Single-Shell Carbon Nanotubes of 1-nm Diameter*. Nature, 1993. **363**: p. 603-605.

6. T.W. Ebbesen and P.M. Ajayan, *Large-scale synthesis of carbon nanotubes*. Nature, 1992. **358**(16): p. 220.

7. A. Thess, R. Lee, P. Nikdaev, et al., *Crystalline Ropes of Metallic Carbon Nanotubes*. Science, 1996. **273**: p. 483-487.

8. C. Bower, O. Zhou, W. Zhu, et al. *Fabrication and field emission properties of carbon nanotube cathodes, in Amorphous and Nanostructured Carbon*. in *Mat. Res. Soc. Symp. Proc*. 2000.

9. C. Bower, O. Zhou, W. Zhu, et al., *Nucleation and growth of carbon nanotubes by microwave plasma chemical vapor deposition*. Appl. Phys. Lett., 2000. **77**(17).

10. C. Bower, W. Zhu, S. Jin, et al., *Plasma-Induced Conformal Alignment of Carbon Nanotubes on Curvatured Surfaces*. Appl. Phys. Lett., 2000. **77**(6): p. 830-832.

11. P. Kim, L. Shi, A. Majumdar, et al., *Thermal transport measurement of individual multiwalled nanotubes*. Phys. Rev. Lett., 2001. **87**.

12. E.W. Wong, P.E. Sheehan, and C.M. Lieber, *Nanobeam Mechanics: Elasticity, Strength and Toughness of Nanorods and Nanotubes*. Science, 1997. **277**(26): p. 1971-1975.

13. M.-F. Yu, B. Files, S. Arepalli, et al., *Tensile Loading of Ropes of Single Wall Carbon Nanotubes and their Mechanical Properties* Physical Review Letters, 2000. **84**(24): p. 5552-5555.

14. M.S. Dresselhaus, G. Dresselhaus, and R. Saito, *Physics of Carbon Nanotube*. Carbon, 1995. **33**: p. 883-891.

15. P. Avouris, *Molecular Electronics with Carbon Nanotubes*. Accounts of Chemical Research, 2002. **35**: p. 1026-1034.

16. H. Dai, E.W. Wong, and C.M. Lieber, *Probing Electrical Transport in Nanomaterials:Conductivity of Individual Carbon Nanotubes*. Science, 1996. **272**: p. 523-526.

17. S. Frank, P. Poncharal, Z.L. Wang, et al., *Carbon Nanotube Quantum Resistors*. Science, 1998. **280**(5370): p. 1744-1746.

18. D. Temple, *Recent progress in field emitter array development for high performance applications*. Mat. Sci. and Engin., 1999. **R24**: p. 185-239.

19. R. Gomer, *Field Emission and Field Ionization*. 1961, Cambridge, MA: Harvard University Press.

20. A. Modinos, *Field, Thermionic and Secondary Electronemission Spectroscopy*. 1984, New York, NY: Plenum Pub Corp.

21. L. Forro and C. Schonenberger, *Physical Properties of Multi-wall Nanotubes*, in *Carbon Nanotubes : Synthesis, Structure, Properties, and Applications (Topics in Applied Physics, 80)*, M.S. Dresselhaus, G. Dresselhaus, and P. Avouris, Editors. 2000, Springer-Verlag: Heidelberg.

22. J.Y. Huang, K. Kempa, S.H. Jo, et al., *Giant field enhancement at carbon nanotube tips induced by multistage effect*. Appl. Phys. Lett., 2005. **87**: p. 053110.

23. C.A. Spindt, I.Brodie, L. Humphrey, et al., *Physical properties of thin-film field emission cathodes with molybdenum cones*. J. Appl. Phys., 1976: p. 5248-5263.

24. C.A. Spindt, C.E. Holland, P.R. Schwoebel, et al., J. Vac. Sci. and Tech. B, 1998. **16**: p. 758.

25. C.A. Spindt, C.E. Holland, A. Rosengreen, et al., IEEE Trans. Electron Dev., 1991. **38**: p. 2355.

26. D. Temple, W.D. Palmer, L.N. Yadon, et al., J. Vac. Sci. and Tech. A, 1998. **16**: p. 1980.

27. Y. Cheng and O. Zhou, *Field emission from carbon nanotubes*. C.R. Physique, 2003. **4**: p. 1021-1033.

28. N.S. Xu and S.E. Huq, *Novel cold cathode materials and applications*. Materials Science and Engineeering R, 2005. **48**: p. 47-189.

29. O. Zhou, H. Shimoda, B. Gao, et al., *Materials Science of Carbon Nanotubes: Fabrication, Integration, and Properties of Macroscopic Structures of Carbon Nanotubes*. Acc. Chem. Res, 2002. **35**: p. 1045-1053.

30. H. Shimoda, S.J. Oh, H.Z. Geng, et al., *Self-assembly of carbon nanotubes*. Adv. Mater., 2002. **14**(12): p. 899-901.

31. S.J. Oh, Y. Cheng, J. Zhang, et al., *Room-temperature fabrication of high-resolution carbon nanotube field-emission cathodes by self-assembly*. Appl. Phys. Lett., 2003. **82**: p. 2521.

32. J. Zhang, J. Tang, G. Yang, et al., *Efficient Fabrication of Carbon Nanotube Point Electron Sources by Dielectrophoresis*. Adv. Mat., 2004. **16**(14): p. 1219-1222.

33. J. Tang, G. Yang, Q. Zhang, et al., *Rapid and Reproducible Fabrication of Carbon Nanotube AFM Probes by Dielectrophoresis*. Nano Letters, 2005. **5**(1): p. 11-14.

34. J. Tang, B. Gao, H. Geng, et al., *Assembly of 1D nanostructures into sub-micron diameter fibrils with controlled and variable length by dielectrophoresis*. Adv. Mater., 2003. **15**(15): p. 1352.

35. B. Gao, G.Z. Yue, Q. Qiu, et al., *Fabrication and electron field emission properties of carbon nanotube films by electrophoretic deposition*. Adv. Mater., 2001. **13**(23): p. 1770-1774.

36. O. Van der Biest and L.J. Vandeperre, *Electrophoretic Deposition of. Materials*. Annu. Rev. Mater. Sci., 1999. **29**: p. 327-352.

37. W.B. Choi, Y.W. Jin, H.Y. Kim, et al., *Electrophoresis deposition of carbon nanotubes for triode-type field emission display*. Appl. Phys. Lett., 2001. **78**(11): p. 1547.

38. W.B. Choi, D.S. Chung, J.H. Kang, et al., *Fully sealed, high-brightness carbon-nanotube field-emission display*. Appl. Phys. Lett., 1999. **75**: p. 3129.

39. Niels de Jonge, Yann Lamy, Koen Schoots, et al., *High brightness electron beam from a multi-walled carbon nanotube*. Nature, 2002. **420**: p. 393.

40. C. Bower, W. Zhu, D. Shalom, et al., *On-chip vacuum microtriode using carbon nanotube field emitters*. Appl. Phys. Lett., 2002. **80**(20): p. 3280.

41. G.Z. Yue, Q. Qiu, B. Gao, et al., *Generation of continuous and pulsed diagnostic imaging x-ray radiation using a carbon-nanotube-based field-emission cathode*. Appl. Phys. Lett., 2002. **81**(2): p. 355.

42. Y. Cheng, J. Zhang, Y.Z. Lee, et al., *Dynamic X-ray radiography using a carbon nanotube field emission x-ray source*. Rev. Sci. Inst.. 2004. **75**: p. 3264.

43. J. Zhang, G. Yang, Y.Z. Lee, et al., *A multi-beam x-ray imaging system based on carbon nanotube field emitters*. Proceedings of SPIE, 2006. **6142**: p. 614204: 1-8.

44. J. Zhang, G. Yang, Y. Cheng, et al., *Stationary scanning x-ray source based on carbon nanotube field emitters*. Appl. Phys. Lett., 2005. **84**(18): p. 1841041-3.

45. J. Zhang, Y. Cheng, Y.Z. Lee, et al., *A nanotube-based field emission x-ray source for micro-computed tomography*. Rev. Sci. Inst., 2005. **76**: p. 094301.

CHAPTER THREE

CELLULAR IRRADIATOR SYSTEM DEVELOPMENT AND DESIGN

3.1 Requirements for Cellular Irradiation

Having reviewed a variety of the cell irradiation systems available and in use the key components and requirements for an effective system become clear.

Gerardi in his 2006 article "A comparative review of charged particle microbeam facilities" [1] provides a list of items or capabilities necessary for a microbeam system, stating:

> To design a charged particle microbeam for single-ion single-cell irradiation, the following basic requirements have to be fulfilled:
> (a) The beam spot has to be reduced to a micrometre or sub-micrometre size, corresponding to cellular or sub-cellular dimensions.
> (b) Working with living cells, the beam has to be extracted into air.
> (c) Accelerator beam current has to be reduced in intensity on the cell sample in order to assure a counted particle exposure with high reproducibility.
> (d) A cell visualisation and localisation system, mainly based on a microscope equipped with a CCD camera and coupled to appropriate software.
> (e) A cell micropositioning and/or revisiting system to locate cells under the microscope and place them in the ion beam with high spatial resolution and reproducibility.
> (f) A particle detector to count the number of particles per cell with high efficiency and to provide a trigger signal to a fast beam deflector for switching off the beam when the pre-set number of particles per cell has been delivered.
> (g) A special cell holder to keep cells in humid and stress-free (and sterile, for some specific investigations) conditions during irradiation and to allow cell visualisation and ion detection used for elemental analysis.

We can translate most of these items into a form useful for electron based irradiators. For the first three an electron based system needs a collimator to shape the exiting beam to the 5-10 um range, a window to extract the beam from the vacuum into the air, and an appropriate acceleration voltage to insure deposition of most of the electron beam energy into the cell monolayer being irradiated. The remaining four requirements could be stated as cell microscope and imaging software, a high-resolution cell dish positioning stage, means of ensuring proper dose delivery, and a cell dish capable of bottom side irradiation and compatible with the available microscope systems. We have been able to design, build, and integrate the components mentioned here to develop a functioning cell irradiator.

To fulfill the aforementioned requirements the UNC carbon nanotube field emission based cell irradiator has required the design and construction of a special platform to accommodate its necessary equipment and requirements. To balance and integrate these components several special features have been utilized. Formation of the electron beam of course requires a functioning vacuum system, while a special electronic configuration has been utilized for the high voltages involved in accelerating the electron beam. Furthermore irradiation and observation of cells presented special needs met by the design of several custom components. This chapter will describe the platform for the irradiator and the significance of the various parts of the system.

3.2 High Voltage Set-up

Based on the simulation data discussed in Chapter 1 the irradiation of cell monolayers by electrons is best accomplished when the electrons are accelerated to kinetic

energies of 25-30 kV. Given the typical thickness of the cell layer and the material layers through which the electron beam emerges these energies result in a maximization of the electron energy being deposited in the cell layer. Operating at these energies requires a high voltage power supply to create the necessary potential between the field emission component of the system and the anode/irradiation stage.

3.2.1 Electrical Design

Because the electron beam is generated and accelerated in a vacuum both the field emission component and the anode/irradiation stage must exist in a contiguous vacuum system. In this case a standard stainless steel vacuum chamber was inadequate for supporting the high potential difference. Therefore it was necessary to install an insulating segment to allow for the high potential differences. A cylindrical ceramic vacuum chamber was attached to the top of the stainless steel cross vacuum chamber (Figure 3.1). On the other end of the cylindrical ceramic chamber a custom stainless steel anode/cell irradation flange was attached. The ceramic chamber provides sufficient insulation between the cross vacuum chamber, which resides at the cathode potential, and the anode flange, whose potential is 30 kV higher than the cathode.

With a voltage of approximately 30 kV involved it was necessary to decide which of the two electrodes would be connected to ground as either of these represented the simplest and most feasible of options. Either the anode and its related structures or the cathode and its related electronics would be grounded.

With the anode grounded it would be necessary to float the cathode and multiple electronic components at ~ -30kV during operation of the cell irradiator. This would require

insulating and isolating a large platform from the floor and other conducting objects to avert shorting to ground potential.

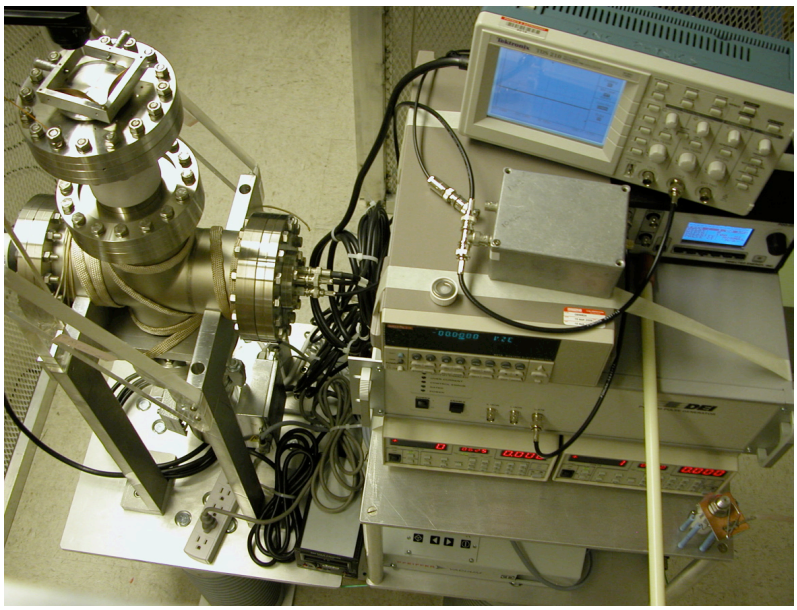

Figure 3.1: The UNC cellular irradiator platform. The cell irradiation stage is to the upper left connected to a ceramic insulating flange allowing for high voltage isolation between the irradiation stage and the remainder of the platform and electronics (right).

With the cathode grounded the insulating platform would be unnecessary, but the anode and irradiation stage would then be subjected to periodic ramp up and ramp down of the high voltage to 30kV above ground potential. Irradiation samples consisting of plated cells in Petri dishes would then be subject to this voltage oscillation with its effects on the cell samples unknown. Additionally a high potential on the anode would present a challenge to placing a microscope over the cell sample. Because the microscope must be positioned within two inches of the anode the microscope would also have to carry a high potential or be liable to arcing between the microscope and the cell irradiation stage. Placing a high potential on the microscope would also require that its light source and CCD camera, connector, and the computer be floated at high voltage.

For these reasons it was determined that the cathode and related electronics should be floated at –30 kV with the anode grounded (Figure 3.2). Either arrangement would require the electrical isolation of large components, but floating the electronics platform as opposed to the microscope viewing system was preferable. Also with the

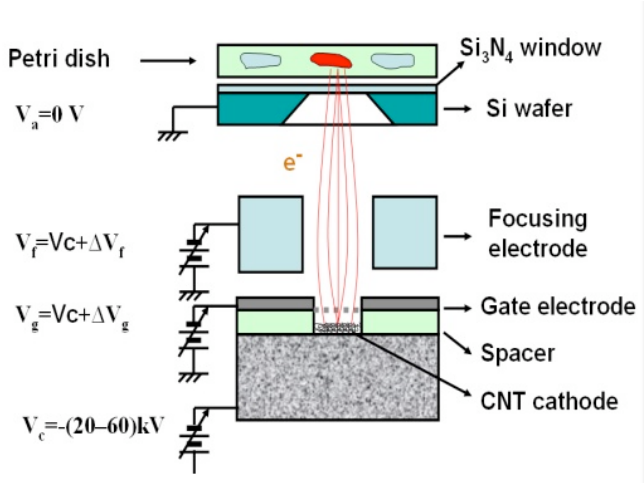

Figure 3.2: Schematic representation of the various system components and the potential applied to each. The cathode is grounded to an adjustable high voltage power supply. Electron acceleration potential can be applied up to -60 kV, but was typically used in between –30 and –20 kV. The gate and focusing electrodes are at voltage 500 to 2000 V above the acceleration voltage applied.

anode grounded the unknowns associated with floating the cells at 30 kV would be removed. The anode was grounded by wire from the irradiation stage to a wall socket ground.

3.2.2 Platform Design

In order to achieve the electrical isolation of the cathode and related components an insulating table was constructed. Normally a standard electron gun or a grounded anode high voltage power supply could have been used to avoid building a special isolation table, but in this case a custom electronics set up was required for our prototype system. Because the various components functioned off standard 120 V, 60 Hz power they would need to be floated.

For that purpose two 18” x 18” aluminum plates were mounted on four high voltage insulators, similar to insulators used in high voltage power distribution to form two table-like platforms for the irradiation system and associated electronics (Figure 3.3).

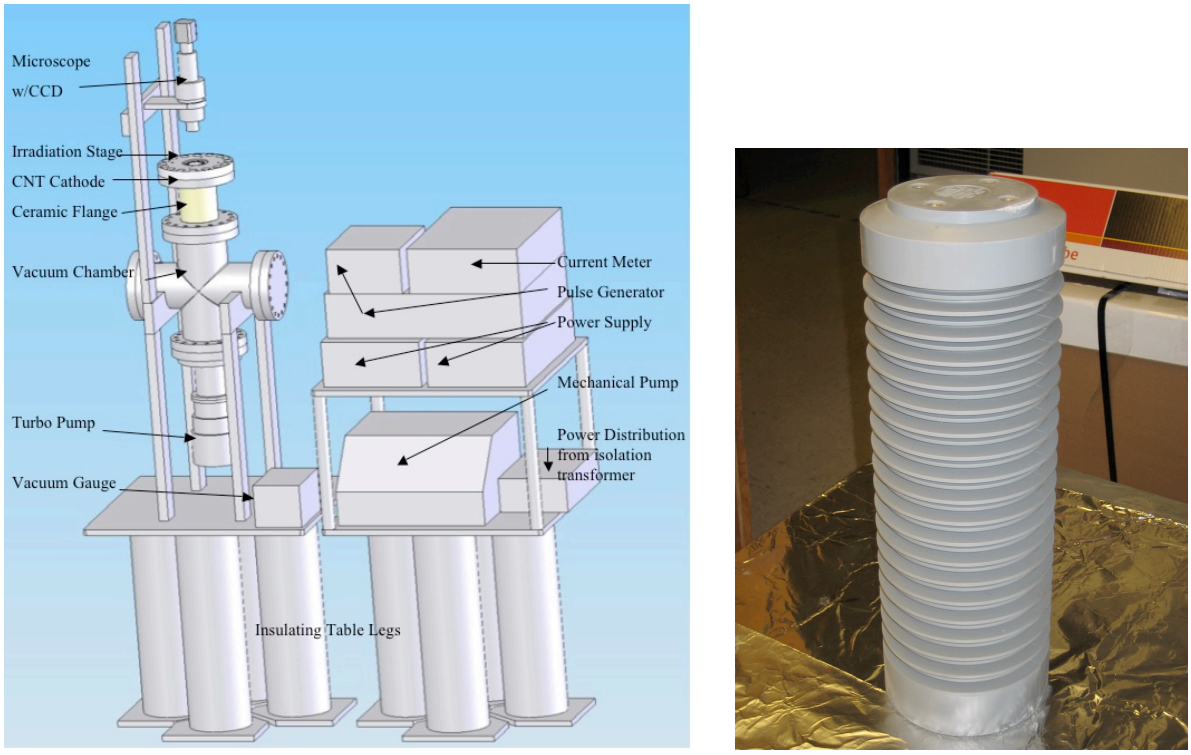

Figure 3.3: (left) Basic system schematic of the UNC cell irradiator with first generation microscope system. All of the components supported by the tables can be floated at high negative voltage with the exception of the microscope and irradiation stage, both of which are grounded. (right) Single insulating table leg capable of insulating up to 60-80 kV. Eight legs are used to support and insulate the two tables depicted on the left.

A frame was constructed to support the vacuum chamber on one of the tables. A vacuum gauge, an electrical feedthrough, and a turbo pump were mounted to the side and bottom flanges of the chamber respectively.

A second table with an additional aluminum plate as a second shelf was used for the mechanical pump and the system electronics. This second table was mainly used in order to isolate the mechanical pump vibrations from the microscope and irradiation stage. This minimized the pump’s impact on the viewing capabilities of the system, which will be

discussed later. The system electronics, which were mounted on this table, consisted of at various times several of the following components: a pulse generator, digital multimeters, high voltage power supplies (~2000 V supply) for gate and focusing voltage, a digital oscilloscope, circuit boards for multipixel connections, and a PC for computerized control of the microbeam system.

3.3 Additional High Voltage Requirements

As stated, during operation the cell irradiation system requires a high negative voltage relative to ground to provide acceleration of the field emission electrons. Usually this voltage is 30 kV. While most of the other components are positioned on top of the insulating tables a few other components enable the high voltage operation of the system, namely the high voltage safety cage, a high voltage power supply, and a high voltage isolation transformer (Figure 3.4).

3.3.1 High Voltage Safety

To ensure safe operation of the CNT cell irradiator during the application of high voltage a grounded aluminum cage was built to surround the system. The cage is composed of an aluminum frame with perforated, expanded aluminum sheet forming the walls of the cage, with a door on one side. The cage is sized such that the walls are approximately 18 inches from the cell irradiator tables, to avoid any arcing between the system and the cage during high voltage operation and to allow users access to the system. The cage is connected to a nearby outlet ground. Additionally a metal grounding hook/electrical discharge rod is connected to the cage. The hook is placed in contact with the system tables following use of

the high voltage so that the system is fully grounded and is not an electrical hazard to the users. During high voltage operation the hook is removed, the cage door is closed, and users are prevented from accidental contact with any high voltage.

3.3.2 High Voltage Power Supply

A high voltage power supply is used to provide an acceleration voltage of ~30 kV for the CNT electron beam. This power supply is connected to the insulating tables in order to float the tables, electronics, and the CNT cathodes at – 30 kV. The power supply is placed outside of the grounding cage for manual user operation and is connected to the insulated table via a high voltage insulating cable which passes over the outside of the cage. By this means the tables, electronics, and CNT cathodes are floated at –30 kV, although it is capable of supplying power up to –60 kV.

3.3.3 High Voltage Isolation Transformer

So far we have not yet addressed how the electronic components on the insulating high voltage table receive the ~120V AC power necessary to operate. Clearly they cannot be plugged into a standard grounded wall socket while also floating at –30 kV. For this purpose a high voltage isolation transformer is used to provide ~120 V AC power at all times to the components resting on the insulating tables, whether floating at high voltage, at normal ground or somewhere in between. The transformer has a 1:1 voltage conversion ratio, but it provides a nominal 60 kV of insulation by isolating the two sets of transformer coils with oil. The oil has a sufficiently high dielectric constant to prevent high voltage breakdown. The system side of the transformer is connected to a circuit breaker that distributes power to outlets to which the various system electronics are connected.

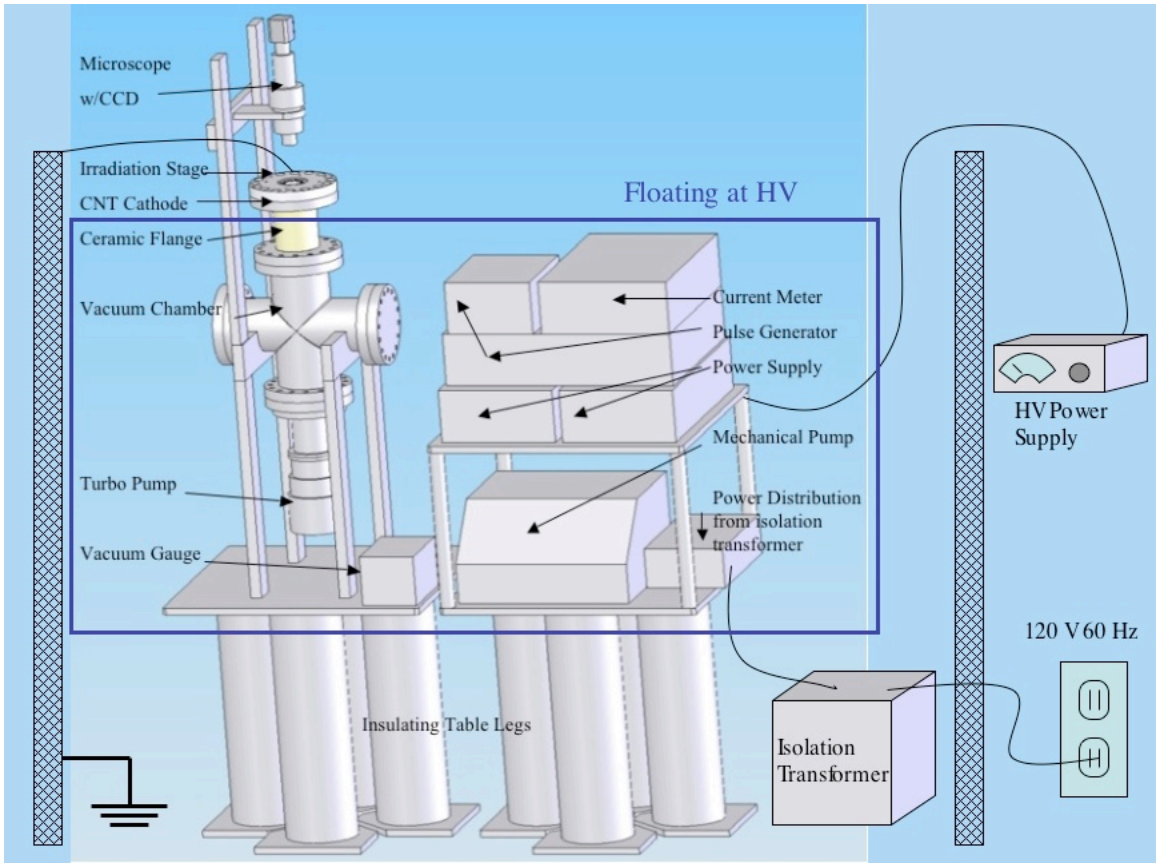

Figure 3.4: The system schematic with the addition of the high voltage components necessary for operation. A grounded safety cage is placed around the perimeter of the system. An isolation transformer connected to a wall outlet provides power to the system while providing a minimum of 60 kV of insulation. The HV power supply resides outside the cage and is connected to the table via an insulating cable. The components of the system isolated at high voltage are enclosed within the blue box outline.

3.3.4 High Voltage Operation

For operation of the irradiator with high voltage it was necessary to properly use the various system electronics. The high voltage power supply was operated from outside the cage. But as stated most of the system electronics were placed on the high voltage insulating table inside the safety cage. Previously it was possible to set all of the electronics to the proper values and with the cathode already emitting electrons to irradiate the cells by increasing the high voltage. Because of the manual ramp up and ramp down of the high voltage and manual timing of the beam on-time this process was grossly inaccurate.

It was determined that while some of the electronics could be set prior to the application of high voltage it was necessary to manipulate some of the electronics during the use of the irradiator. For this purpose we cut several 1 inch diameter holes in the safety cage through which to insert 0.5" diameter, ~30" long plastic control rods. A short length of 0.75" rubber tubing was placed over the end of the rod to assist in the manipulation of buttons and dials on various electronic components. This capability allowed, for example, the activation or deactivation of the pulse generator from outside the system. With the pulse generator operating in pulse count mode it was possible to ramp up the high voltage and then activate the pulse generator. With the electron beam pulses all seeing the same high voltage this resulted in a much more accurate irradiation process and in more accurate reporting of data.

For future phases of the cell irradiator system, particularly the multi-beam system, a computer control method has been proposed. Using a Labview interface signals from a multi-channel output may be used to control the individual pixels via a high voltage MOSFET. In the Labview interface the pulse frequency and width could be controlled for each pixel allowing for variation of dose and dose rate from each pixel. In one embodiment the computer would be floated at high voltage inside the cage and controlled via a wireless mouse and keyboard. Another future option is the use of an optical control link that would allow for control of the computer inside the cage or perhaps provide a link from a computer outside the cage to an output board inside the cage at high voltage. These developments will provide for greater flexibility and versatility for future phases of the CNT based cellular irradiator.

3.4 System Optics and Microscopy

During 2008 we upgraded the Cell Irradiator system to increase its capability and usefulness for radiobiology experimentation. Previously our system used a simple long working distance microscope with a low-resolution CCD device mounted on a 3-axis translation stage, which provided basic viewing capabilities. This was mounted on an insulating plastic frame, which suspended the microscope over the cell irradiation stage. Additionally a simple dish translation stage had been built consisting of two orthogonal micrometer heads mounted in a frame to provide small-scale translation of the cell dish. Both of these components have been replaced with more appropriate equipment for the imaging and analysis of irradiated cells.

3.4.1 System Microscopes

In early experiments with the cell irradiator our first generation viewing system, a long working distance microscope with a simple CCD camera, was used to visualize the irradiation window and cells for alignment purposes (Figure 3.5(a)). This microscope set up provided gray scale images of the dish and the cells but with inadequate contrast to reliably image cells or to easily visualize the electron window position. This was particularly difficult given the lack of an internal light source in line with the optical axis. Instead, at various times, an incandescent light source with a fiber optic gooseneck output and a flashlight were used for illumination. Also the lack of fluorescence or phase contrast capabilities, which are often used to enhance cell visualization, made viewing cells difficult.

As a result this set up did not allow for the in-situ monitoring of cells while in place on the irradiator flange nor did it allow for cell visualization via fluorescence, on which current microbiology research relies heavily.

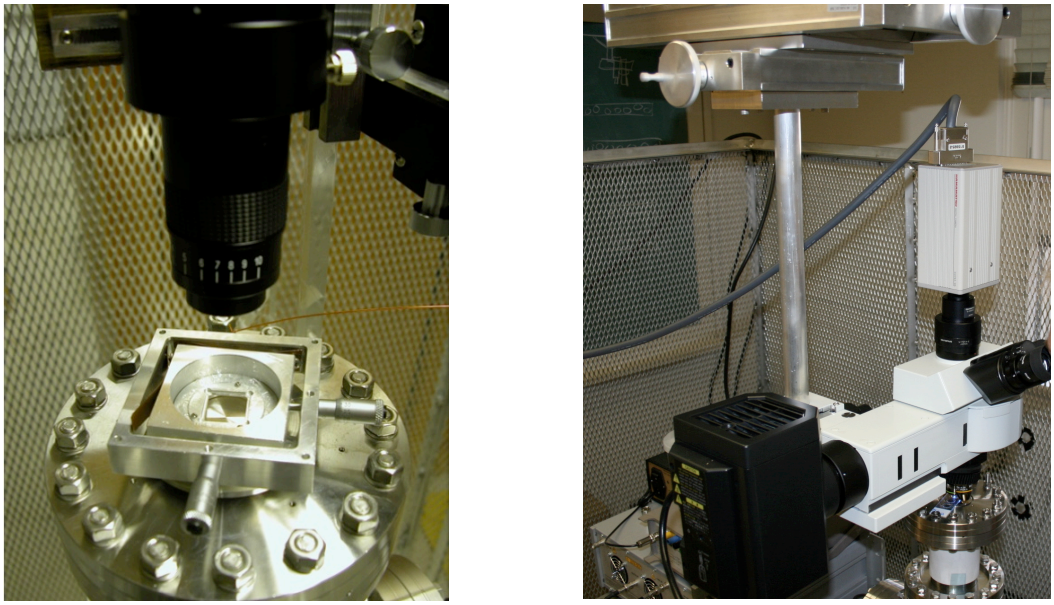

(a) (b)

Figure 3.5: (a) First phase microscope composed of a adjustable magnification telescope and a low resolution CCD camera, but lacking an internal light source. Also shown is the first generation dish translation stage. (b) New fluorescence microscope with multiple objectives, a built in light source. Also shown are the overhead heavy-duty translation stages which allow repositioning of the microscope over the cell dish.

To achieve these capabilities an Olympus upright microscope (Figure 3.5(b)) was purchased and integrated into the existing system. The microscope is outfitted with a Lumen 200 Fluorescence Illumination System from Prior Scientific which uses a metal arc lamp to provide UV/broadband light. The microscope contains filters that allow for the excitation and viewing of common fluorescent stains.

This allows for the visualization of various cell structures, such as the cell wall and nucleus, as well as the foci associated with various cellular processes. Using these capabilities cells can be located and imaged prior to irradiation with the effects induced by irradiation visualized after electron exposure. This is achieved via specific fluorescent

markers which highlight structures or foci of interest. This improvement now allows us to image cells more clearly and in a manner consistent with current methodology. Images are captured via a Hamamatsu C4742-95 CCD camera using Image-Pro 6.2 software. The software allows for the capture of still frame images singly or in sequence. The exposure time for each frame can be adjusted over a broad range to insure proper exposure, and the exposure interval between multiple frames can be adjusted to produce movies.

3.4.2 Microscope Stand and Translation Stage

A custom microscope mount allows the new microscope to fulfill the requirements of the irradiator system. The microscope must be removable, electrically grounded, have 3-axis translation capability, and be relatively vibration free. The mount consists of a steel frame bolted to the floor and wall to give it relative mechanical stability. Two heavy-duty, high-resolution translation stages (Figure 3.5(b)) are connected together and mounted to the steel frame to provide x and y translation. A cylindrical mounting rod is suspended from the translation stages to which the microscope can be attached and positioned at any height over the irradiation stage or can be rotated away. The microscope is stored on an adjacent table on another mounting rod when not in use and can be installed or removed in about one minute.

Microscope fine x-y translation is accomplished via manual operation of the overhead translation stages, which allow for the microscope to be precisely positioned over the irradiation window or an area of interest in a Petri dish. These translation stages, made by Velmex, although manually controlled, have resolution of 5 um or better. Fine z-control is provided by the microscope focus wheel. The microscope, mounting rod, stages, and support plates together weigh around 45 kg. The mounting system's structure is therefore extremely

robust, and in addition to its strength its configuration also provides for the microscope to be grounded so that it is at the same potential as the cell irradiation stage/flange.

3.4.3 Image Stabilization

In initial tests microscope vibration prevented the capture of sharp images via the attached CCD camera. With the weight of the microscope suspended near the unanchored end of the ~24" long, 1.25" diameter mounting rod small oscillations were easily induced and not easily dampened. Because the microscope and the irradiation flange were not mechanically connected vibrations on either component diminished imaging resolution. This challenge has been mitigated via the construction of a stabilization plate mounted between the irradiation flange and the microscope mounting rod (Figure 3.6). The plate attaches to the irradiation flange via three bolting brackets and a single bolt attaches the plate to the bottom of the microscope mounting rod. The rigid attachment of the plate effectively dampens the microscope vibrations and synchronizes the residual vibrations of the flange and microscope.

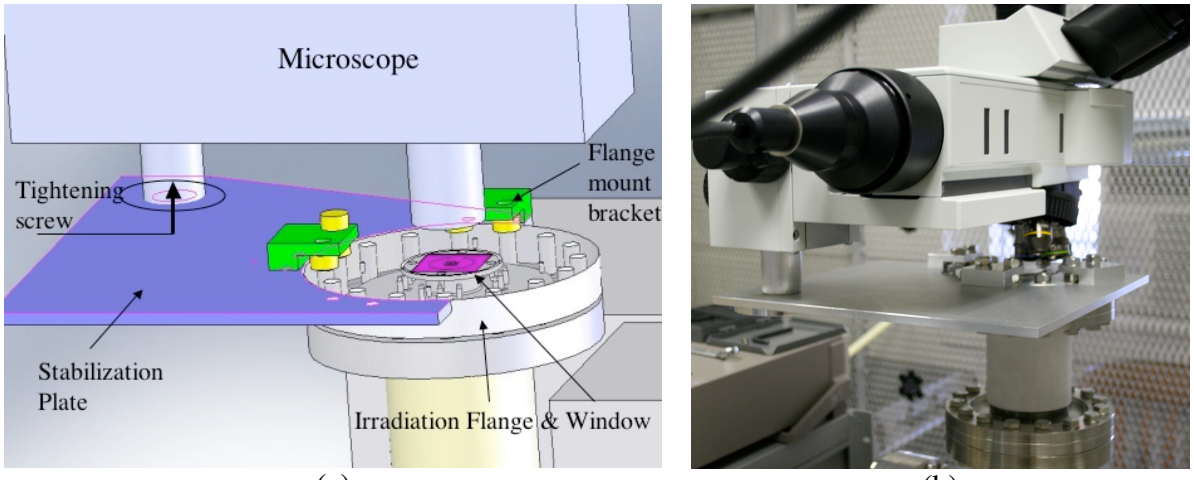

(a) (b)

Figure 3.6: (a) Schematic and (b) image of the microscope stabilization plate. The installation of the plate ties the microscope rigidly to the irradiation stage, removing relative oscillations between the two components.

Stable images of cells, fluorescent foci, and even cell nucleoli have been obtained. Figure 3.7 demonstrates the difference between images captured with and without the stabilization plate in place. In order to quantify the resolution of the system it was determined that the CCD camera had a pixel pitch of 5.9um. These images were taken through the 40x objective using 2x2 binning, therefore each image pixel is [(5.9um)(2)/40] = 0.3 um. In Figure 3.7(a) the cell images are blurry, none of the subcellular components are visible, and the smallest cells measure about 40 ± 1 pixels across or 12.0 ± 0.3 um. For Figure 3.7 (b) the vibrations are dampened and the smallest distinguishable objects, γ-H2AX foci, are approximately 4 ± 1 pixels across or 1.2 ± 0.3 um. In the case of the image without stabilization (3.7(a)) this was not the worst or the best image obtained. In some cases, if the microscope were left undisturbed, the image quality and resolution would improve, and in other cases if the microscope was bumped with more force a worse image would result. Nevertheless this image represents what would be a common occurrence during standard use of an unstabilized scope, such as adjusting the focus knob or bumping the eyepieces with the forehead. It is also possible that the resolution might be improved compared to that in (3.7(b)). For these particular images the exposure time was 0.550 s. If the 2x2 binning were turned off and a longer exposure time was used it might be possible to cut the minimum feature size in half to 0.6 um.

Given the configuration of the system the stabilization plate does produce one minor operational limitation. The vibrations are only fully dampened once a viewing location is determined and a screw is tightened between the plate and the microscope mounting rod. To change locations this screw is loosened, the x-y translation stages are adjusted, and the screw is retightened for the new location.

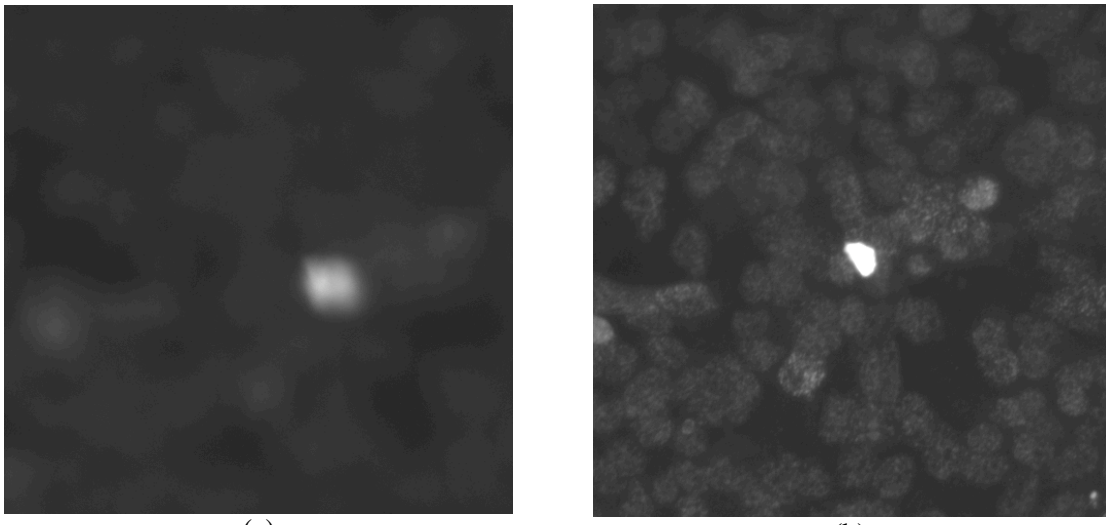

(a) (b)

Figure 3.7: Images from a cell plate without (a) and with (b) the stabilization plate attached. The bright spot is the same location in both pictures. The addition of the plate allows for steady viewing of foci and other cellular structures.

3.5 Cell positioning

For the system to be fully capable of standard cell irradiation experiments the cell dish also needs to be moved and positioned relative to the irradiation window. Whereas the previous dish translation stage was placed directly around the cell dish, the new design allows for a more open arrangement with the translation stage mounted to the side of the irradiation flange with a stiff beam connecting the translation stage movements to the dish (Figure 3.8). This more open arrangement accommodates the new microscope which has a shorter working distance than the previous viewing system.

During some experiments, we found that contact between the cell dish bottom and the window, when covered in Mylar, resulted in "stiction" between the two resulting in stretching of the dish's mylar membrane and resulting in inaccurate translation of the

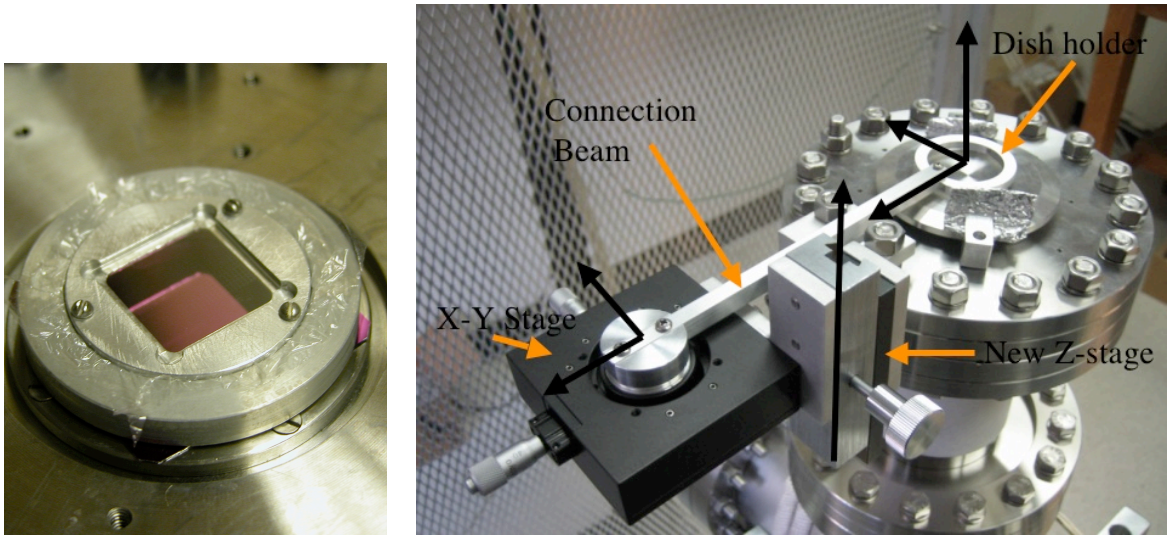

(a) (b)

Figure 3.8: (a) Cell dish positioned over the silicon nitride window chip. The dish fits into the dish holder at right and has a transparent mylar bottom; the violet color of the silicon nitride is visible underneath. (b) Dish translation stage: stage movement is translated to the dish via the connection beam. Z-control is available to lift the dish (not depicted) off the electron window as needed. Dish holder is positioned over vacuum protection flange in image.

cells over the electron window. To solve this intermittent problem we added a z-translation stage for the dish. This allows us to raise the dish, perform x-y translation, and lower the dish back onto the window, avoiding the "stiction". The dish translation stage allows us to move the dish distances as little as a few microns.

Finally the new microscope system has been tested with various cell samples. Cells are viewed at up to 400x magnification. Cells stained with GFP labeled γ-H2AX, Texas Red, and DAPI have allowed for the respective viewing and integration of images of the foci of DNA double strand breaks, the cell wall, and cell nuclei.

3.6 Summary

A platform has been developed which provides for the special needs of a CNT based electron beam irradiator. A vacuum environment has been provided which enables the production of the electron beam. The vacuum chamber, an insulating table, a power transfer system, and safety equipment have been engineered for operation under a floating high voltage. Cell positioning and visualization challenges have been met as well. While cells are most often viewed via transmission illumination most cell irradiator systems prevent that configuration. And while most microscopy platforms consist of an integrated and mechanically fixed system the high voltage requirements of our platform have prevented that. Nevertheless components have been designed and implemented to satisfy these requirements demonstrating unique solutions to the challenges of cell irradiation.

In the next chapter we will discuss the fabrication of two other components which are essential to the system, the CNT based cathode and the electron window, and discuss results obtained. The cathode and the window provide the final components needed and allow this system to function fully as a cell irradiator.

References

1. S. Gerardi, *A comparative review of charged particle microbeam facilities*. Radiation Protection Dosimetry, 2006. **122**(1-4): p. 285-291.

CHAPTER FOUR

SINGLE-PIXEL AND MULTI-PIXEL COMPONENTS AND RESULTS

This chapter will address the most critical elements of this work in developing the UNC CNT field emission based cellular irradiator. In this chapter I will discuss the various electron collimators developed along with the fabrication and testing of the CNT cathodes for the irradiator. These components are the most critical because of their fundamental importance to the project. The collimator serves as the main means by which we can shape and define the beam size, while the cathode produces the electron beam necessary for irradiation. Both single-pixel and multi-pixel collimators and cathodes have been developed and will be discussed.

In addition to these components I will discuss and review the results obtained from both film and cell irradiation. Film has been used to calibrate the beams while cellular irradiation demonstrates the intended purpose of the system.

For this portion of the project our first goal was to first develop a prototype single pixel cellular irradiator based on CNT field emission. All other electron based irradiator systems having been based on commercial electron guns, our goal was to demonstrate a comparable system with similar and if possible a smaller diameter irradiation area.

Second we wanted to develop a multi-pixel electron irradiation system, something which, to our knowledge and review of the literature, has never been done before, with most

systems using a single beam to irradiate multiple locations via shifting the position of the cell dish. The multi beam system could potentially eliminate that or minimize the need for shifting the dish. In the case of the multi-pixel beam, maintaining a small beam diameter was important but not the highest priority for this prototype.

4.1 Electron Window/Collimator Fabrication

One of the more critical components of any microbeam system is the electron window/collimator. For our system in order to form a microbeam capable of irradiating a single cell it was necessary to build an aperture to collimate the beam to a small diameter. We have found that the beam emitted from the cathode is much larger than this small target diameter and will in fact deposit uniform dose over relatively large windows, at least 250 um, as discussed in 4.3.1.3. Apertures of ~5 um are a common size used by other electron beam groups, so this served as our initial target value for making apertures. For the aperture to be useful for CNT cell irradiation it must be covered with a vacuum tight window to allow formation of the beam in vacuum and for irradiation of the cells on the other side of the window which need to be at ambient conditions of pressure. Collimator fabrication was achieved via two different methods. Using silicon microfabrication techniques several different silicon nitride windows were made, and also a laser-drilled aperture in stainless steel foil was used to make a second type of window.

4.1.1 Silicon Nitride Windows

The silicon nitride window was made from a double side polished 400 um thick Silicon wafer with a conformal LPCVD deposited 300 nm Silicon Nitride Si_3N_4 layer,

following the steps illustrated in Figure 4.1(a). Using photolithography, reactive ion etching (RIE), and potassium hydroxide (KOH) anisotropic etching the wafer was etched from one side through to the other with the etch terminating on the silicon nitride. Two properties of silicon nitride make it suitable for this application. First, layers of silicon nitride as thin as several hundred nanometers can be easily electron permeable. Second, silicon nitride is extremely resistant to KOH etching[1], making it an optimal etch mask.

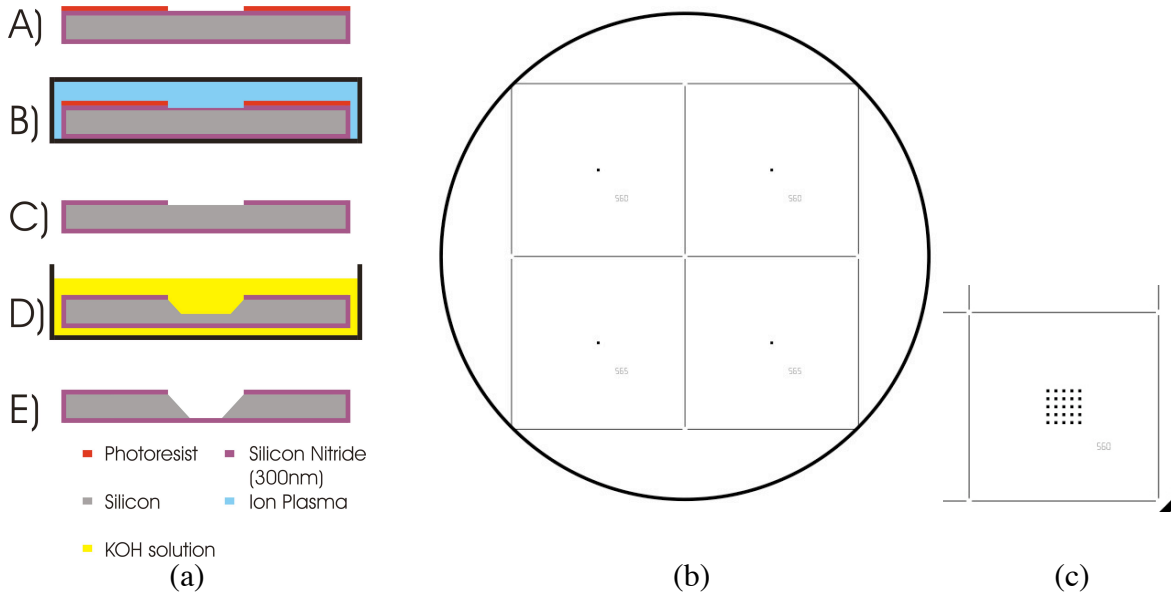

Figure 4.1: (a) Process flow for fabrication of a single silicon nitride window in cross section. A) Patterning the photoresist with photolithography on the nitride layer. B) Etching nitride with RIE. C) Substrate after RIE and photoresist removal. D) Etching the silicon substrate in KOH. E) Completed KOH etching, showing the remaining silicon nitride membrane. (b) Photomask pattern for 100 mm wafer showing 560um squares in the center of each of four window substrates. The lines defining the edge of each chip etch produce a partial etch through the chip (c) Pattern of square holes for the 5x5 membrane window array.

4.1.1.1 Lithography and Patterning

To start the fabrication process the wafer was spin coated with a ~1.5 um layer of Shipley 1813 photoresist, and exposed with a negative of the mask pattern as seen in Figure 4.1 (b) to open up square patterns in the photoresist as well as long rectangular features to define the edges of the four chips on each wafer. Here the central square pattern in each

quadrant is approximately 560 um on a side. This dimension was chosen so as to leave an approximately 5-10 um window on the other side of the wafer. The long rectangular lines were drawn to form grooves that would be etched down partially through the wafer. Drawn at a width of 200 um they would reach a calculated etch depth of ~141 um. This depth was deep enough to assist with separating the wafer into four separate window pieces while also holding the wafer intact during normal handling. This eliminated the need for manually cleaving the wafer or for dicing the chips with a wafer saw; the former method can often result in an imprecise wafer cleave location while the latter process would have presented challenges to preserving the thin silicon nitride window.

After exposure the wafers were developed in MF319 developer for 60 s with moderate agitation. The features depicted in black in Figure 4.1(b) developed away leaving the remaining surface of the wafer covered in photoresist.

Prior to the etch step a hard bake was performed; the photoresist was baked at ~125C for 60 seconds on a hotplate to reflow and harden the resist prior to reactive ion etching (RIE). The wafer substrate was then etched for 4-5 min in a SAMCO RIE-1C model etcher using Octofluoropropane (C_3F_8) and Oxygen. The C_3F_8 flow rate was set to ~4.5 sccm delivering a pressure of 125 mTorr. Also a small quantity of oxygen was flowed into the chamber to add an additional 12.5 mTorr of gas into the system for a total pressure of 137.5 mTorr with the plasma off. RF power generation was supplied to the system in the capacity of 80W. Etching was often performed for 3-4 minutes, followed by an inspection of the nitride layer. The edges of the wafer tended to etch faster and clear first. Also after etching was complete towards the edges some accumulation of etch polymer seemed to take place on to the exposed silicon; this could easily be misinterpreted as an incomplete etch, but in fact

the opposite was the case. It was observed that when the nitride layer was almost completely etched that the nitride layer took on more intense colors, blues, yellows, and some browns, as these indicate very thin nitride. This is readily apparent after comparison against charts of nitride color vs. thickness[2]. As additional etch time was needed wafers were reloaded and etched for additional intervals of 15-60 s until all of the areas unprotected by photoresist were clear of nitride. After the nitride was etched the photoresist was stripped from the wafer in piranha etch, a ~4:1 H_2SO_4/H_2O_2 mixture, or in some cases in an N-methyl pyrrolidone (NMP) solvent.

4.1.1.2 Through wafer etching via KOH

Next the substrate, now with square and rectangular openings in the silicon nitride layer, was etched in Potassium Hydroxide (KOH) aqueous solution. The KOH solution etches certain crystal planes in the silicon faster resulting in an anisotropic etch. For a standard (100) oriented silicon wafer the face of the wafer is oriented to the (100) plane and the flat is generally aligned to the <100> direction. Because the etch rate of the {111} planes is so vanishingly small compared to the {100} planes the {111} planes approximately function as an etch stop. In the case of the standard wafer described above the {111} planes intersect the (100) plane of the wafer at angles of 54.7˚ intersecting with the plane of the wafer along lines parallel and perpendicular to the wafer flat. Depending on the shape and dimensions of the feature patterned in the nitride layer a variety of structures can be produced, from trenches to pyramidal pits, as well as membranes (Figure 4.2).

For the purpose of forming nitride membranes it was necessary to etch all the way through the 400 um wafer. By defining the size of the etch pattern in the nitride on the first side of the wafer it was possible to approximately determine the window size. Assuming

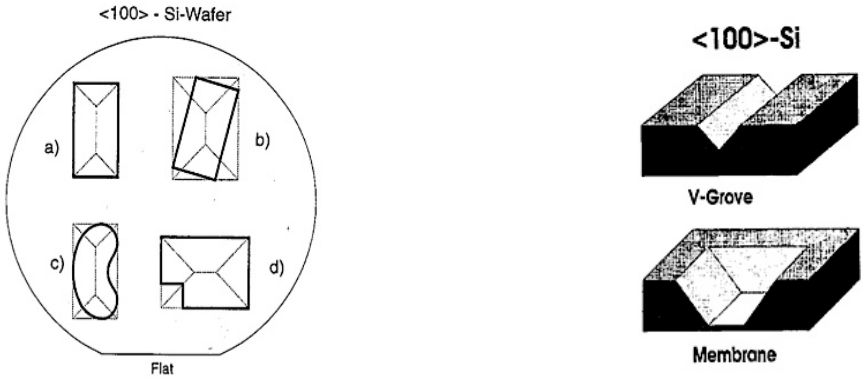

(a) (b)

Figure 4.2: Types of etch holes produced by the etching of (100) silicon via KOH. (a) Various mask hole shapes and their resultant etch pit shapes. (b) Cross sectional diagrams of a trench or v-groove structure and a membrane fabricated by KOH etching of (100) silicon. Features that are insufficiently large compared to the thickness of the wafer will terminate in a trench, while larger dimensions will result in membrane structures. Reproduced from reference [3].

a zero etch rate in the {111} planes a simple geometric calculation can be performed relating the feature size to the final etch depth. In a wafer of sufficient thickness, for a square opening in the nitride aligned parallel to the <100> direction the terminal etch depth, d, is related to the feature width, w, by the following equation:

$$d = \left(\tan(54.7)\right)\left(w/2\right) \qquad (4.1)$$

In this case the etch terminates in a point or, in the case of a rectangle, a line because the wafer is thicker than the maximum etch depth. For the case were the wafer is thinner than the maximum etch depth another useful calculation can be performed to determine the square nitride opening size, w_i, necessary to achieve a silicon nitride membrane window of a particular width, w_f, with a term for the wafer thickness, t_w:

$$w_i = \left(2t_w/\tan\left(54.7\right)\right) + w_f \qquad (4.2)$$

Given the angle of intersection of the crystal planes, the thickness of the wafer (400 um), and the target of a 10 um x 10 um square membrane it was possible to calculate, using Equation 4-2, that a square hole 576 um on a side should be etched in the nitride. This initial

value was used for the first set of lithography masks, but the wafer yielded membrane windows in the range of 25-30 um on a side. After several experiments this dimension was eventually reduced to 560 um to account for various forms of process bias. Some of the sources of this process bias may have included inaccuracy in wafer thickness, possible bias in the lithography and RIE steps, and nominal etching of the {111} planes.

Wafers are manufactured to tight tolerances, but variances in wafer thickness result in changes in the size of the window or possibly prevent a window from forming should the wafer be too thick. Batches of wafers vary in their quoted thickness tolerance, with some ± 5 um and others ± 20 um. Two batches of wafers were used over the course of this project. Unfortunately the first batch lacked thickness tolerance data and for the second batch it was not possible to confirm the listed tolerance given the lack of appropriate measurement equipment. This led to some variation in the etching process, such as enlargement of the window when etching a thinner wafer.

Bias in the lithography and RIE steps also affected the final feature size and required altering the starting dimension. In lithography the pattern dimension may not be accurately transferred to the photoresist. In this case in which a positive photoresist is used with a dark field mask, poor mask to wafer contact as well as overexposure are factors that may contribute to feature enlargement, increasing the size of the window.

For KOH etching an additional challenge is that of the alignment of the photoresist pattern to the flat and the degree to which the flat approximates the <100> direction. Either of these factors can result in rotation of the square pattern away from a parallel configuration, which naturally would increase the outer dimension of the pattern, resulting in undercutting

of the nitride layer and making for a larger than expected feature (Figure 4.3). These factors may together be additive or subtractive depending on their relative rotational directions.

Another factor in the process is that of the degree of anisotropy, defined in this case as the degree or ratio to which the {111} planes are etched in comparison with the {100}. While the etch rate in the {111} planes can be very low, 1% or less of the {100} etch rate, some factors can cause this rate to increase and consequently to result in more undercutting of the nitride and a larger than expected membrane window size.

All of the wafers etched in this process were etched in 22wt% KOH solution, by dilution from a 45wt% KOH stock. This concentration demonstrates the highest etch rates for (100) silicon[3]. At 70C and 80C the silicon etch rates in the KOH are approximately 1 and 1.4 um/min respectively[1, 4]. Wafers were generally etched in this temperature range. In some cases it was found that etching at or around 80C produced greater roughness of the silicon surface. This resulted in some stair stepping along both the {111} and {100} planes as well as some pitting in the normally planar etch surfaces (Figure 4.3). Although surface roughness measurements were not made the roughness was readily apparent visually. One result of this roughness seemed to be faster etching of the {111} planes and consequently a reduction in the anisotropy of the etch process. This resulted in the enlargement of the membrane window size as mentioned above.

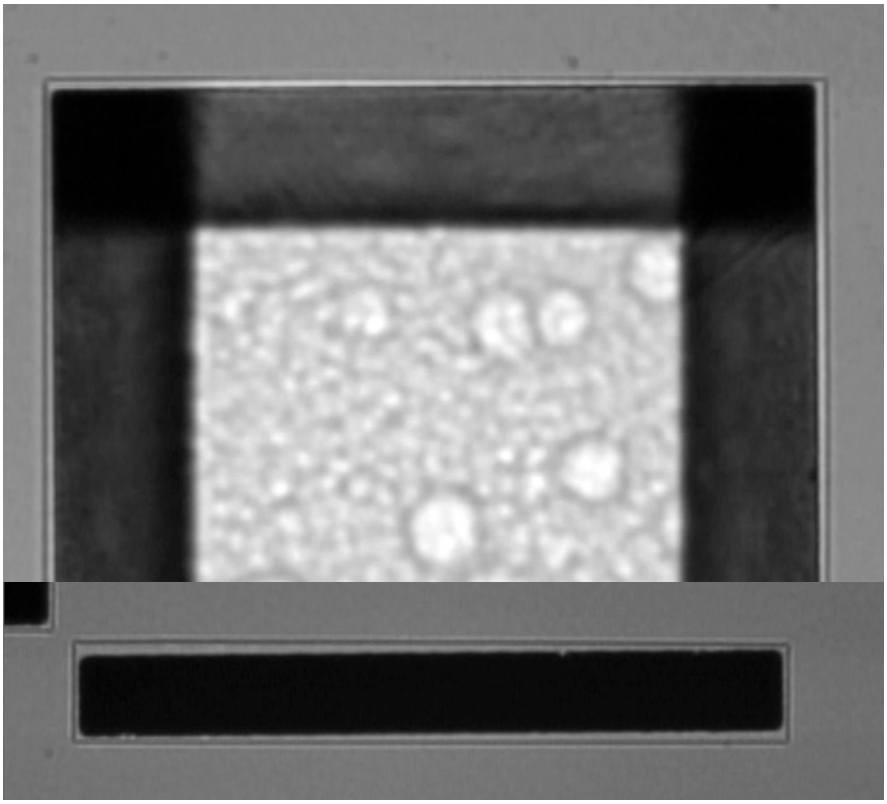

Figure 4.3: (Top) Optical image of partially etched KOH hole in silicon exhibiting several factors producing variation in etch results. In the center pitting is present on the (100) plane, on the {111} side planes visible striations indicate a defect induced overetch, and at the edges nominal undercutting of the silicon nitride is visible along with a moderate rotational differential between the lithography and the crystal orientation of the silicon. All result in enlargement of the etch width. (Bottom) Image of a narrow etched trench, used as part of a labeling scheme, showing a similar rotational difference and the resulting enlargement of the trench.

While the source of this loss of anisotropy was not immediately apparent this problem was only observed when using the second batch of wafers from which the nitride windows were fabricated. Probable sources of this overetching in the {111} planes are elevated oxygen impurities in the wafers and increased thermal cycling. Data exist to show that these two factors work independently and in conjunction to cause a reduction in the anisotropy ratio between {100} and {111} reducing this ratio from as much as 100:1 down to as little as 20:1 [5, 6]. It is thought that interstitial oxygen defects, particularly in elevated concentrations, accumulate and precipitate in the bulk, especially if the wafer has undergone

multiple high temperature thermal processing. Elastic stresses from these precipitates induce dislocation defects which create gaps in the otherwise slow etching {111} planes, resulting in a faster apparent {111} etch rate. While the oxygen content of the wafers used in this work was not known this explanation closely describes the increased undercutting and surface roughness observed despite use of the same process conditions for the first batch of wafers. Also the effects as described in these references match well with the observed effects in our wafers. A reduction in the KOH etch temperature to around 70C seemed to mitigate this effect and result in a smoother etch, with the lower temperature possibly resulting in a better differential etch rate between the silicon and the oxygen related defects. It is not known if all of the wafers in the batch were susceptible to {111} overetching, but as the reduction in etch temperature seemed to solve this problem it was not investigated further. Windows with small dimensions were subsequently fabricated from this batch of wafers without further reduction in the patterned dimension.

For each experiment the etch time was approximately 6 hours. Water was periodically added to the solution to bring it back to its original volume and concentration. Periodically during the etch process the wafers were removed and etch depth was measured using a micron graduated focus knob on a standard optical microscope. Etch rate could be calculated and approximate etch time remaining calculated. After sufficient etch time the silicon was removed revealing the silicon nitride membrane, which when viewed as an isolated membrane appeared yellowish green. This allowed one to confirm that the silicon was completely etched, and that only the nitride was remaining.

4.1.1.3 Fabrication results

Using the techniques mentioned above a large number of single window and multi window chips have been made. Initially a large number of different windows were produced. Several of the first windows made were square windows 250 um on a side; one of these windows was later used for experimental work as discussed subsequently. Single windows with side measurements of ~ 20 um (Figure 4.4(b)) were made and used in many of the single pixel irradiation experiments. The smallest KOH etched window made was measured by SEM at 3.5 um x 6.5 um, as illustrated in Figure 3c. In addition to these single window chips, multi window chips were also fabricated with a 5x5 array of etch holes (Figure 4.1(c)). In particular one multi window chip was etched with all the windows ranging from 9 to 13 um on a side. Film and cell irradiation data from these windows will be presented in the next chapter.

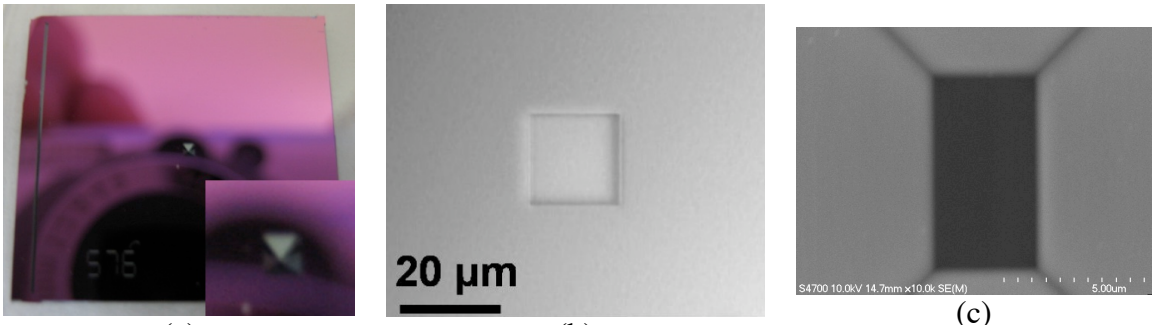

(a) (b) (c)

Figure 4.4: (a) Chip with a single nitride window etched in the center seen from the etched side with the inset showing detail of the inverted pyramidal structure. (b) 20 um window used for cell irradiation seen from the topside. (c) SEM image from the etched side of a 3.5 um x 6.5 um window showing the slope and intersection of the {111} planes.

4.1.2 Laser Drilled Aperture

To form an alternate collimator/window a 5um diameter laser drilled aperture in a 50um stainless steel foil was obtained. A ~3 um Mylar film was affixed to the foil with an

adhesive to form a second type of window. This aperture provided a ~10:1 aspect ratio for the electron collimator which was an improvement over the KOH etched windows, whose sidewalls were sloped at 54.7˚. The large angle of the KOH etched apertures would theoretically allow electrons to pass through the window at much higher angles whereas the laser drilled aperture had a more limited angular range.

In the case of both the silicon nitride window chip and the laser drilled aperture/Mylar window each was attached to a central inset flange (mini-flange) of the anode/irradiation stage. The mini-flange sits at the center of the irradiation stage with an O-ring seal between the mini-flange and the rest of the chamber forming the final vacuum seal.

The techniques used here in making the nitride windows as well as the laser drilled aperture were also used to form a large KOH etched 250 um x 250 um window as well as a laser drilled double slit structure with 2mm long, 5 um wide slits in a 50 um foil. These were used for additional irradiation experiments, the data from which we will present subsequently.

4.2 Fabrication and Characterization of CNT Cathodes

While the electron window/collimator is essential in forming a microbeam the CNT electron cathode is the more unique aspect of this work. The particular nature of beam formation sets this system apart from other existing systems and ultimately enables the unique direction of our research, the development of a multi-pixel system. CNT based field emission cathodes have certain advantages over conventional thermionic cathodes in terms of low operating temperature, instantaneous response time, cathode design flexibility, and potential for miniaturization. Thus CNT field emission technology is ideal for the proposed

multi-pixel electron microbeam cellular irradiation system, which is capable of high temporal and spatial resolution irradiation to user specified multiple cellular regions. This section will describe the formation of the single and multi-pixel cathodes and their subsequent testing.

4.2.1 Single Pixel Cathode Fabrication

The CNT cathode used in the single pixel system is a composite film deposited onto a metal substrate using electrophoretic deposition (EPD) following the procedures we have previously discussed[7, 8]. The CNTs used for this cathode were small-diameter multi-wall carbon nanotubes provided by Xintek and were used as the source material for the EPD ink. The CNT cathode produced for the single-pixel system was a 1mm diameter area of CNTs deposited onto a stainless steel substrate.

This cathode was fabricated from a stainless steel screw. One end of the screw was cut off flat and polished to a smooth surface. The smooth end of the screw was then covered with a threaded Teflon cap with a 1 mm diameter hole drilled in its center. This served as a mask for the electrophoretic deposition (EPD) process with the rod serving as the EPD substrate. Electrical connection was made to the rod by the attachment of a wire. Because the entire EPD assembly would be immersed in the EPD solution and prone to CNT deposition any exposed portions of the rod were covered with Parafilm to avoid unwanted CNT deposition. The 1 mm diameter area inside the Teflon cap was therefore the predominantly exposed area.

For the EPD process the deposition substrate and a counter electrode are immersed in the various solutions of deposition material as has been described earlier. A current of the proper polarity is passed through the solution between the electrodes, inducing the material to move towards and moderately bond with the substrate. If the two electrodes approximate a

parallel plate configuration the area of highest deposition will be in between these two plates as the distance between the two is minimum.

The EPD process requires properly prepared solutions to achieve good results. In our case the EPD process was performed as a two step process. The first solution utilized was a solution of glass frit particles and CNTs in an ethanol/water mixture with $MgCl_2$ as the salt charger. The second was an additional solution of CNTs only. First the solution of glass particles and a moderate concentration of CNTs was used to deposit the first layer of the CNT cathode. A voltage/current of 5 mA was applied to the substrate for a period of 15 seconds leaving behind a visible film of the particles. Next the second solution with a higher concentration of CNTs was used to deposit an additional top layer of CNTs at a voltage of 2 mA for 20 seconds. Following deposition the substrate was removed, the Parafilm was removed, and the Teflon cap unscrewed to reveal the ~ 1mm circle of CNT/glass composite. The EPD materials maintained moderate adhesion following the process.

After the EPD process the substrates were annealed for 60 min at 500°C in a vacuum annealing furnace. The annealing process, at the selected temperature, results in the flowing and fusing of the glass particles, resulting in a good bond with the substrate and fixing the CNTs in the glass matrix. The cathode is then mechanically stable and the CNTs are also electrically connected to the underlying substrate.

4.2.2 Incorporation of cathode into cathode assembly

After fabrication the single pixel cathode was placed into a custom designed cathode assembly. The CNT based single-pixel electron microbeam cellular irradiator, as illustrated in Figure 4.5, contains a CNT field emission cathode, a metal mesh gate electrode, an

electrostatic focusing lens, and an anode with a collimator and the silicon nitride electron-transparent exit window.

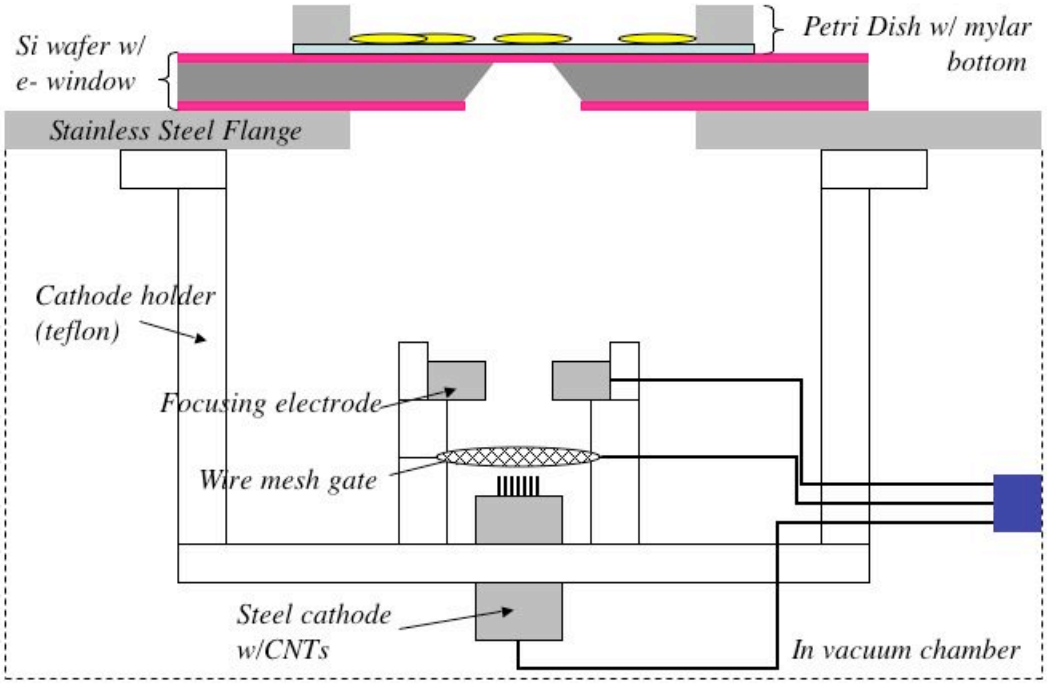

Figure 4.5: Cross-sectional schematic of cathode set up and electron window.

The body of the single-pixel CNT cathode assembly was machined from Teflon block, chosen in this case for ease of machining as well as robust electrical insulation. The design allows for the CNT field emission cathode, the metal mesh gate electrode, and the electrostatic focusing electrode to be placed in close proximity to one another while maintaining necessary electrical isolation. Electrical connections to the various components were provided by Kapton insulated wire fed through holes drilled into the Teflon. The stainless steel screw substrate was threaded into the assembly with a spacing of approximately 200 um to the gate electrode, allowing for easy extraction of electron current for the irradiator.

The as-fabricated single-pixel cathode was placed in its assembly and installed into the vacuum chamber. In the vacuum chamber Kapton coated wire was used to connect the

cathode, gate, and focusing electrodes to a high voltage vacuum feedthrough. On the outside coaxial cable was used to connect the components to the proper sources. The CNT cathode consisting of the polished screw was connected to ground via a 500 kOhm resistor and a multimeter used to measure current. The gate and focusing electrodes were connected to high voltage power supplies capable of several thousand volts via coaxial cables. The gate electronics in particular consisted of a high voltage input sourcing a pulse generator. By this means the gate voltage was pulsed so as to moderate the current produced by the cathode. The pulse width was variable from 25 ns to DC.

4.2.3 Field emission test of single-pixel cathode

The cathode was tested for field emission and supported a moderate current of 2-5 uA at a gate voltage of around 700 V. Higher currents were achieved using higher gate voltages, but this particular application did not require higher currents as the 2-5 uA current was found to easily to bring about the desired level of irradiation.

4.2.4 Multi-pixel cathode fabrication

For the multi-pixel system an early goal was to develop an array of as many as 10,000 individually controllable pixels. Given this was our first foray into a multi-pixel irradiator fabrication a smaller array was chosen. In this case a 5 x 5 array of 25 pixels was selected as it was judged to be able to demonstrate the functionality of a larger multi-pixel array. The pixel to pixel spacing, 1.5 mm, of the array was chosen from an earlier plan to use an existing cathode array chip with this spacing between cathodes. The minimum spacing achievable between two pixels would have been about 600 um as 500 um was the target size for the

circular cathodes being made. Also the array required an interconnection layout of lines approximately 200 um in width as well as adequate spacing between the cathodes.

While these factors helped to define the spacing the consideration of the array size was impacted by other considerations. One initial consideration was the chip to vacuum flange interconnect scheme. Because the insulating ceramic chamber chosen had such a small inner diameter, 2.4 inches, the number of connections possible in that space along with the cathode assembly was limited. The estimated maximum using the planned interconnect scheme was around 30. Also the high voltage insulating, multi-pin feedthrough flange available for our chamber set-up also had a maximum connection pin count in the neighborhood of 30. These along with the desire to fit the full array of cathodes within the diameter of the cell dish design resulted in the 5x5 array.

Because the 5 x 5 array design affected the design of a large number of parts for the system starting over from scratch with a new array size was not a real option. Nevertheless this array provided a good starting point for the evaluation of this first generation system.

4.2.4.1 Multi-pixel cathode substrates

In the case of the multi-pixel cathode rather than using a stainless steel rod as the substrate a silicon oxide on silicon and a glass substrate were used. These substrates, both being nominally insulating, allowed for the multi-pixel cathodes to be individually addressable by forming metal patterns on their surfaces.

Figure 4.6 (a) shows the second and final design version of the CNT cathode array. In the first design all 25 of the contact pads were located on one side of the cathode. It was originally thought that this would make connection to the cathodes easier, but this also required that all 25 connections would have to be arranged in a more compact area, rather

than spreading them out onto two different sides as with the final design. The small, 2.4 inch, inner diameter of the ceramic chamber, mentioned above, made this scheme more challenging. With a cathode size of 1.2 in. x 1.2 in and a diagonal of 1.7 in. this left very little room on either side of the cathode for the cathode assembly and the individual cathode connections. Therefore the cathode layout was redesigned to accommodate this parameter.

In the case of the silicon wafer substrate a negative photoresist was used to form a negative pattern on the substrate of the desired metal line structure (Figure 4.6(a)). The silicon oxide layer on the silicon wafer was 4um thermal oxide. Next a Chrome and Copper metal layer was applied to the substrate via a magnetron sputtering system. The Cr was 600 Å and the Cu 1600 Å. Next a lift off was performed in Acetone or NMP to remove the photoresist and the metal layer deposited over the top, while the metal bi-layer adhered well

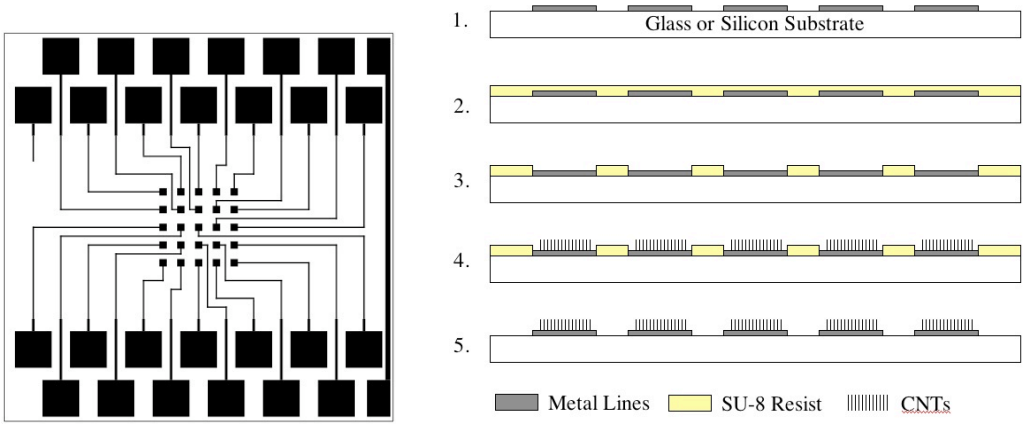

(a) (b)

Figure 4.6: (a) Layout of the multi-pixel cathode. The black structures represent metal. From the outside are electrical contact pads, connecting lines, and the central 5x5 cathode material locations. (b) The EPD fabrication process: (1) Substrate with metal pattern. (2) Spin coating of SU-8 photoresist. (3) SU-8 is exposed and developed to reveal holes over metal pads. (4) CNT cathode material is deposited via EPD. (5) SU-8 is removed via lift-off in N-methyl pyrrolidone (NMP).

to the silicon surface. In the case of the glass substrate, XinNano, Inc. was employed to form a screen printed silver reproduction of our custom pattern on 1.1 mm thick glass using their proprietary processes. The glass was diced to size using a dicing saw.

4.2.4.2 Lithography for EPD

Following the definition of metal lines the next step was to prepare the susbstrates for EPD (Figure 4.5(b)). In the case of both the SiO_2/Si and the glass substrate a mask was formed using Microchem SU-8, a special purpose negative epoxy resin photoresist. The exposed SU-8 layer is rendered impermeable to the alcohol based EPD solutions, where other photoresists would experience dissolution, making it an excellent EPD template. Also the negative formulation along with its high transparency result in the resist pattern transferred having very high aspect ratio sidewalls. This better confines the EPD materials during deposition to the target areas and results in a better CNT/glass particle pattern following the lift-off.

SU-8 10 was used to form a 10 um resist layer. First an undercoat layer of Omnicoat was applied at 3000 rpm for 30 s. As the SU-8 resist can be extremely adherent after processing this layer allows the resist to be removed more readily. The Omnicoat layer was baked at 200°C for 1 min on a hotplate, the thickness of this layer being on the order of a few hundred nm. Next the SU-8 resist was spin coated at 3000 rpm for 30 s, soft baked on a hot plate for 2 min at 65°C and 5 min at 95°C, exposed through the mask with 180 mJ of UV light, post-exposure baked for 1 min at 65°C and 2 min at 95°C, and then developed in SU-8 developer for 2 min[9]. Finally an additional develop step of 30 s in MF-319, an alkaline aqueous developer, was used to remove the Omnicoat from the patterned deposition holes.

4.2.4.3 EPD Procedure

The photoresist pattern defined a 5x5 array of 0.5 mm holes centered on the cathode pad array in the center of the chip into which CNTs would be deposited. The pattern also left the outer contact pads uncoated so as to allow electrical contact. In order to perform the EPD process on mutliple pixels simultaneously it was necessary to electrically connect the 5x5 array. Although the pixels might have been processed separately the simultaneous deposition would insure greater uniformity. This was achieved via the application of a temporary silver paste to the contact pads arrayed on each side of the chip.

After the silver paste was dried each pad and pixel was probed for electrical continuity. A bridging connection line allowed connection of the pixels on both sides of the chip. The side of the chip to be immersed was wrapped in Parafilm to avoid material deposition to the silver paste and contact pads. Electrical connection was made to the opposite (unimmersed) side of the chip. At other times the deposition process was performed on one side of the chip at a time, as this left the chip cleaner after removal of the silver paste.

As with the single pixel cathode process similar deposition solutions of glass particles and CNTs were used in a two-step deposition process. The charger used in the deposition was $MgCl_2$, and accordingly the target substrate was made the negative electrode. The first solution consisting predominantly of glass particles was deposited for 30 s at ~500 Volts and a current of ~0.2 mA. The second solution containing more CNTs was then deposited for 15 s at ~300V and 0.1 mA.

4.2.4.4 Lift-off and annealing

Following deposition the SU-8 photoresist layer was removed using NMP. The NMP was heated to 80ºC if lift-off did not occur readily at room temperature. This lift-off

process serves to better define the edges of the CNT cathode. Any CNT material hanging over the edge of the photoresist pattern is typically removed leaving a relatively smooth circle of CNTs on the cathode. The silicon and glass multi-pixel substrates were annealed in a vacuum furnace as described earlier for the stainless steel rod cathode (Figure 4.7).

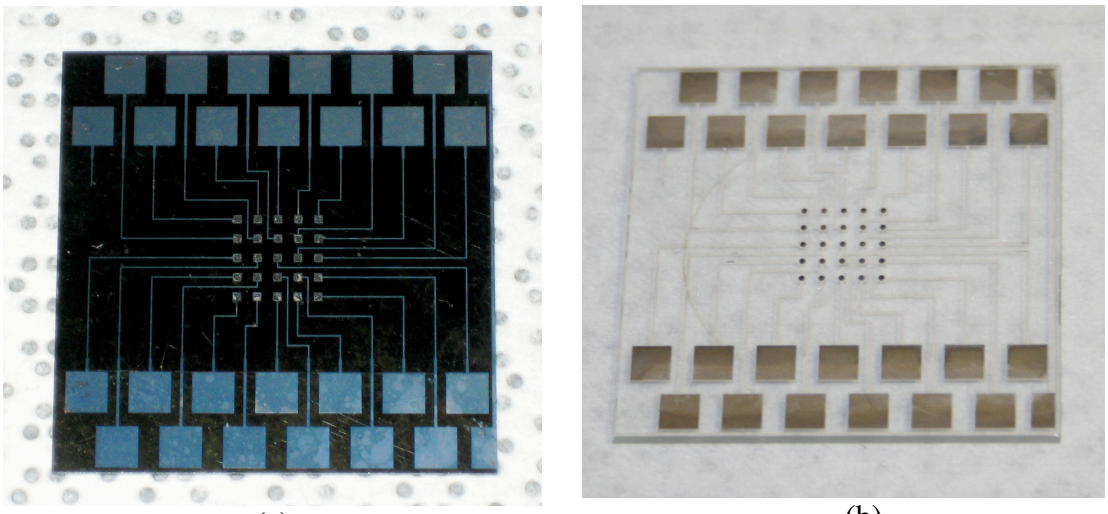

(a) (b)

Figure 4.7: As fabricated cathodes on (a) silicon oxide on silicon and (b) glass substrate following EPD and annealing. In the center is the 5x5 CNT cathode array.

4.2.4.5 Activation and cathode morphology

The cathodes also underwent an activation step consisting of several, typically three, iterations of tape contact and removal, using at times Kapton tape and at other times a low tack wafer dicing tape. The Kapton tape was used on the silicon cathodes, but it was necessary to use the low tack tape on the glass substrates as the Kapton as well as Scotch tape resulted in partial lifting of the printed Ag lines. The taping process served to remove any unattached debris, whether nanotube or otherwise, from the cathodes, which could have caused non-uniformity in the cathode to gate distance. It is also thought to improve field emission results by peeling up nanotubes from the surface of the cathode into a more vertical

orientation. This effect was not quantified in these experiments, but the taping was nevertheless essential in removing unwanted debris, which might have otherwise become vaporized or otherwise introduced instability during field emission testing.

Figures 4.8 & 4.9 provide some images of cathodes fabricated on the silicon oxide on silicon wafer and the glass substrate. Optical microscope images of a single cathode from the 5x5 array can be seen before and after taping (Figure 4.8). The CNT composite material is deposited approximately on the center of the pad, although the cathode is not perfectly circular, possibly as a result of adhesion problems in the SU-8. The difference

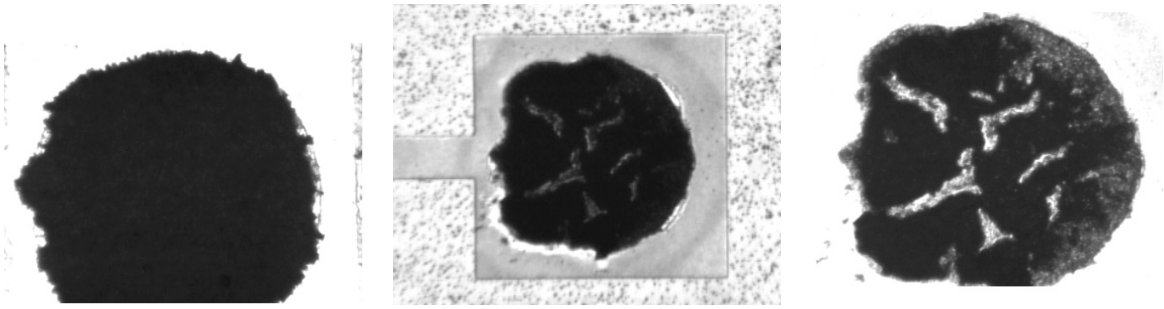

(a) (b) (c)

Figure 4.8: Optical microscope images of a single pixel following EPD and annealing. (a) Pixel pre-taping showing a relatively uniform CNT/glass film. (b) Pixel post-taping showing arrangement on cathode pad and some removal of deposited, although potentially loose material. Cathode is not perfectly round as a result of possible SU-8 adhesion loss. (c) Higher mag image of pixel shows regions where deposited material has been removed, along with some height differential.

between an untaped and taped sample can be seen, showing the effects of the taping procedure in removing poorly adherent material. SEM images (Figure 4.9) show the pre- and post-taping surface of several cathodes in the array. Debris is removed from the cathodes as well as the chip surface. The morphology of the CNT/glass composite is clear under higher magnification SEM. The glass has fused together, and the CNTs are imbedded in the glass in an isotropic manner. Some CNTs protrude through the surface of the glass and will function as field emitters. Other CNTs embedded in the surface may not have a complete connection

to the conducting metal lines through the glass and will therefore not serve as connected emitters.

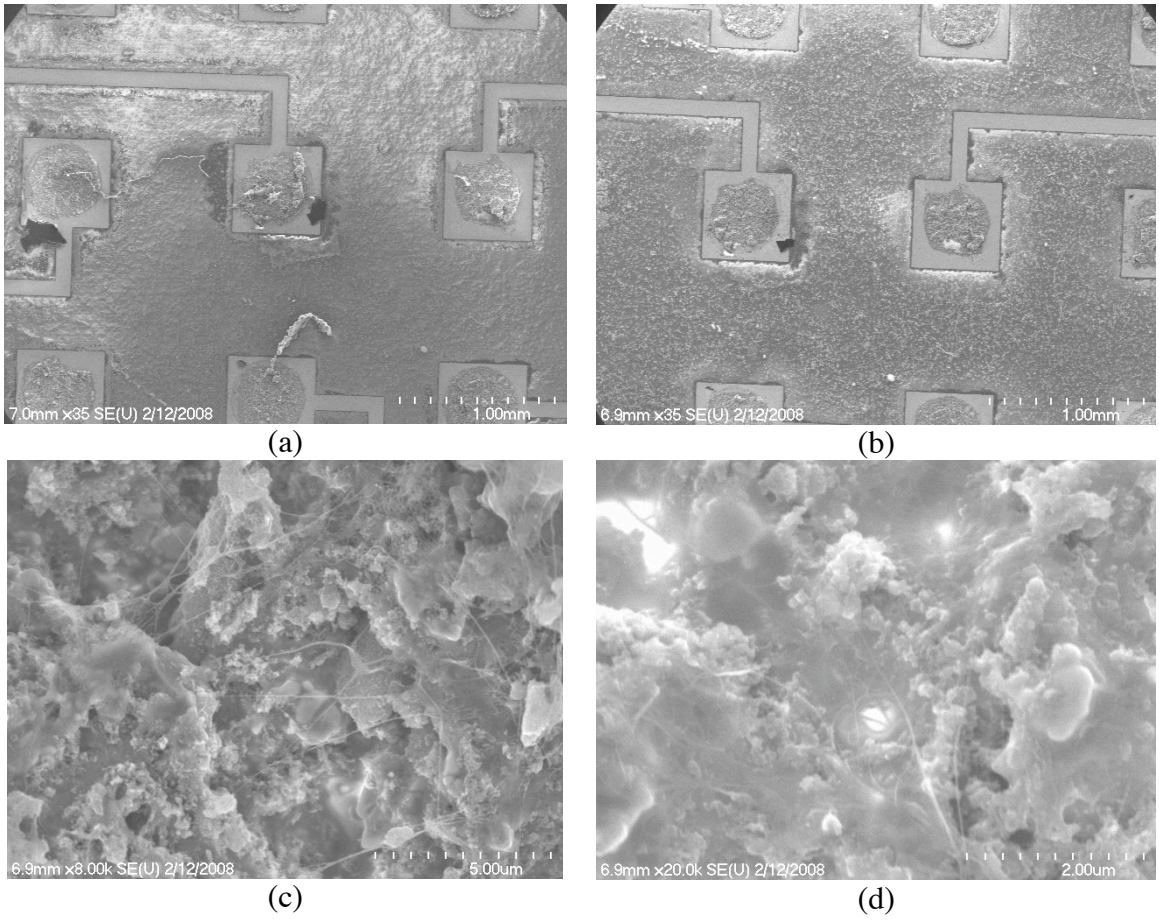

Figure 4.9: SEM images of the silicon wafer based CNT cathode. (a) Pre-taping image of a portion of the 5x5 cathode array. (b) Post taping image of the same location shows removal of debris from the chip surface and from individual cathodes. (c) and (d) Pre and post-taping images of the cathode morphology (different locations). CNTs are present in both images intermingled with the glass particles. The CNTs and debris in general is nominally thinned in the second image.

4.2.5 Field emission test of multi-pixel cathode

Prior to placing the multi-pixel cathode into the irradiator the cathode was tested to confirm its functionality. This included testing the field emission properties of the new cathode by measuring its I-V curve, evaluating its field emission uniformity by testing its

illumination of a phosphor screen, and demonstrating individual pixel control by observing the illumination of predetermined pixels.

The cathode was installed into the multi-pixel cathode holder pictured in Figure 4.10, and in place of a gate electrode a phosphor coated ITO glass substrate was placed parallel to the cathode array to serve as an anode, with 200 um glass spacers separating the two. For the field emission test and the uniformity test all the pixels were shorted together by connecting their contact pads to one another.

This assembly was placed into a field emission test vacuum chamber, and connections were made to the cathode lead and the anode via high voltage feedthroughs. The system was pumped to ~10^{-6} Torr. The tests were performed in diode mode.

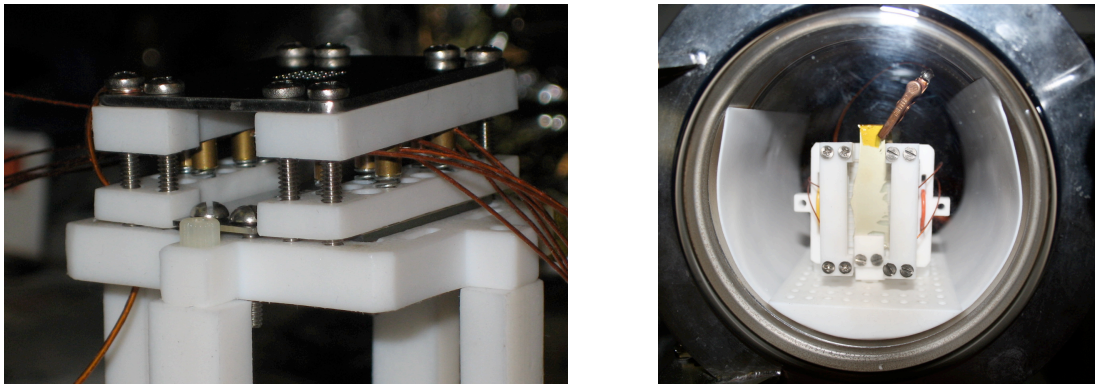

(a) (b)

Figure 4.10: (a) The multi-pixel cathode assembly: the cathode is sandwiched between the Teflon base plate and the individual connection components. Kapton coated wires provide connection to several leads in this image. (b) The multi-pixel cathode field emission test set-up: for the field emission test a phosphor coated ITO glass anode was used and is seen in the center.

For the field emission I-V testing of the cathode an automated test procedure was used to measure the current output. The cathode array was connected to ground through a 200 kOhm resistor as well as a current meter. The anode was connected to a high voltage pulse generator. Both the pulse generator and the current meter were operated via a Labview interface to automate the measurement procedure. From the starting voltage three 3 ms

pulses at a 1 Hz pulse frequency were applied to the anode. 3 ms was the minimum necessary read time to get an accurate data point read, and three pulses were used to get an average. The voltage was ramped by 50 V to a predetermined maximum voltage.

Data was obtained for both the silicon based cathode as well as the cathode array on glass. In the case of the silicon based cathode a current of 2.5 mA was obtained from all 25 cathodes, providing an average current of 0.1 mA per 500 um diameter pixel, corresponding to a current density of 0.05 A/cm^2.

For the cathode array on the glass substrate the same process was carried out. The results, as displayed in Figure 4.11, were similar to those of the silicon substrate. For all 25 cathodes a current of 2.0 mA was obtained at ~1200 V. This yielded an average current per pixel of 0.08 mA and a current density of 0.04 A/cm^2.

The current levels obtained for these multi-pixel cathodes, are somewhat comparable to other data recently reported by our group. While these levels could perhaps be a little higher they were nonetheless adequate for cell irradiation, which we have found to require relatively low current. This low current requirement is corroborated in Table 1.1.

However to achieve a higher current further development and testing could be performed on the cathode. The use of the phosphor screen as the anode may have limited the measurement of the cathode current. The phosphor screen sometimes exhibited unwanted characteristics such as charging and arcing, visible by light emission outside of the pattern of the cathodes. Charge accumulation on the cathode and/or anode may have been one source of these problems. Changing the anode to a metal rather than a phosphor screen anode would help in the future for a measurement of higher current.

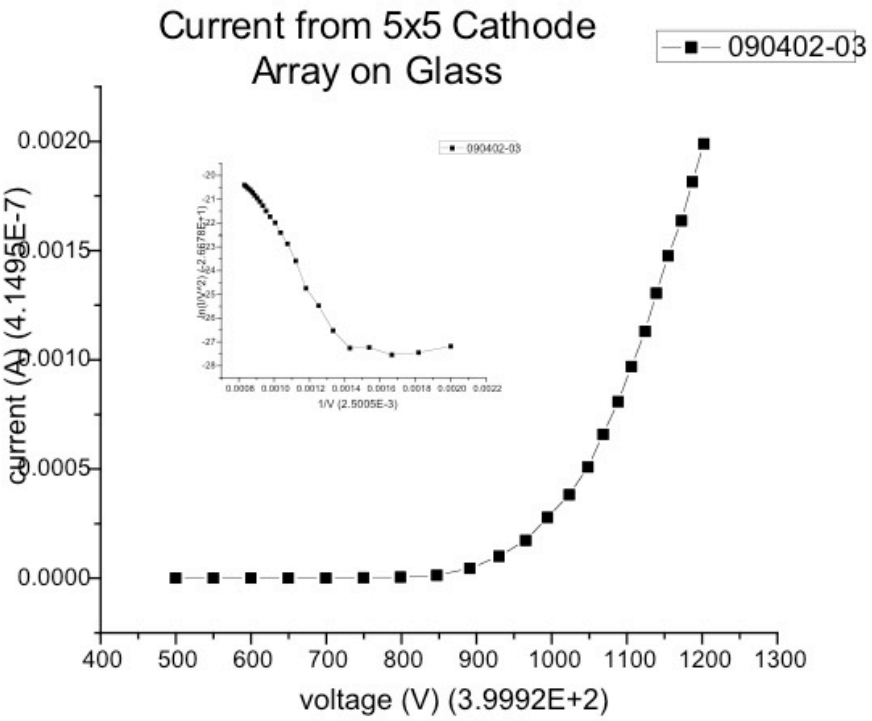

Figure 4.11: Field emission measurement data from multi-pixel cathode on glass, showing a peak measured current of ~2.0 mA at ~1200V. The inset graph shows the Fowler-Nordheim plot, demonstrating relatively good field emission at the higher voltages.

In addition to gathering the field emission I-V data images of the emission pattern, as seen on the phosphor screen, were taken to evaluate uniformity and individual control. For the first test, which was contiguous with the I-V test, the cathodes were shorted together, but different voltage pulse parameters were applied. The relatively long pulses, 3 ms +, used for the I-V measurement were not appropriate for this type of evaluation as they were more likely to cause charging on the phosphor screen. Therefore shorter pulses were utilized.

The image in Figure 4.12(a) was obtained from a phosphor screen pulsed at 50 us at 1000 Hz, an effective duty cycle of 5% at a voltage of 1000V. The reduced pulse duration provided for a more uniform phosphor screen image, as each pulse was shorter, resulting in less charge accumulation. The image was also somewhat dimmer as a result of degradation in the phosphor; nonetheless the image shows 25 functioning pixels of relative uniformity.

The circular pixels show some tendency to emit near their edges more than their centers, and it appears that certain spots around the diameter emit more strongly than others. There also appears to be one hot spot outside of the cathode locations, but the cause of this was unknown.

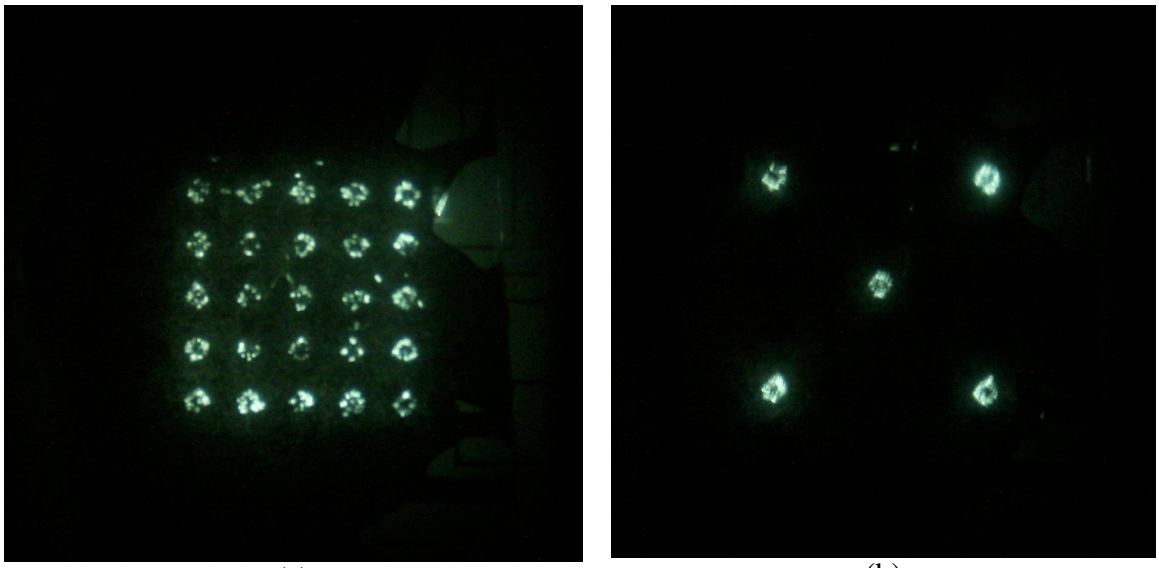

(a) (b)

Figure 4.12: Phosphor screen image of multi-pixel cathode with (a) all 25 pixels connected and (b) the corner and center pixels connected. The images demonstrate relative field emission uniformity and individual control of the pixels.

The image in Figure 4.12(b) was obtained by selectively connecting the corner and center pixels in the 5x5 matrix. Electrical parameters were similar to those for the 25 pixel image. The image demonstrates the individual control capability of the cathode chip at the test voltages. The pixels are relatively uniform and do not seem to be demonstrating any crosstalk.

4.3 Irradiation using CNT Cathodes

While much fabrication work has been completed for both the single and multi-pixel cathodes the ultimate goal of course is to evaluate their effectiveness and capabilities for

irradiation. Two methods were variously used for assessment: irradiation of radiochromic film and the irradiation of different kinds of cells.

The radiochromic film used was a conducting form of Gafchromic film HD 810. The film consists of a thin radiosensitive layer (~1 um) applied to a polyester backing. The film is sensitive to a broad spectrum of radiation, but for electron irradiation the radiosensitive layer must be placed in contact with the nitride window. Irradiated areas of the transparent film change to a deep blue, whose peak absorbance is around 670 nm. To determine the dose the film is scanned on a commercial scanner. The red portion of the RGB scan is used to extract the numerical densities of the exposed area and the unirradiated background. An optical density(OD) can then be determined which is correlated to dose (Figure 4.13).

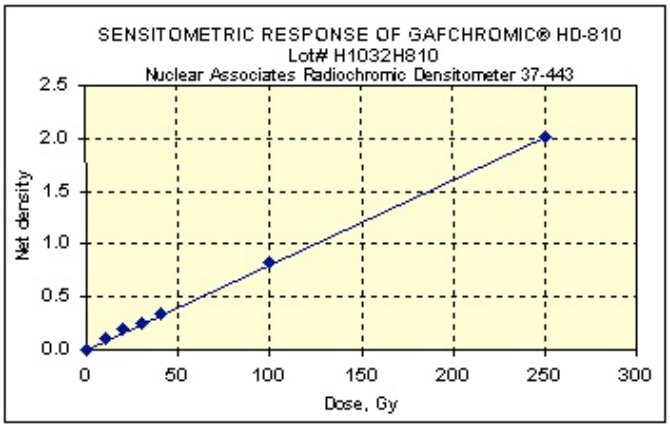

Figure 4.13: Graph of optical density vs. Absorbed Dose for GAFChromic HD-810 film. The film response has high linearity.

The following equation was used to convert optical density to dose:

$$\text{Dose (Gy)} = (125)[-\log(OD_{exposed}/OD_{background})] \qquad (4\text{-}1)$$

For the cell samples fluorescence microscopy was used to evaluate the radiation damage. A wide variety of fluorescent molecular probes are available for the detection and visualization of various kinds of cellular activity or transformation. For our experiments cells were fixed and stained following irradiation to visualize electron bombardment-induced

DNA Double Strand Breaks (DSB). A commonly used fluorescent polyclonal antibody was used to detect foci of the phosphorylated histone g-H2AX, which attaches to regions of DSBs. The g-H2AX antibody fluoresces green when attached to these regions. This provides a reliable confirmation of DSBs and radiation damage. It was also possible to use positive and negative control samples. The positive samples were irradiated in a Cesium irradiator to similar doses as used in the electron irradiation experiments. Negative control samples were allowed to experience a similar environment to the irradiated samples.

4.3.1 Irradiation using Single Pixel Cathode

The single pixel cathode system was the first phase in the project and represented the first data obtained using the CNT irradiator. For all of our irradiations, the field emission cathode has been operated in the pulse mode. The pulse width, frequency, and count can be varied via the pulse generator, with pulse widths of 10us to 1ms at 100 Hz being typical. The beam energy was typically fixed at 30kV. The system was used for film as well as cellular irradiation.

4.3.1.1 Film Irradiation and Calibration

The GAFchromic film was used to calibrate the system using both the silicon nitride membrane window as well as the laser drilled aperture window. Initially silicon nitride windows with dimensions of 18 and 10 um on a side were used for testing. For the 18 um window a single 1 ms pulse at a beam current of 2 uA was used, delivering a dose of 8.0 ± 0.3 Gy. After scanning a beam diameter of 45 ± 6 um FWHM was obtained (Figure 4.14).

This beam diameter as compared to the window size can be attributed to several factors. The first is the lack of beam collimation given the pyramidal geometry of the

anisotropically etched Si. This allows electrons to pass through the window from a much wider angular range than a higher aspect ratio collimator. The 54.7º angle at which the (111) plane meets the wafer surface translates into a 35.3º angle between the collimator walls and the beam axis. Additionally the square shape of the window means that the window diagonal is actually √2 larger than the window width, and in the corners the angle off the axis is 45º. The second factor is the intrinsic scattering experienced by the electrons traveling through the window, any intervening Mylar film and possibly through a narrow, and undesired, air gap between the window and the radiochromic film. Nevertheless this lack of collimation was motivation for improvement in the collimator.

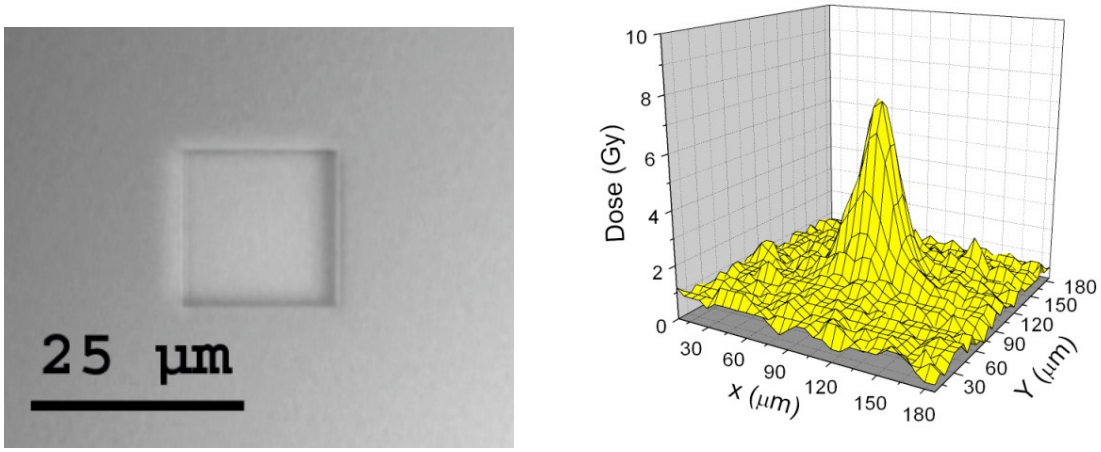

(a) (b)

Figure 4.14: (a) 18 x 18 um silicon nitride window. (b) 3D dose plot from irradiation showing an 8 ± 0.3 Gy irradiation with a 45 ± 6 um FWHM.

To attempt to reduce the beam size further the 5 um laser drilled aperture/Mylar film cap described earlier was installed. The radiochromic film was placed over the window and exposed in multiple locations. The irradiated spots of the film were scanned to determine the dosage. The matrix of values from the scan was converted into a representative 3D sample exposure plot as depicted in Fig 4.15(a) showing the dose distribution determined from the

scan of the film. A 2D plot through the center is shown in Figure 4.15(b). In this case the peak exposure is 12.1 ± 0.3 Gy with a FWHM of 23 ± 2 um.

Again given the use of the 5 um diameter window size, as compared with the 10+ um window, the FWHM measurement of 23 ± 2 um was somewhat higher than expected. The beam size can be attributed to electron beam divergence and scattering in several locations. The moderate 10:1 aspect ratio of the laser drilled collimator, scattering in the Mylar layer, and the potential for thin air gaps between the layers of Mylar and radiochromic film all contribute to the beam size observed.

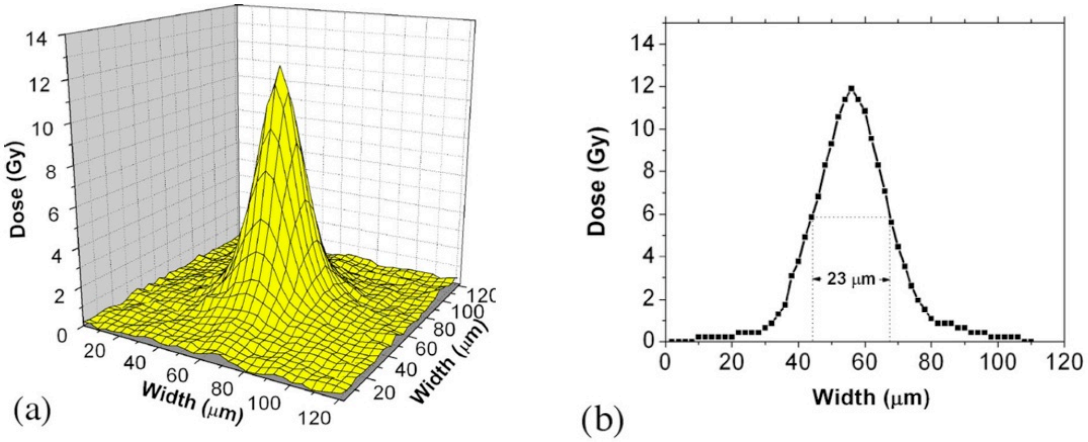

Figure 4.15: 3D dose plot converted from scanned film data of irradiation spot via 5 um laser drilled aperture. The dose is 12.1 ± 0.3 Gy and the FWHM is 23 ± 2 um.

While reasonable irradiations were achieved via the single beam system it was also desirable to estimate the efficiency of the beam current. Approximately 30% of the beam current was lost to the gate and focusing elements prior to reaching the anode surface, the electron window chip[10, 11]. The transmission rate through the nitride membrane itself was determined to be at least 70% for 30 keV electron beam[12, 13]. The Mylar Petri dish bottom, which the electron beam must pass through before cell irradiation, also moderately attenuates the electron beam intensity[14]. However the overall transmission rate of the system is largely determined by the size of the electron beam window/collimator chosen for a

specific cell irradiation experiment. Conventional clinical radiotherapy and thus cell irradiation research uses an average dose rate ranging from 1 to 300 Gy per hour. We were able to produce a dose rate ranging from 1 to 100 Gy per second in the prototype system demonstrating that the field emission achieved is more than adequate for this application. Furthermore the beam current can be correlated to the dose delivered for any given cathode and electron window/collimator set up.

As mentioned earlier a 3.5um x 6.5um window was also constructed (Fig 4.16(a)). While this window did not yield any significantly better data than the 5um aperture we were able to use it to test the repeatability of the dose from pulse to pulse. In this test the film was exposed by irradiating and shifting the film serially over five separate locations (Figure 4.16(b)). Each location received 25 1ms pulses at standard beam conditions. The film was scanned for analysis. The average dose for each spot was 17.9 Gy with a dose per pulse of 0.7 Gy. The standard deviation was 0.9 Gy, approximately 5% of total dose. The spots are on the order of 25-35 um, which is not quite as small as our previous best data from the laser drilled aperture.

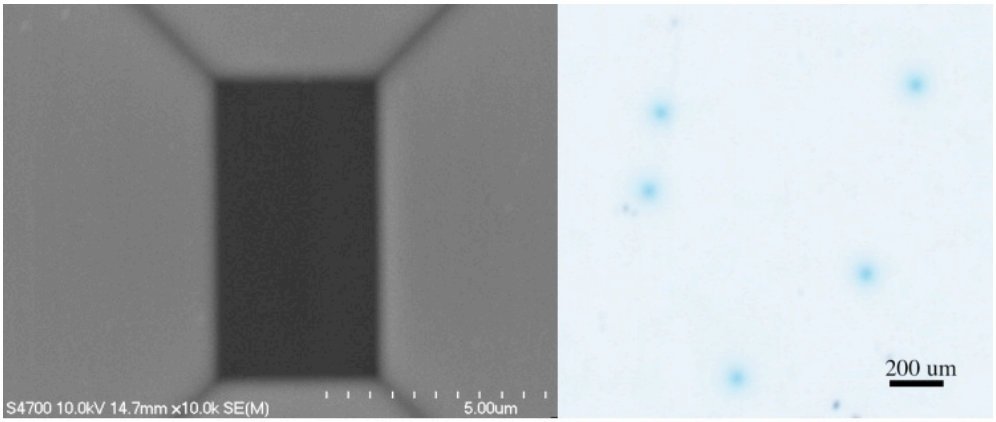

(a) (b)

Fig. 4.16: (a) SEM image of the 3.5um x 6.5 um silicon nitride window from etched side of the wafer. (b) Scanned image of exposed Gafchromic film with five separate irradiation spots of average dose of 17.9 Gy, dose per pulse of 0.7 Gy, and standard deviation of 5%.

4.3.1.2 Cellular Irradiation

In addition to the film data obtained cell irradiation was performed to demonstrate the systems functionality. For the cell irradiation experiment a custom-made cell dish and dish translation stage were used.

To test the dish and translation assembly a dry run was performed using the radiochromic film. A piece of the film was attached to the bottom of the cell dish with adhesive to simulate the process of irradiating various regions of a cell dish and to perform multiple irradiations in close proximity to one another. In this experiment the 18 x 18 um silicon nitride electron window was used.

The cell dish was placed in the translation stage and the micrometers were manipulated so that the film could be irradiated in an "L" shaped pattern as seen in Fig. 4.17. The cell dish and attached film was translated over the window in 100 um increments between each irradiation exposure. Each exposure was a single millisecond pulse delivered with a cathode current of 2 uA and a beam energy of 30 kV. In this case an average maximum dose of 8.3 ± 0.9 Gy was achieved, demonstrating relative uniformity from exposure to exposure. Sources of variance in the uniformity were as before, scattering, potential gaps between the window and film, lack of resolution in the film scanning process, and broadening as a result of the non-vertical sidewalls of the silicon collimator.

The results of the dry run being satisfactory the same technique was applied to a sample of rat fibroblast cells. First a cell dish was constructed consisting of a stainless steel ring and Mylar film. A 1.5 um thick sheet of Mylar was glued to the flat-bottomed ring using a biologically compatible epoxy (EP21LV from Master Bond Inc.). Rat fibroblast cells were

plated and grown into multiple sterile dishes in a monolayer for irradiation over several days. The x-y translation stage was included to move the cell dish in relationship to the microbeam.

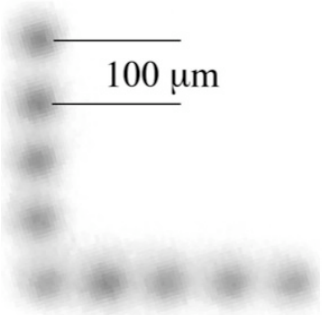

Figure 4.17: Successive exposures in radiochromic film were made following 100 um movement via the simple translation stage to form the above L-shape. An average dose of 8.3 +/- 0.9 Gy was obtained for 1 ms pulses at 2 uA beam current and a 30 kV acceleration voltage.

To carry out the cell irradiation and identify the location a special procedure was utilized. First, using our first phase microscope (Figure 3.4), the electron window was located and centered in the viewing field using a compact X-Y-Z translation stage. Unlike the radiochromic film the irradiation pattern in the cells would not be as easily observed. It was necessary to note the position and return to it after treatment of the cells with the antibody probe. For this reason an etched coverslip was placed in a square frame mounted to the top of the Mylar bottom dish. The dish was placed over the silicon nitride exit window. After locating a region of confluent cells the position in the dish was noted by focusing on to the coverslip which was etched with a numbered and lettered x-y matrix. This position and the final position after translation were recorded for simplified location of the irradiated area

Prior to and following the cell irradiation time, about 20 minutes, the cells were maintained at standard incubation temperatures. A representative area of the SCI irradiated cell dish is depicted in Fig 4.18(a) and (b) at 4x and 20x, showing the density of the plated cells. With the cell dish positioned over the electron exit window the irradiator was used to deliver an approximately 20 Gy equivalent of pulsed electron irradiation. Using the

micrometers the dishes were shifted 250 um between irradiation doses in order to form an easily recognizable “L” shape. Because the film had shown such close overlap at a 100 um spacing a larger spacing was used to ensure separation between locations.

Following irradiation the cells were fixed and stained to visualize electron bombardment-induced DNA Double Strand Breaks (DSB). The polyclonal antibody was used to detect foci of the phosphorylated histone g-H2AX, attached to regions of DSBs. The cells were then examined with fluorescence microscopy as shown in Figure 4.18(c). The areas fluorescing in green indicate the presence of foci of DSBs in the same location and in the same “L”-shaped pattern as expected. A positive control cell dish, uniformly irradiated in a Cesium irradiator, is depicted in Figure 4.18(d) showing uniform presence of foci across

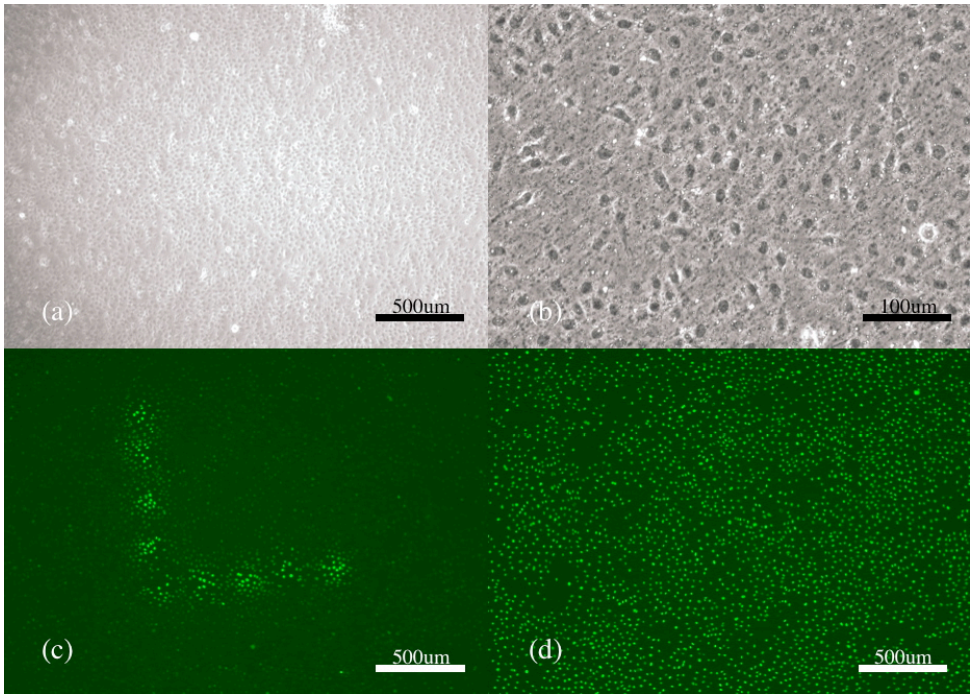

Figure 4.18: (a) (b) Images of plated cells in Mylar bottom Petri dish at 4x and 20x respectively, showing the cell density of the irradiation samples. (c) Fluorescent image of plated cell sample following irradiation and fixing and staining procedure to mark DNA double strand breaks via the g-H2AX, polyclonal fluorescent antibody. The separation between irradiation sites is approximately 250um. (d) Fluorescent image of a representative region of a positive control cell dish, uniformly irradiated in a Cesium irradiator at 21 Gy, showing uniform presence of foci. Reproduced from reference[15]

the dish. The combined data show that the amount of current generated by the CNT field emission is sufficient to quickly irradiate the cells to produce a clearly measurable response.

The data also affirm the decision to expand the separation between irradiation locations from 100 um with the film to 250 um with the cells. The film measurements show that 100 um spots are readily distinguishable, but had 100 um spacings been used for the cells it is likely that the "L" shape would have had a more continuous appearance rather than that of lines of separate spots. It is not clear whether this larger spot seen in the cells in comparison with the film is the result of a bystander effect or that the low dose reaching those areas produces a more intense response.

Another comparison between the film and the cell images is that the film has a clearly defined and calibrated means by which to read off the dose following irradiation, as seen in Figure 4.13 and Equation 4-1. At least for the specific elements from this project no such means exists for the cells. Therefore we lack a means of converting observed fluorescence into dose received. In this case 20 Gy equivalents were used for ease of locating the dots. This was performed in some measure subsequently but also represents a possibility for future work and calibration of the system. The comparison between the film and cell irradiation data is an area for future investigation which can help to shed light on the scattering, dosimetry, and fluorescence interrelationships.

4.3.1.3 Large Window Experiments and Results

In addition to testing our smallest windows the single pixel system has also been tested using a much larger window on both film and cells. For some experiments it may be desirable to expose a larger group of cells to study their collective reaction or variable reactions to uniform irradiative stress. A large square silicon nitride window was made with

dimensions of ~250um on a side (Fig. 4.19(a)). As described above film was irradiated to obtain dosimetric data for the window (Fig 4.19(b)). Instead of 25 1ms pulses a single 500us pulse was used. The average dose delivered was calculated to be 24.5 ± 3.7 Gy. The large window resulted in a much higher dose delivery rate likely owing to its much larger area and lack of collimation. Additionally the large window was used to irradiate human colorectal cancer cells. The cells were stained with gamma H2AX to identify foci of DNA double strand breaks (Fig. 4.19(c)), demonstrating uniform large area irradiation using the single pixel system.

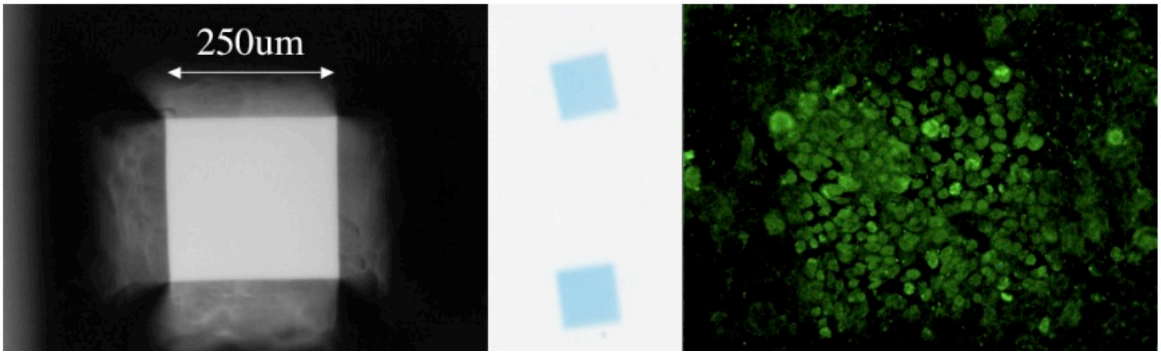

(a) (b) (c)

Fig. 4.19: (a) Optical microscope image of the large nitride window, ~250um on each side. (b) Scanned image of exposed Gafchromic film showing two sample irradiation spots using the large nitride window. (c) Fluorescent microscope image of gamma-H2AX stained human colorectal cancer cells following electron irradiation; the shape of the square is visible and slightly tilted rotated toward the left.

For this same irradiation the cells were stained not only with the γ-H2AX stain, but also stains for other cell structures. The stain DAPI highlights the cell nuclei while Texas Red highlights the cell wall. Figure 4.20 depicts a composite and the separate images of the stains over the same area depicted in 4.19(c). This capability will allow for more precise cell irradiations in the future.

When irradiating with the large window it can be assured that the whole area is receiving a uniform dose. Many cells in this case receive essentially the same dose. In the

case of the small window the objective is to irradiate potentially a single cell and at most only a few cells are irradiated are the maximum dose. Additionally while the dose profile from the large window looks essentially like a plateau with an ~250um top, the dose profile

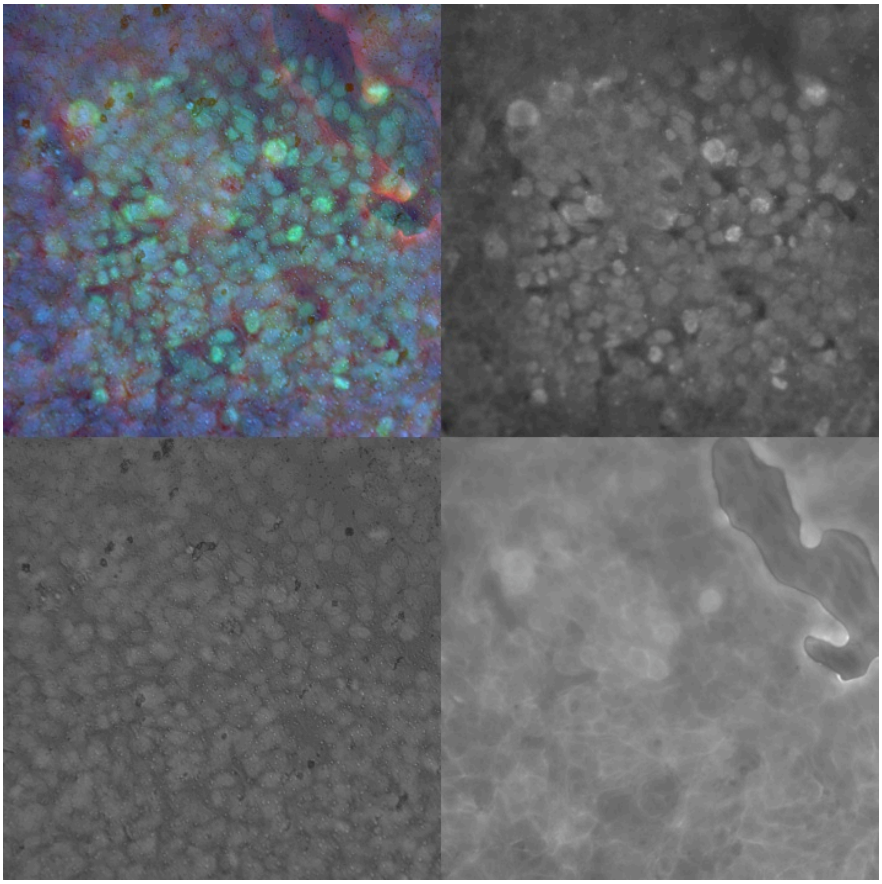

Figure 4.20: The above fluorescent microscope images were obtained following irradiation and staining of human colorectal cancer cells. The cells were irradiated through a nitride window approximately 250um x 250um in area. The cells were stained and imaged with gamma-H2AX (upper right), Texas Red (lower right), and DAPI (lower left). The composite image (upper left) is formed after tinting and combining the grayscale images. DAPI, in blue, highlights the cell nuclei, Texas Red highlights the cell wall, with gamme-H2AX highlighting the foci of DNA DSBs.

from the small window looks more like a Gaussian function with an ~30um FWHM. With its large irradiation area the large window is then a better means of investigating comparative dose response using the gamma-H2AX marker as it results in a larger sample size of cells seeing the dose.

Another dish of the same cells was irradiated in five locations with the 250um window while the irradiation spots were spaced by approximately 2mm. After using radiochromic film to calibrate the electron dose output the spots were irradiated with doses of 11.5, 23, 46, 92, and 184 Gy respectively (Figure 4.21). The cells were then fixed and stained. Images of the cells were obtained with a microscope showing a gradual increase in the number of foci and overall fluorescence as the dose increased. This was done to investigate any upper limit in the dose to fluorescence response. Although the data have not yet been quantitatively analyzed, some degree of saturation seems apparent in the upper exposure range of 92 Gy and higher.

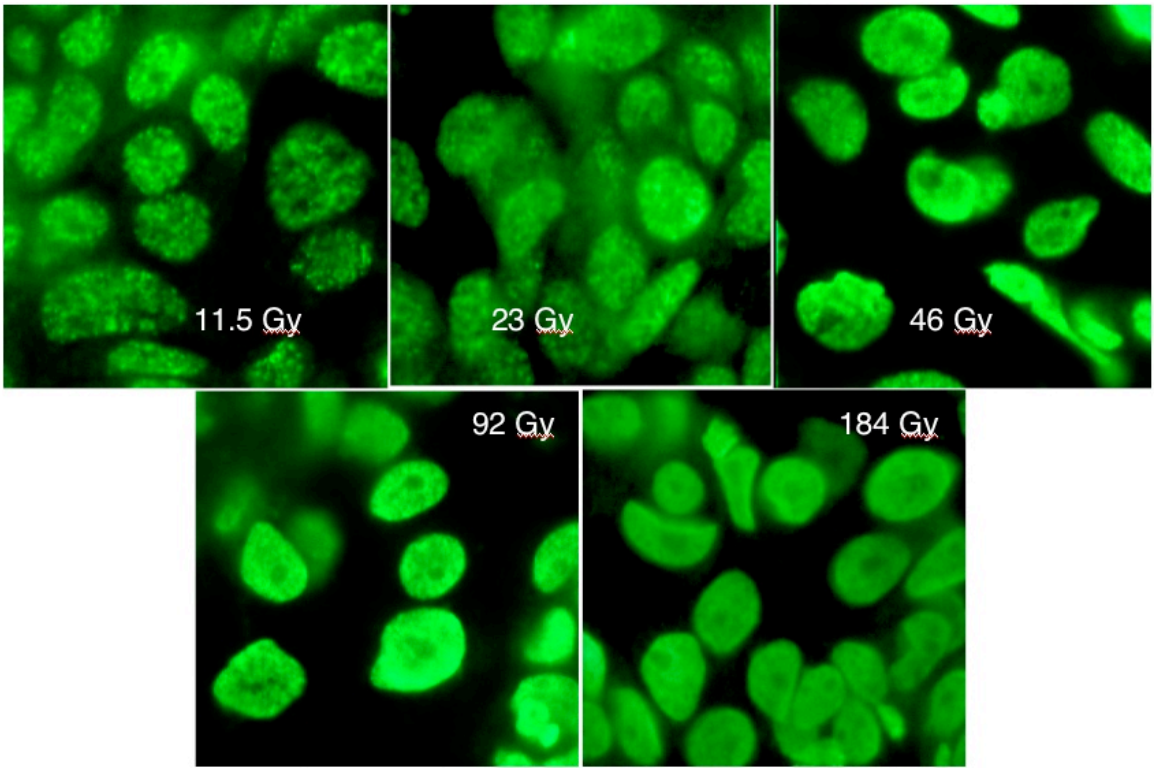

Figure 4.21: Regions of cells irradiated via the 250 um window at a dose range from 11.5 Gy to 184 Gy. A correlation between dose and the number of foci was observed.

Observation of this dose dependence points to the capability of using the nanotube based cell irradiator and particular the multi-pixel system to test various doses within a single

population of cells in a dish, all experiencing similar conditions with the exception of the dose received.

Finally a comparison irradiation was performed by placing an additional dish of cells in a radiobiology laboratory Cesium irradiator. The entire dish received 10 Gy of radiation. This provided an experimental control for the electron irradiated cells. Comparing the image from the control dish with the area of the electron irradiated dish receiving 11.5 Gy in Figure 4.22, we can see that the two show a similar density of DNA double strand break foci, further validating this irradiation method.

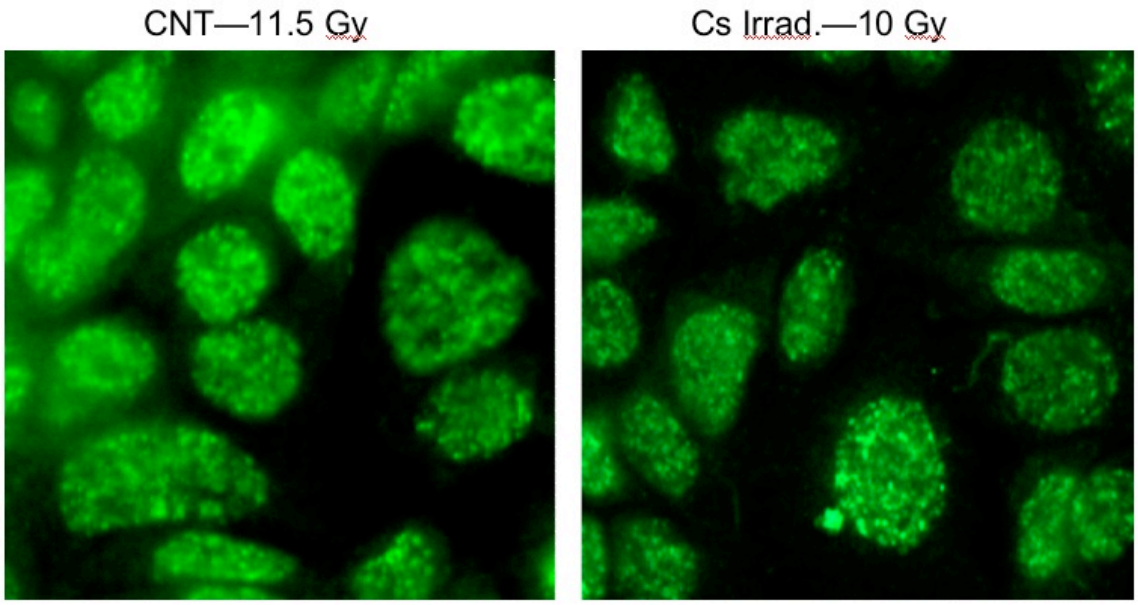

Figure 4.22: Comparison irradiation between the CNT based irradiator (11.5 Gy) and a Cs irradiator (10 Gy), showing relatively similar levels of foci.

4.3.2 Single-pixel irradiation capabilities and dosimetry analysis

We have obtained a broad data set related to the as-developed single pixel CNT based irradiator. The minimum irradiation spot at FWHM obtained in these experiments has been 23 ± 3 um, somewhat greater than desirable for single cell irradiation experiments. This was obtained using a 5 um laser-drilled aperture with a 10:1 aspect ratio.

While the overall objective of this project has been to develop a multi-pixel cell irradiator it has nonetheless been of interest to develop a single beam system of small diameter that would be capable of irradiating single cells. Early in the project an ambitious beam size of 3 um was targeted to enable the irradiation of subcellular components while stating that a 20 um beam would allow for whole cell irradiation. Both would be achieved via beam collimation. Also desirable was a high irradiation dose rate which would allow for the deposition of doses in the 1-10 Gy range in 1 s or better. To evaluate these goals, I will discuss the beam profiles obtained and the various simulation results others have achieved. I will also discuss possible improvements to our system for cell irradiation.

In considering the beam profile we see that the small aperture/narrow beam experiments performed have resulted in relatively sharp peaks of dose as seen in Figures 4.14 and 4.15. The beam profiles take on a generally Gaussian shape, suggesting a normal distribution as a result of a series of random processes. There is value in this comparison as the electron energy dissipation process takes place through a random series of collisions events.

Nevertheless viewing the beam profiles as a perfect bell curve is somewhat inadequate. First each window, and therefore the electron beam, has a finite width. This produces some level of deviation from a true bell curve as it is a departure from a point source or pencil beam. This may cause the actual profile to appear more like a plateau. Second, edge effects in the profile should also be taken into consideration as there may be a lack of beam equivalency at the center and the edges of the window. Because of the shape of the collimator sidewalls, whether a silicon nitride window or a laser-drilled aperture is used the profile edge may see a more drastic drop-off in dose than a normal distribution as the

presence of the edge may hinder some of the possible electron exit paths as compared with the center.

As mentioned above the beam apertures used are of more than finite width. In the case of the film exposure via the 250 um window (Figure 4.19(c)) the conversion of this image into a profile has a plateau or mesa shape as compared with the small apertures. Additional data was collected from a 50 um window showing an irradiation profile from an intermediate size. Here the peak is broader than that seen for the smaller apertures but without a full plateau. This suggests that in the range from small apertures (5-20 um) to the larger apertures (250+ um) a broadening of the peak will occur so that a continuum between a near Gaussian distribution and a plateau or mesa shaped profile exists.

It is also important to address the width of the peak as related to the window dimension. From the data presented it can be seen, at 30 kV acceleration voltages, that the peak is always wider than the electron aperture. There are a number of reasons for this, several of which have been mentioned earlier: scattering through the window, Mylar layers, and any air gaps present as well as scattering in the radiochromic film. Figure 1.20 graphically depicts some of this scattering in a water medium for multiple electron tracks. It appears that to a large degree the scattering that takes place, particularly closer to the beam entry while its initial energy is higher, is forward scattering at small angles, which tends to extend the irradiation in depth as well as laterally. In this data set the entering beam is a pencil beam and sees moderate scattering. In the case of an actual collimator the beam as it emerges from the window is neither a pencil beam nor is it necessarily perfectly orthogonal to the aperture and film. Both of these factors contribute in such a way as to increase the width of the measured beam.

Other factors affecting the evaluation of the beam profile are related to our measurement techniques. The radio-sensitive emulsion layer of film used to measure beam profiles lacks complete uniformity as can be visualized under an optical microscope. Some non-uniformity, perhaps ± 1 um, is present, perhaps as a result of variations in the radiochromic component's distribution in the emulsion. Also the measurement of the film introduces further, though moderate, error with our newer scanner providing a feature resolution as small as 2 um, 12800 dpi, depending on the setting selected. Despite the excellent scanner resolution these factors introduce as much as a few microns of an additional uncertainty in the beam profile. In the case of the narrower peaks, such as the 23 um FWHM, even at 2 um resolution most of the curve is defined by only 25 points, a relatively rough sketch of the profile.

Of course the ultimate question that arises from this data is to ask what the minimum attainable size of an irradiation spot is. For an initial estimate of this system's capabilities based on our best experimental data we can start with the 23 um beam diameter from a 5 um circular aperture, with the assumption that the FWHM represents the beam diameter, and extrapolate for various aperture sizes. In the ideal case of a pencil beam of electrons our beam diameter might be reduced to as little as 18 um, which represents the intrinsic broadening. Assuming a more reasonable but challenging reduction of the collimator aperture to 1-2 um extrapolation reduces the beam diameter to perhaps 20 um. These proposed values would also require the relatively high aspect ratio collimation, 10:1 or greater, demonstrated in the laser drilled aperture. Given the possibility of the laser drilled apertures in conjunction with other possible collimation techniques to be discussed in Chapter 5 it should be possible to form these high aspect ratio collimators and reach a 20 um

diameter at 30 keV acceleration voltages. The potential downside of this process would be the reduction in the electron fluence through the reduced aperture. A consequent reduction in dose rate would probably result, although the large dose rate range available could be used to compensate.

In addition to this initial estimate from our system, the simulation data referred to in Chapter 1 also provide a means of estimating the smallest possible beam diameter. Unfortunately the simulation data is displayed according to different parameters in each case, making a side-by-side comparison difficult. Nevertheless starting with the KIRAMS data in Figure 1.19(a) at 30 keV with a 5 um collimator at a depth of 5 um into the irradiation sample we see that the deposited dose is ~ 5% of the peak dose at a beam width of ~20 um. Given the 5 um collimator and using the 5% measurement this data suggests an intrinsic broadening of 15 um. From the Texas A&M data in Figure 1.19(b) at 25 keV we have already seen that a radius of 8.65 um envelops 90% of the absorbed dose. This would suggest an intrinsic broadening of twice that value or 17.3 um. Again because of the two different data sets exact quantities are not being compared; the radius at which a 95% reduction in the peak dose is calculated does not necessarily equate to the radius at which 90% of the absorbed dose is contained. Finally in the data set generated at UNC and depicted in Figure 1.20 the entering beam is a pencil beam yet is spread to diameters of 2, 12, and 30 um for energies of 10, 30 and 60 keV. Choosing the 30keV data from this more limited evaluation the intrinsic broadening is estimated to be 12 um.

To summarize the simulation data we have at 30 keV, 25 keV, and 30 keV intrinsic broadening values of 15 um, 17.3 um, and 12 um respectively. A simple average of the simulation data yields ~14.7 um with our best experimental data set providing an intrinsic

broadening of 18 um. Given these data a conservative estimate of the minimum beam diameter achievable for a beam energy in the neighborhood of 30 keV, with a very small collimator of 2 um, would be approximately 17 ± 2 um. This estimate meets one of our initial goals, that of irradiating single whole cells in the range of 20 um. Also this value is only 1 um lower than the intrinsic broadening value of 18 um for our best data. These data suggest that achieving a 3 um electron beam at 30 keV for subcellular irradiation might not be feasible. But this estimate would also seem to suggest that an electron beam system operated at these energies would still have some single cell irradiation limitations. Hitting a 10 um diameter single cell without irradiating a neighboring cell partially or with a reduced dose might be impossible in the case of highly confluent cells. A more thorough analysis of the existing simulations along with further use of the existing simulation code could provide more detailed answers relevant to our current system setup.

A few other possibilities could be explored to attempt to narrow this irradiation diameter perhaps into the range of 15 um or lower and to more successfully achieve single cell irradiation. The first possibility is that of managing the cell samples by using larger cells or by making them less confluent and therefore less likely to see a neighbor irradiated.

The second means is that of utilizing alternative high voltages. As discussed in Chapter 1 these simulation data also show interesting effects at both higher and lower acceleration voltages. Figure 1.19(a) would suggest that at acceleration voltages of 70, 80, or more keV small angle forward scattering is stronger than at even 50 keV with the beam width in the first 5-10 um of depth showing reduced broadening. Using this means an even higher voltage might be one means of reducing this beam size down a few microns. Potential disadvantages of this method would be the difficulty of measuring dose deposited into a

thicker layer of the radiochromic film than is sensitized. Also the possibility exists that the higher energy beam would irradiate the media above the cells in a manor that would disrupt experimental conditions, perhaps generating unwanted radicals. For our system this method would not yet be testable given higher required voltages. The other possibility is that of lowering the beam acceleration voltage. Comparing the Figure 1.20 data for 10 and 30 keV one could assume that an intermediate voltage might produce less scattering and a smaller beam diameter. Lowering the voltage to 20-22 keV would still assure some electron fluence through the window structure and could potentially reduce the beam diameter down to the range of a 10 um single cell. Unfortunately this would probably come with the potential cost of reducing the dose rate. This was observed in a few experiments in which the standard 30 keV voltage was not obtainable as a result of arcing. Operating the system in the lower range increased irradiation time over 10x while maintaining the same beam current. Increasing beam current might allow this to be overcome, but beam efficiency is reduced as a greater portion of the beam energy is absorbed in the window and Mylar layers. Also given the potential for variation in these layers and occasional air gaps the lower voltage path is less preferable and more prone to dose variation.

The final means by which this beam diameter might be reduced would be the utilization of the techniques described above along with a variety of adjustments to the irradiator and its collimator along with techniques to increase the aspect ratio. One means of decreasing this value would be to reduce the thickness of the nitride layer or the Mylar layer(s) used. Given the very small windows being utilized a thinner nitride of perhaps 150 nm could be structurally sound. Also the 3 um Mylar layer previously utilized could be replaced with a 1 to 1.5 um layer. Thinning these layers would reduce scattering prior to

arriving at the irradiation sample. Lastly improvements in the collimation of the electron beam could provide some reduction in beam diameter. A more intense study of the beam shape arriving at the window could bring about adjustments to improve the beam focusing, and a higher aspect ratio collimator could also provide a greater degree of collimation. A process for fabricating a higher aspect ratio collimator will be discussed in Chapter 5.

The other initial goal of our project was to achieve a useful irradiation dose rate. In Chapter 1 we discussed that one of the limitations of X-ray based systems was the increased irradiation times given their low dose rate. An irradiator system with useful irradiation doses that can be achieved in 1 s or fractions of a second will provide a strong advantage over X-ray irradiation. In the preceding data we have shown a variety of irradiation rates depending on the window used. For the small window, 3.5 um x 6.5 um, a single 1 ms pulse was able to produce an average irradiation of 0.7 Gy, and for the large window, 250 um, a single 0.5 ms pulse delivered 24.5 Gy. Given these data and the capabilities of easily varying the pulse count, pulse width, and beam current, a dose rate range of 1 cGy to 100 Gy per second is readily achievable, with some dependence on the window size.

4.3.3 Irradiation using Multi-pixel Cathode

While we have been able to obtain a variety of results with the single pixel irradiator, the multi-pixel cathode introduces a number of new challenges. The first of those is the successful independent connection of up to 25 pixels when fully realized. The next is being able to obtain irradiation from all 25 pixels. And the final most challenging goal is the ability to have unique cathode pixel to window correspondence; that is that when a particular pixel is turned on that the window in the matrix to which is corresponds is the predominant recipient of its electron dose.

4.3.3.1 Multi-pixel Assembly

To start we constructed a multi-pixel cathode assembly (Figure 4.23) comprising, much, like the single pixel cathode, a cathode holder, gate electrode with spacers, a focusing electrode, and a means of aligning the cathode array to the window array.

The major difference from the single pixel system was the greater complexity of the pixel interconnect components, which allowed for connection of 25 separate pixels. These components provided the bridge between the Kapton connection wire and the contact pads located on the outside of the multi-pixel cathode. Kapton wires, which connected to a multi-pixel feedthrough, were fed, at the cathode assembly, into holes drilled in the side of small brass cylinders and attached with orthogonal set screws. The cylinders nested in an array in the same pattern as the outer cathode contact pads. A second component with corresponding through holes was positioned underneath the cylinder holder; small diameter springs were

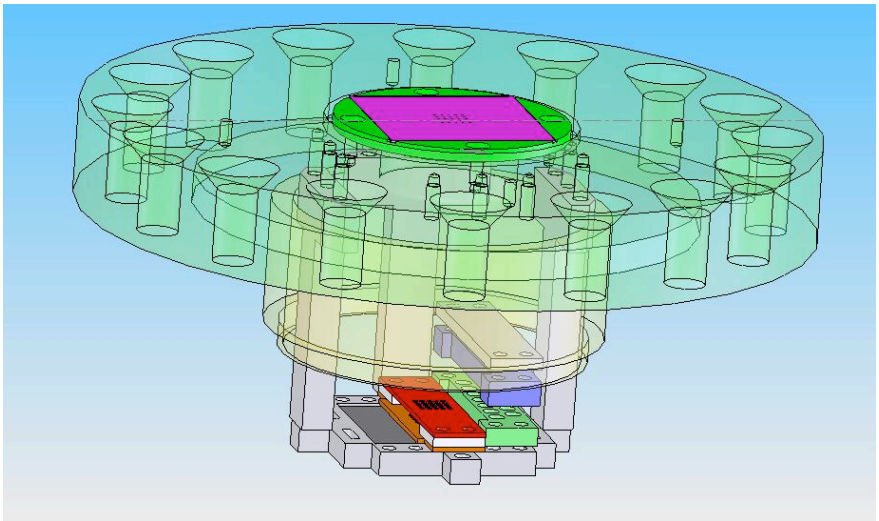

Figure 4.23: Solidworks rendering of multi-pixel cathode assembly as connected to the anode flange and irradiation window array. The cathode is placed in a recessed area (dark gray) near the bottom of the assembly. A gate electrode (orange), focusing electrode (red) sit centrally while interconnect elements, (green, blue) are positioned on outside. Teflon legs attach and provide alignment to the anode flange (top, green), and the 5x5 array window (purple) is attached to the anode via the mini-flange (opaque green).

placed into the through holes making contact between the on-chip contact pads and the brass cylinders. While something like a set package with wire bonding would have been an attractive alternative the cathodes would potentially have large voltages between them which would require excellent insulation. Therefore the package as described functioned as the current best design.

We were able to address the first issue by testing the CNT cathode array and the etched silicon nitride window together. In this case the full 5x5 CNT cathode array was connected together so as to simultaneously see emission from all of the pixels. This cathode was placed in the cathode assembly, but a single connection to all the cathodes was utilized as opposed to the mutli-pin feedthrough. The cathodes were turned on and were used to irradiate radiochromic film through the window array. The scanned film shows evidence of irradiation at each pixel (Figure 4.24). The center pixel was analyzed for dosimetry, and it

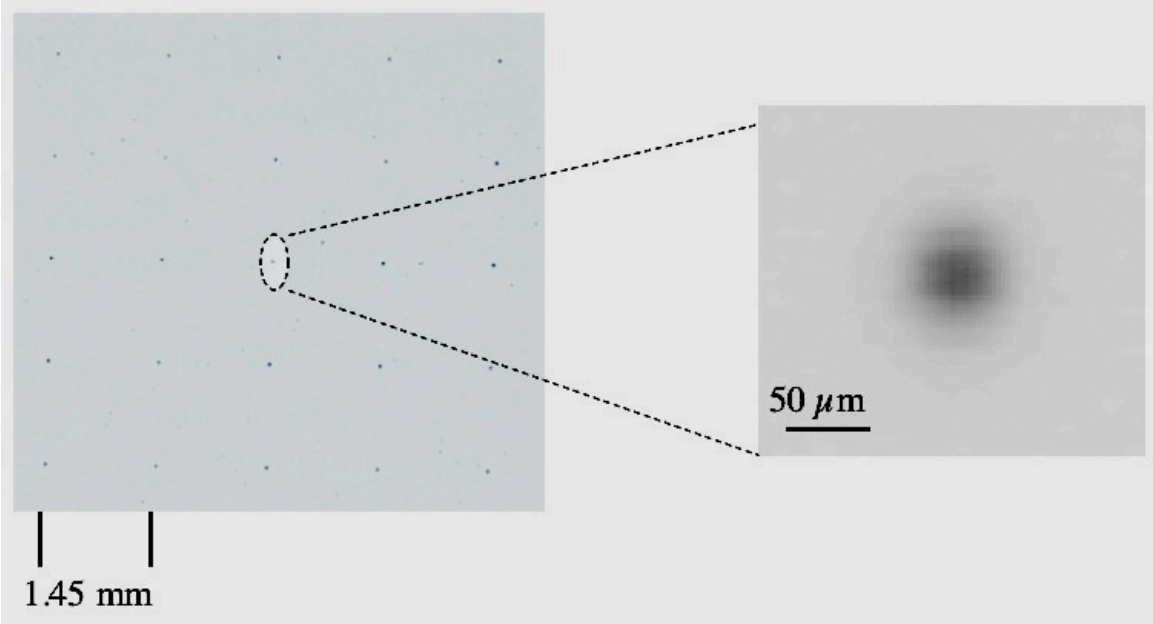

Figure 4.24: Film scan of multi-pixel irradiation via full interconnection of cathode array. The 5x5 window array was used as well. Dosimetry on the central pixel shows a FWHM of 40 ± 4 um and a maximum dose of 29.1 ± 0.4 Gy.

was found to have a FWHM of 40 ± 4 um with a maximum exposure of 29.1 ± 0.4 Gy. Given the known non-uniformity in the window array, ranging from 9um to 13 um windows, as well as the unknown uniformity of the cathode array the scanned image shows reasonable uniformity.

4.3.3.2 Proposed Control Electronics

To address the lack of uniformity and the need to independently control the multi-pixel system a circuit board and Labview interface are being developed. The circuit board provides a layout of variable resistors and high voltage MOSFETs to address these issues. Variable resistors are placed in series with each pixel and provide tunability for the cathode current. Eventually the system will have a fixed gate voltage, and adding resistors to each pixel allows them all to be tuned to the proper output without having to change the gate voltage. The high voltage MOSFETs are also in series with the resistors and are connected via their gates to the 5 V inputs from the multi-pin output of the computer based lab view

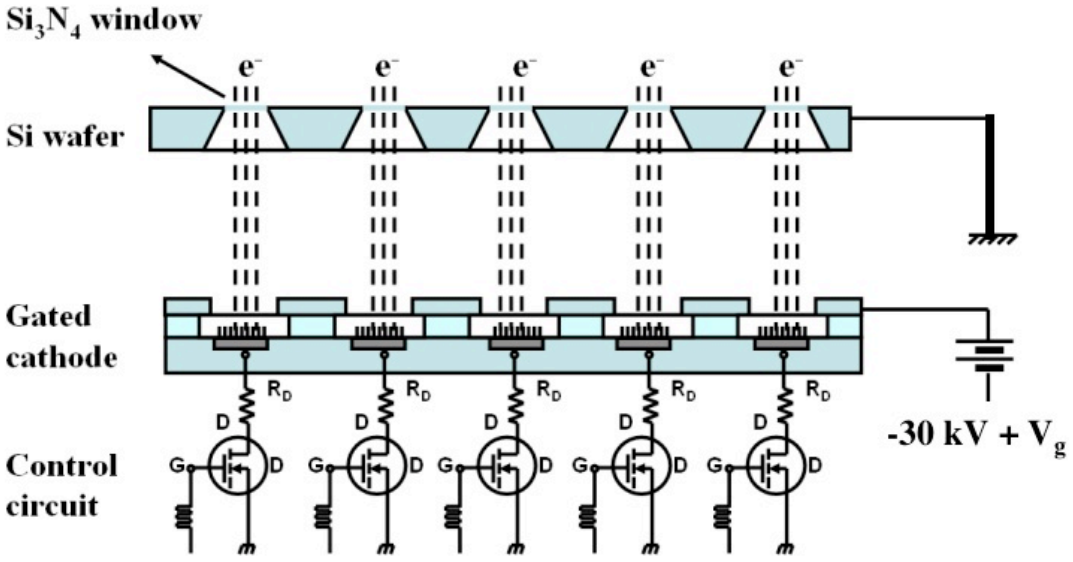

Figure 4.25: Proposed example control circuit for multi-pixel cathode. The MOSFETs will be addressed by a 5 V Labview interface.

interface. The lab view interface will allow for further control of each pixel. Pulse width, count, and frequency can be adjusted to produce a wide variety of irradiation variations for a single pixel or all twenty-five. Work is still ongoing in developing the interface. In particular, problems with the high voltage need to be corrected that may cause overheating and damage to some of the components.

4.3.3.3 Irradiation Using Individual Pixel Control

To test the individual pixel control capability of our system the glass substrate based multi-pixel cathode (Figure 4.6(b)) was installed along with a new multi-pixel window. In this case several pixels were wired individually as seen in Figure 4.9 (a) with effort made to avoid any intermittent contact to other pixels. The vacuum chamber was fitted with a high voltage multi-pin feedthrough flange (Figure 4.26), and the Kapton lead wires for these contacts connected via the feedthrough. With all of the wires connected on the inside it was possible to connect select wires on the outside to address particular pixels on the inside.

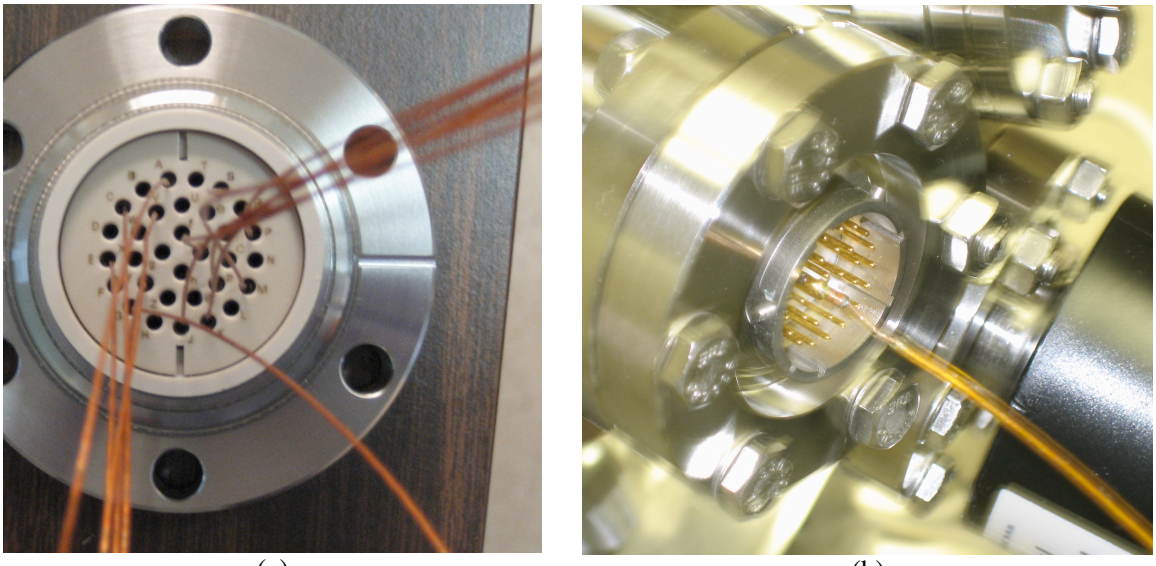

(a) (b)

Figure 4.26: Views of the multi-pin feedthrough wiring scheme. (a) Multiple wires are connected on the vacuum side of the flange. (b) A single wire connected to a grounded multimeter on the outside in order to activate the pixel.

Pixels were connected individually and in a few cases several pixels were connected simultaneously. Unfortunately it was not possible under this arrangement to tell which pixels were emitting and which were not when several were connected. Also different responses to the gate voltage made this mode of operation less useful. In one case some damage was done to some of the pixels because of arcing or some form. Therefore more caution was taken in gathering the data.

For the multi-pixel window a modification was made in order to enhance the window collimation performance. As discussed earlier a single KOH etched window provides relatively low screening as compared with a higher aspect ratio vertical collimator. To address this difficulty two KOH etched windows were stacked together as an initial, simple, and cost effective means of forming a higher aspect ratio collimator. In this case two 5x5 window arrays were used. The top silicon array was left in its native state with the 9-13 um nitride membranes intact, with the exception of a few which had been broken. The bottom wafer was etched in the RIE to remove the nitride layer, and then etched for a few minutes in KOH to expand the size of the aperture. These ranged from 10-30 um. The two wafers were stacked and glued with vacuum epoxy wafer backside to wafer backside as shown in figure 4.27 to form a new high aspect ratio collimator with a thickness of 800 um and an aspect ratio of perhaps 25:1. Because of the broken windows a piece of Mylar was attached to the top surface and the entire piece was glued with the epoxy to a multi-pixel mini-flange having 1 mm holes for each window. The chips were aligned by placing their edges evenly with one another, the edge positions having been determined by the KOH trench etching technique described earlier. Alignment was checked via an approximately orthogonal visible light source. Light was seen to shine through all 25 apertures in the array.

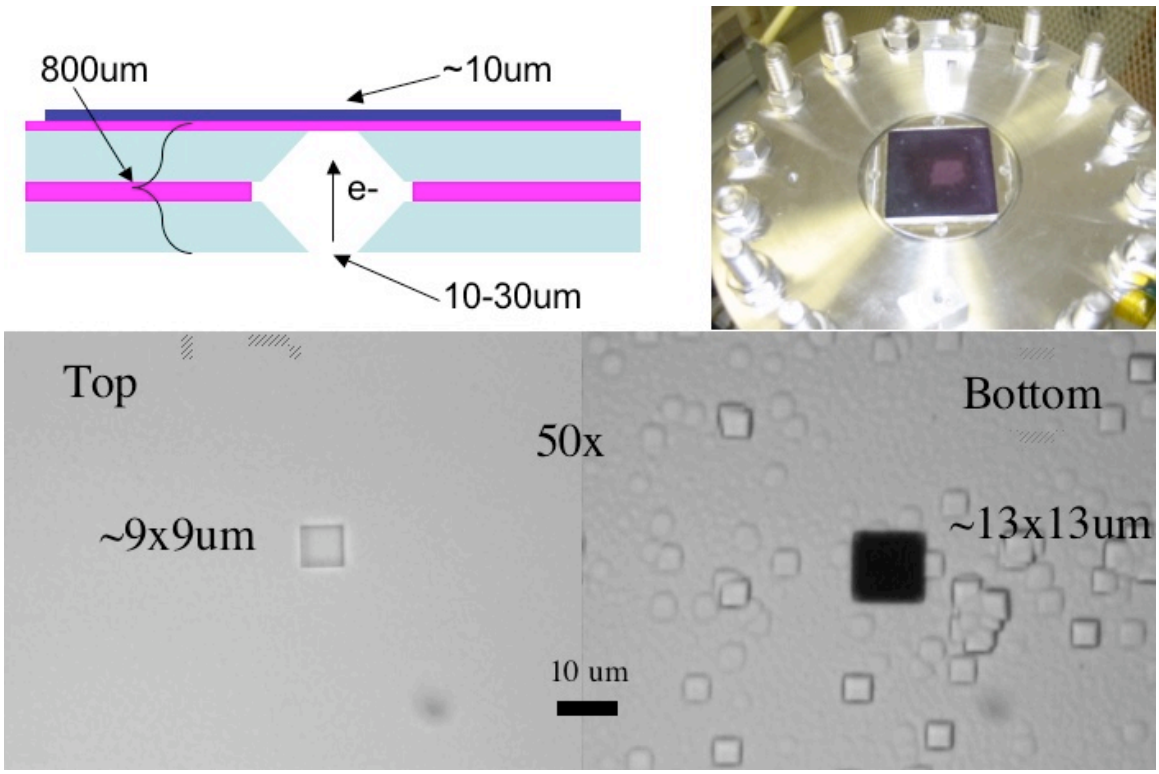

Figure 4.27: The double-stacked 5x5 array electron window collimator: schematic, picture, and optical microscope images of sample windows from the top and bottom chips.

For the film irradiation test of individual pixel control it was found that high voltages above ~20 kV would induce arcing. In addition to the 20 kV acceleration voltage a pixel current of 5 uA was used at 10% duty cycle. Because of the low acceleration voltage much longer irradiation times were necessary to obtain recognizable irradiation spots on the film. Exposure times on the order of 5-10 minutes were used. This length of time is clearly outside of the reasonable length for irradiations, but in future work it should be possible to increase the voltage and reduce the time significantly. The 20 kV acceleration potential reduced the electron transmission and dose delivery. Also higher aspect ratio collimation reduces the number of electrons passing through. These issues are related to the arcing and electrical challenges that have occurred, and should be addressable so as to increase current and voltage and thereby reduce the irradiation time.

For simplicity of evaluation corner pixels were used to irradiate the film. Using the parameters listed above cathode pixels in the upper right and lower right of the chip layout as seen in Figure 4.6 were activated and used for irradiation. Both cathode pixels showed the strongest irradiation over the window corresponding to their pixel location, but some irradiation took place around neighboring windows (Figure 4.28). The specific values obtained for the detectable irradiation spots are marked on the figure. For both data sets the

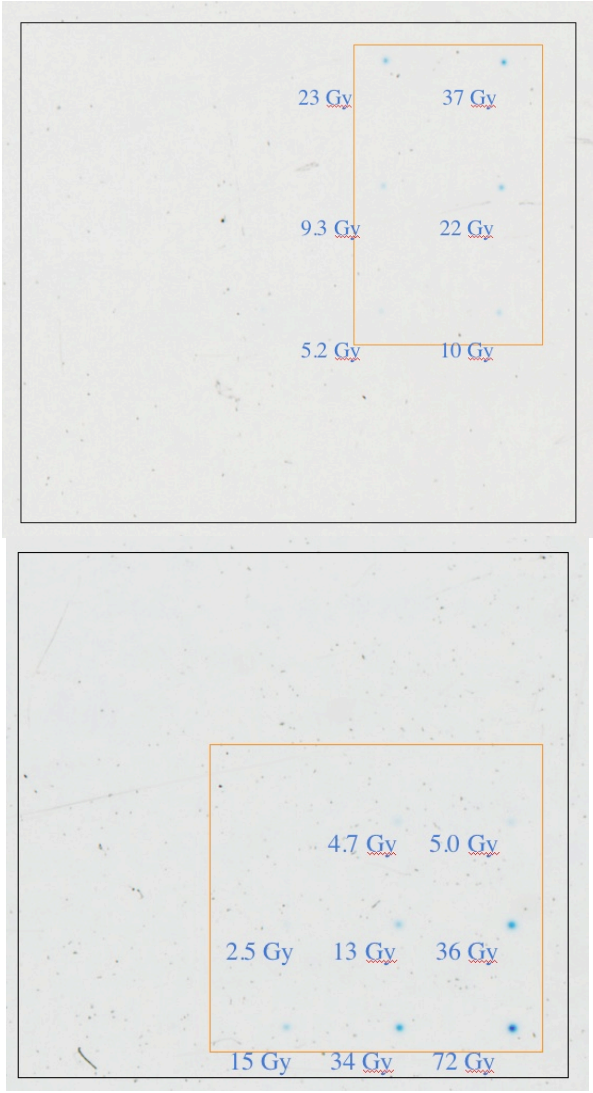

Figure 4.28: (Top) Irradiation pattern from upper right pixel. (Bottom) Irradiation pattern from lower right pixel. The black box shows the approximate location of the 5x5 array. The orange box shows the recognizable irradiation spots. The spots have been analyzed and the peak dose at each detectable spot is listed.

dose obtained at nearest neighbors was about half that received at the corner window. For the next nearest neighbor the dose was around one quarter of the corner dose. The values of one half and one quarter are not particularly meaningful other than the fact that they generally demonstrate that some form or forms of crosstalk are taking place in the multi-pixel system, such as beam crosstalk (a collimation challenge) and/or electrical crosstalk (an insulation and breakdown challenge). For biological experiments crosstalk of this magnitude is undesirable and unacceptable as it does not represent true individual pixel control. In some cases crosstalk of a few percent might be acceptable, but ultimately this requires some form of alleviation.

4.3.4 Multi-pixel irradiation evaluation and analysis

In developing the multi-pixel irradiator an implicit goal was to avoid this type of severe crosstalk. Future work on the multi-pixel system will need to address some of these problems. I will attempt to address several of the potential problems and fixes for the multi-pixel system here.

One source of error observed was that the gate mesh was bowing when the gate metal support was attached to the cathode; this took place because the attachment created a compressive stress on the part. This caused the gate to be in much closer proximity (perhaps 50-100 um closer) than the standard 200 um gap distance over a portion of the cathode array. This may have contributed to the pixel non-uniformity in terms of turn on voltage and current uniformity. With some portions of the gate significantly closer than others the cathodes in that area would show lower voltage turn on and emit more current than the other cathodes. After it was discovered this was addressed by spot welding the tungsten gate mesh to the

stainless steel gate piece. This allowed the bowing effect to be mitigated when the gate support was attached. After reinstalling the repaired gate structure the next set of results did not demonstrate greater uniformity; nevertheless this was an appropriate fix for a potential problem.

Given that the gate bowing was not the observed problem it was necessary to consider other possible errors, such as the possibility of surface breakdown in between the pixels. It is thought that this might be one reason behind the lack of cathode pixel to window pixel correspondence. To address this issue would require the introduction of some changes in the cathode chip fabrication. The process is not as clean as could be reproduced in other environments, and better processes would also prevent the presence of any contaminating metals on the surface which may contribute to a lower surface breakdown potential. The surface of the chip in between pixels might also be made rougher by an etching or plasma treatment process. This would increase surface area and increase the linear resistance in the case of a surface breakdown. Another means of addressing the potential for other pixels emitting would be to tie any floating pixels into the gate voltage. This would prevent them from emitting, but it would also introduce high voltage directly onto the chip whereas previously the high voltage is only indirectly applied to the chip.

Despite these attempts at fixing the system the challenges of arcing and crosstalk remain the main issues. These are both significant challenges and are mostly a result of scaling up the system from a single beam to a multiple beam. I will discuss them here along with various methods of addressing them further.

Crosstalk in the multi-beam system can be separated into two types, electrical and beam crosstalk. Beam crosstalk assumes that when a particular pixel is activated, via

grounding its connection to the floating ground of the system, that electrons are then predominantly if not entirely emitted from that pixel. Ideally the beam would then entirely or predominantly irradiate the film or target over its corresponding window. There are several possible reasons this may not take place. Given the inter-cathode spacing of ~1.5 mm center to center, with cathodes widths of 500 um, and a cathode to anode distance of approximately 5 cm, the aspect ratio of the collimator, depending on the type of window used, needs to be 50:1 or better to completely eliminate beam cross talk. This assumes linear trajectories of the electrons from the cathode, which will not necessarily be the case as the beams pass through the gate and focusing electrodes. Component alignment also may generate some beam crosstalk. In recent observations of the system it was observed that there might be some degree of misalignment between the cathode array and anode array given less than ideal fitting of some of the machined components. In various proportions lack of planarity, x-y shift, and rotation about the z-axis contribute to the misalignment between the two arrays. This could leave the arrays misaligned by a common directional shift or could leave certain cathodes well aligned and others way off because of a rotation. A single cathode-single window arrangement shows much higher tolerance for these misalignments, but with multiple cathodes spaced 1.5 mm apart these misalignments may combine and produce some various measures of crosstalk. The particular configuration of the cathode assembly makes the evaluation of crosstalk challenging as we lacked a clear manner of measuring the misalignment. Also given the timing of the work and the fixed relationship between various system components a complete redesign of the cathode assembly was not possible. The development of a new cathode assembly using better alignment techniques along with other

system components would be an important part of any future work for a multi-pixel system. In particular a chamber with a slightly larger inner diameter would be a strong advantage.

Electrical crosstalk also interferes with the desired activation of a particular pixel and irradiation at the corresponding window. Fabrication of the glass chip was completed in an effort to overcome this challenge. Nevertheless there are several places where electrical breakdown may occur in the multi-pixel cathode assembly.

For our system isolating cathode pixels from one another has several possible points of breakdown. In our current system an individual pixel can be wired in several different modes of connectivity. Some subset of the pixels is wired to the multi-pin feedthrough. One or more of those pixels may actually be grounded so as to permit normal current flow under an applied gate voltage. And in some experiments some have been left disconnected or "floating". Given this scenario the possible points of electrical breakdown seem to be where Kapton coated connection wires from the multi-pin feedthrough contact one another, some of the short distances between conducting structures of the cathode connection assembly, and some of the short distances on the cathode chip itself between adjacent cathodes or cathode lines. Chip level contamination or defects at various ones of these surfaces or possible points of breakdown could contribute to some of the breakdown. But additionally some of the general conditions of system operation could contribute to breakdown potential. In some cases the contact lines on the chip are as close as 500um, with voltage differences of 1500V present in the vicinity along with the possibility of static charges developing between adjacent lines. These conditions may lead to unpredictable breakdown across the surface of the chip causing cathodes close by to a connected cathode to emit electrons. This could

account for some of the strong film irradiation seen beyond what might be seen as mere beam crosstalk from lack of collimation.

For the single beam system, beam and electrical crosstalk are mostly non-factors. Arcing between other components though may still be a factor as it may produce an abundance of electrons leading to a higher than desired irradiation of the film.

Increasing the number of cathodes and windows brings about a new set of challenges including the importance of maintaining electrical isolation in the connections and the avoidance of various kinds of cross talk.

While in one sense it would seem multiple beams should be merely a matter of scaling up the design it is in fact much more challenging. With a single electron source and a single exit window there is very little cross talk that can take place, only perhaps from a stray electron source created through an arcing event.

Another problem that can present a challenge when working with high voltage systems such as the cell irradiator is electrical arcing. This differs from the electrical breakdown which takes place with lower voltages over short gap distances. Arcing in this case is associated with the high voltages applied to the system for electron acceleration and are only observed during their use. Several steps have been taken to attempt to mitigate the arcing problems observed. Some of these have been better cleaning steps, such as electropolishing and solvent cleans of parts going into the vacuum system. Unfortunately the work area lacks the high degree of cleanliness needed as does the chamber, meaning some dirt and dust will always infiltrate the system. One of the main sources of arcing seems to be our limited chamber size and the effect that has on the proximity of various electrical components. When some of these components are grounded and others at high potential

difference the inner chamber diameter of 2.4 inches results in very close proximity of the cathode assembly, particularly the focusing electrode, to the grounded irradiation flange.

One of the first steps taken to alleviate this was to fabricate and place a Teflon collar between the cathode assembly and the irradiator flange wall. This provided some level of reduction in the arcing frequency and an increase in the applied voltage at which arcing occurred, up from about 12 kV to 15 kV difference.

The attachment legs of the cathode assembly were also lengthened to address this. An additional 2 cm provided more separation between the focusing plate and the flange. Finally the edges of the focusing plate were rounded, polished, and cleaned. This provided a much higher level of protection against arcing as we are now able to operate the multi-pixel set up at 20 kV with only occasional arcing problems.

Some of these issues as related to breakdown and electrical arcing are perhaps related to my relative inexperience about high voltage electronics or have been affected by design choices made near the beginning of the project. Although it has not always been possible to redesign the system to account for deleterious effects encountered a future generation of the system should be able to overcome some of these current limitations.

4.3.4.1 Future optimization of the multi-pixel irradiator design

Reviewing the discussion above there are several things that can be done to improve and optimize the multi-pixel irradiator. These include a number of component and system redesigns that would reduce arcing and some of the crosstalk due to misalignment. Additionally work and testing needs to be performed on the cathode along with a potential redesign to eliminate electrical crosstalk due to high voltage breakdown. Finally and most

importantly beam collimation can be improved to bring about the pixel to window correspondence desired and partially demonstrated by the data here. A cathode assembly redesign would also be wise to explore a reduction in the distance between the cathode and the anode, another type of collimator to eliminate beam crosstalk, or an increase in the pixel-to-pixel spacing. With some or all of these improvements highly independent irradiation beams should be possible for a similar system.

4.4 Summary

We have designed and constructed prototype single pixel and multi-pixel irradiators. Functioning electron windows and cathodes have been built. Irradiation of film and cells for the single pixel and film for the multi-pixel have been completed. The single pixel system shows good, repeatable, and long-term function, which is useful for cell irradiation. The multi-pixel system prototype's irradiation capability has been demonstrated and areas for improvement have been identified, such as better electrical function under high voltage, completion of independent control, and resolution of crosstalk issues. Potential solutions have been discussed, and some work towards them has been completed.

References

1. K. Williams and R. Muller, *Etch Rates for Micromachining Processing*. Journal of Microelectromechanical Systems, 1996. **5**(4): p. 256-269.

2. B.Y.U. ECEn Dept. Web Team. *Oxide/Nitride Color vs. Thickness Generator*. 2009 [cited; Available from: http://www.ee.byu.edu/cleanroom/color_chart.phtml.

3. W. Lang, *Silicon microstructuring technology*. Materials Science and Engineering: R: Reports, 1996. **17**: p. 1-55.

4. H. Seidel, et al., *Anisotropic Etching Of Crystalline Silicon in Alkaline Solution*. Journal of The Electrochemical Society, 1990. **137**(11): p. 3612-3626.

5. T. Muller, et al., *Defect Related Problems with the On-chip Integration of Sensors Into CMOS Devices. Proceedings of the Third International Symposium on Defects in Silicon*. 1999. Seattle, WA: Electrochemical Society.

6. A. Hein, et al., *The effects of thermal treatment on the anisotropic behavior of Cz- and Fz-silicon*. Sensors and Actuators A: Physical, 2000. **86**(1-2): p. 86-90.

7. B. Gao, et al., *Fabrication and electron field emission properties of carbon nanotube films by electrophoretic deposition*. Adv. Mater., 2001. **13**(23): p. 1770-1774.

8. S. J. Oh, et al., *Liquid-phase fabrication of patterned carbon nanotube field emission cathodes*. Appl. Phys. Lett., 2004. **84**: p. 3738-3740.

9. Microchem. *NANO SU-8: Negative Tone Photoresist Formulations 2-25*. [cited; Available from: http://www.microchem.com/products/pdf/SU8_2-25.pdf.

10. G.Z. Yue, et al., *Generation of continuous and pulsed diagnostic imaging x-ray radiation using a carbon-nanotube-based field-emission cathode*. Appl. Phys. Lett., 2002. **81**(2): p. 355.

11. Z. Liu, et al., *Carbon Nanotube Based Micro-Focus Field Emission X-ray Source for Micro-Computed Tomography*. Appl. Phys. Lett., 2006. **89**: p. 103111.

12. L. Hanlon, et al., *Electron window cathode ray tube applications*. J. Vac. Sci. Technol. B, 1985. **4**(No. 1): p. 305-309.

13. J. Wieser, et al., *Vacuum ultraviolet rare gas excimer light source*. Rev. Sci. Instrum., 1996. **68**(No. 3): p. 1360-1364.

14. J.H. Miller, et al., *Microdosimetry of Electron Microbeams*. Radiation Research, 2004. **162**: p. 474-479.

15. D. Bordelon, et al., *A nanotube based electron microbeam cellular irradiator for radiobiology research*. Rev. Sci. Instrum., 2008. **79**.

CHAPTER FIVE

RECENT PROGRESS, FUTURE DEVELOPMENTS, AND CONCLUSIONS

5.1 Summary of work completed and recent developments

The development of the UNC carbon nanotube based electron cell irradiator has truly been an interdisciplinary project. We have taken a nanomaterial which has been of great interest in the realm of the physical sciences and used it to address an existing area of need in radiobiology. The electron irradiator has demonstrated the capability of facilitating investigation into the radiation response of living cells. The project has been interdisciplinary in another sense in that it has involved the merging of a variety of systems and techniques in the physical sciences. The development of the system has required the assembly of a high vacuum system, the engineering of a high voltage platform, and the incorporation of microscopic viewing and positioning of cell samples on the irradiator. Additionally the preparation of custom assemblies and the use of microfabrication techniques to develop various components have required further integration of sometimes disparate areas of work.

And while these various methods and systems have been brought together with the purpose of forming a single and multi-pixel array of microbeams for cell irradiation, the work has also opened the doors to new areas of investigation, experimentation, or

improvement. We have already discussed irradiation experiments using apertures other than the small pixel microbeams, for instance irradiation through the 250 um window. While this does not constitute a microbeam technique it does represent an alternate form of cell irradiation.

Two areas of recent work that have focused on exploiting or improving the current system will see further evaluation in the future. In the first case we have designed and fabricated samples for potential improvements to the irradiator utilizing Deep Reactive Ion Etching (DRIE). In the second case we have begun investigating the possibility of using the as-developed cell irradiator for study of microbeam radiation therapy (MBT) at the cellular level.

5.2 Development of components via DRIE

It was previously discussed that several components for our system could be produced using a microfabrication technique known as DRIE. The gate electrode and electron window/collimators previously discussed as well as a modification of the double slit structure would all be candidates for this process. DRIE allows for very high aspect ratio etching of custom patterns into silicon substrates. A microfabrication process flow was developed to build a passive MEMS type structure, with many of the techniques used commonly in MEMS foundry processing, to apply this technique for our system.

For these devices the basic starting material was identical to that used for the fabrication of KOH etched pinhole collimators, 400 um thick, double side polished silicon wafers with a 300 nm LPCVD deposited low stress silicon nitride. The silicon nitride deposition process was completed by MEMSCAP Inc. in Research Triangle Park, NC.

5.2.1 Wafer Backside Processing via KOH etching

The first half of the process was very similar to that used in the fabrication of the silicon nitride membrane windows. The silicon nitride starting wafers were coated in Shipley 1813, exposed, developed, baked, and etched using the same parameters described in Chapter 4. The pattern created was also used to create a silicon nitride mask of the wafer for KOH etching. Different patterns were used from those shown in Chapter 4 to create different sized squares or rectangles to accommodate the designs to be etched via DRIE.

The wafers were also etched in KOH according to the same parameters as before. Previously the silicon was etched completely so as to reveal the silicon nitride membrane. For these components the silicon was partially etched through its thickness so as to leave some thickness of silicon remaining in which to form the DRIE etched structures. In the KOH etch the silicon was etched down to a depth of 240-250 um, leaving behind 150-160 um of silicon. Depths were determined as before, periodically, by using the fine focus micrometer on an optical microscope during the etch process.

5.2.2 Frontside Photolithography and Masking

After completion of the KOH etching the wafers were prepared for etching from the opposite side as seen in Figure 5.1. The DRIE would be used to form structures etched all the way through the remaining silicon layer. The silicon nitride layer used before for KOH etching is not resistant to the DRIE process therefore other materials were used for form an etch mask. Because the etch depth would be on the order of 150 um a relatively robust etch

mask was required. Two different types of etch masks were used, the first a chromium etch mask and the second a KMPR photoresist etch mask.

5.2.2.1 Chromium Etch Mask Process

For the fabrication of the silicon gate mesh as well as the silicon chip window/collimator a chromium etch mask was formed. The chromium etch mask was formed by DC magnetron sputter deposition using a Lesker PVD 75. Approximately 2000A of Cr was deposited from a 3 in target onto each substrate at a power of 300W at a rate of just under 2 A/s in ~20 min.

After removal from the sputter system the wafers were spin coated with ~1.5um Shipley 1813 positive photoresist, exposed via a dark field mask, and developed for 60 s in MF 319 developer. The photolithography step created a pattern by removing the photoresist in the shape of the holes to be etched in the DRIE. For each of these structures most of the wafer was covered in photoresist with only the cumulative area of the small holes left behind. Next the wafer was hard baked at 125 C for 60 s prior to chromium etching. Room-temperature CR-7 chromium etchant solution was used to etch the chromium layer. The wafers were etched for approximately 120 s total. The chrome mostly cleared after about 90 s, but additional overetch time was included to fully etch the chrome and possibly eliminate or undercut smaller defects in the features.

After etching the chrome through the photoresist layer the underlying silicon nitride layer was exposed. This was etched in the SAMCO RIE-1C according to the process described earlier; this allowed the silicon layer to be exposed directly to the DRIE process. Additionally the 1.5 um photoresist layer was left in place to provide additional protection during the DRIE process.

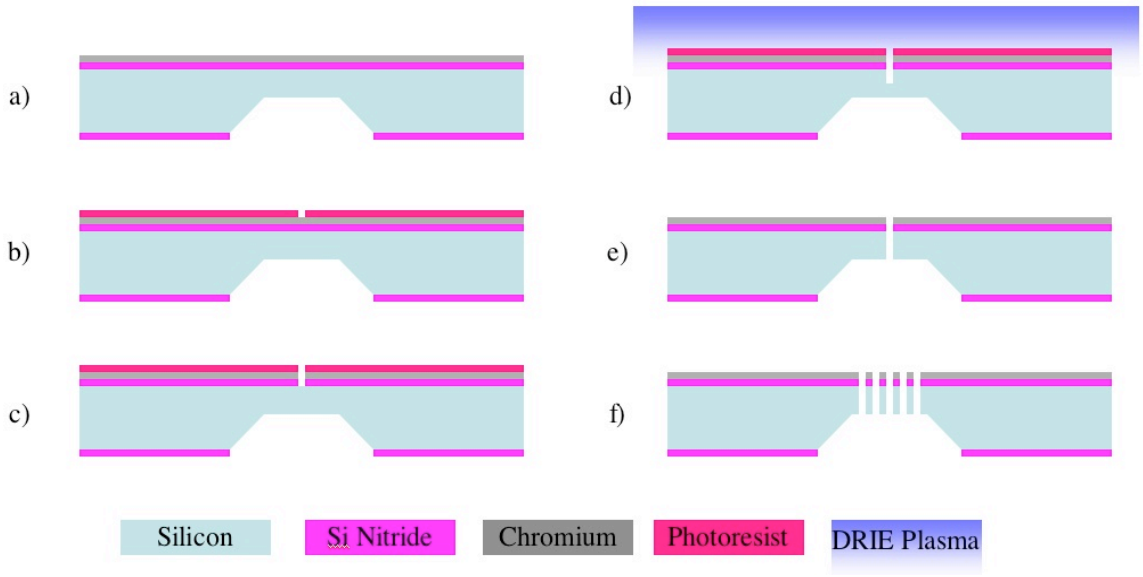

Figure 5.1: Schematic, cross sectional view of DRIE process using a chromium etch mask. a) Silicon Nitride wafer following KOH etching of backside is coated with a 2000A Cr layer. b) Photoresist coating and pattern formation. c) Profile after etching of Cr layer via chrome etch and of silicon nitride via RIE. d) DRIE of exposed silicon layer e) Wafer after completion of DRIE; holes etch completely through the silicon layer, photoresist may be completely consumed after extensive etching. f) The silicon gate mesh is produced following the same DRIE process only using a different photolithography pattern.

The chromium etch mask proved to be somewhat reliable although in some cases chromium layer adhesion loss during the DRIE process affected the device outcome. These failures may have been affected by the lack of wafer cleanliness. Standard cleaning and drying methods in our facilities are more rudimentary and leave open more possibility for contamination.

5.2.2.2 KMPR Photoresist Etch Mask Process

For the fabrication of the multi-slit structure an initial attempt was made to form a chromium etch mask, but after etching in DRIE this mask showed the above mentioned adhesion loss resulting in extreme broadening of the slit width. The slit was designed at approximately 10um, but after Cr etch mask adhesion loss the slit width etched into the substrate was closer to 40um.

As a result of this failure an alternate DRIE masking material was used. Microchem company's KMPR 1010 photoresist was used to form the etch mask. KMPR is a negative, resin-based photoresist which has particularly high performance for DRIE applications. Typical postive photoresists have lower selectivities of 15:1 or 20:1 when undergoing RIE or DRIE. KMPR can exhibit etch selectivities as high as 100:1, allowing for deep etching into the silicon using only 1-10 um of photoresist. Also other available photoresists are limited to coating thicknesses of 2-3 um. Additionally KMPR lithography produces highly vertical lithography sidewalls, because of its highly transparent nature, allowing for greater fidelity in pattern transfer during the etch.

In this case KMPR 1010 photoresist was diluted with Microchem's SU-8 2000 thinner to reduce the solids concentration to a level similar to that of KMPR 1005. KMPR 1010 typically spin coats a nominal 10 um layer at 3000 rpm spin speeds, while KMPR 1005 form an approximately 5 um layer. The amount of additional solvent needed was calculated to be around 20% by volume; therefore approximately 8 ml of thinner was added to 40 ml of KMPR 1010.

The KMPR 1005 photoresist mixture was then spin coated onto the silicon substrate at 3000 rpm for 30 s and soft baked for 5 min at 100C. Subsequently the sample and mask features were aligned and exposed with a 20 s dose of about 240 mJ and given a post exposure bake of 100 C for 2 min. The sample was then developed in Microposit's CD26 developer, an aqueous solution with 2.4% Tetramethylammonium hydroxide, for 3 min with moderate agitation. Inspection of the film after development showed a relatively defect free surface and an estimated film thickness of 7 um, a more than adequate thickness of KMPR assuming moderate etch selectivity.

The KMPR process was similar to the chromium etch mask process shown in Figure 5.1. The Cr deposition, lithography, and etching of Cr and silicon nitride steps in a), b), and c) were replaced with the spin coating, exposure, and development of KMPR, along with an etching of the silicon nitride layer. The substrate then was placed in the DRIE with an outcome similar to f) except free of the Cr layer.

5.2.3 Through wafer etching

The etch through the silicon layer remaining after the KOH was accomplished using an ALCATEL DRIE system. The silicon was etched using either the S1813 photoresist/chromium etch mask or the KMPR photoresist etch mask described above, depending on the substrate. When properly processed each layer provided adequate etch protection with only minimal mask adhesion failure.

The standard Bosch type process was used for these etches. The Bosch process is a two step etch process. The first step is an etch step in which SF_6 gas is flowed into the chamber, ionized in the plasma, and used to etch the exposed silicon. Because of the high bias voltage the ions have a high degree of vertical impact on the substrate accounting for the high aspect ratio capability of the etch. In the second step C_4F_8 gas is flowed into the chamber and via the plasma is polymerized and deposited uniformly onto the substrate surfaces, including the vertical surfaces formed during the previous etch steps. This deposition protects the vertical sidewalls preventing lateral etching of the silicon, allowing the etch to maintain a high aspect ratio sidewall. In this particular case the SF_6 etch and C_3F_8 deposition steps are 7 seconds and 2 seconds respectively.

5.2.3.1 Arrayed Gate Mesh Electrode

The first device etched was an arrayed gate mesh electrode to match the 5x5 CNT cathode array chip. Normally a tungsten 100 mesh was used as the gate electrode for the 5 x 5 CNT cathode array. The mesh structure is made of wires interwoven at right angles so it does not present a perfectly flat surface over the cathode. Also it is a more flexible material and can deform or bow causing greater height discrepancies between adjacent cathodes. This was observed in one case with the mesh bowed down over one side of the cathodes possibly affecting the responses of the cathodes to the gate voltage. The silicon mesh structure allows one to form a much more uniform surface to place over the cathodes, and it is not as susceptible to deformation. Similar devices have been etched using DRIE[1] but using somewhat different processes.

The wafer was etched first by KOH to a depth of 280 um and then via DRIE using the sputtered chromium etch mask. The pattern for the gate mesh is shown in Figure 5.2(a). The wafer was etched via DRIE for 15 min and removed. The etch depth was measured at an average value of 55 um, yielding an etch rate of just under ~3.7 um/min. The wafer was then etched for an additional 20 min and removed. Partial breakthrough of the silicon was observed as seen in Figure 5.2(b). The wafer was then etched for several additional 3 min intervals to attempt to complete the etch.

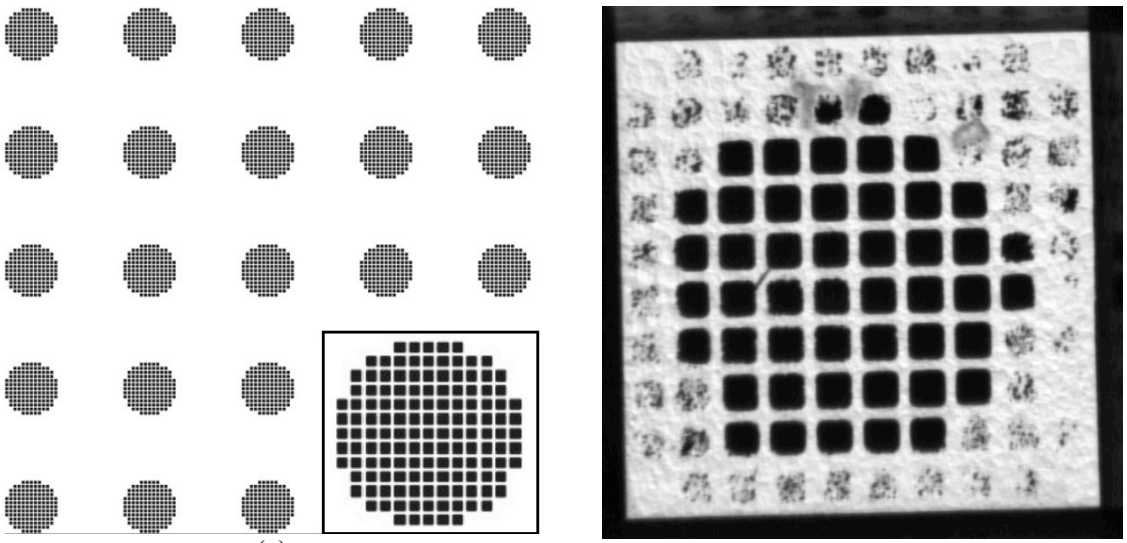

(a) (b)

Figure 5.2: (a) 5x5 gate mesh array mask pattern and magnification of a the mesh for one pixel (inset image). (b) Optical microscope image of partially etched silicon layer from the backside of the chip, with holes near the edges not yet completely etched.

Each quadrant of the wafer contained a 5x5 gate mesh array (a 3x4 portion of the gate array is seen in Figure 5.3(a)), and some quadrants of the wafer saw nearly complete etching on each mesh. Others did not demonstrate complete etching because of process problems encountered. In order to avoid etchant attack on the wafer chuck with through wafer etching the wafer was mounted to a silicon backing wafer. Fomblin oil was used to provide adhesion between the device and backing wafer. When the etch broke through the silicon some of the Fomblin oil bubbled through open parts of the mesh and contaminated areas not yet completely etched, effectively terminating the etch in those areas. And in another area of the wafer incomplete removal of contaminants blocked the etch. This accounts for some of the etch defects encountered. To overcome the problem of incomplete etching on successive runs Kapton tape was used to attach the wafers or wafer pieces to backing wafers in lieu of Fomblin oil. The Fomblin was used for its purportedly better thermal contact, but the Kapton tape provided a reasonable alternative.

Nevertheless some areas saw complete etching over the entire quadrant, resulting in a fully realized 5x5 array gate mesh electrode. Having etched away 280 um of Si thickness in the KOH a remaining silicon thickness of ~120 um was measured as seen in Figure 5.3(c), demonstrating strong process control using this method.

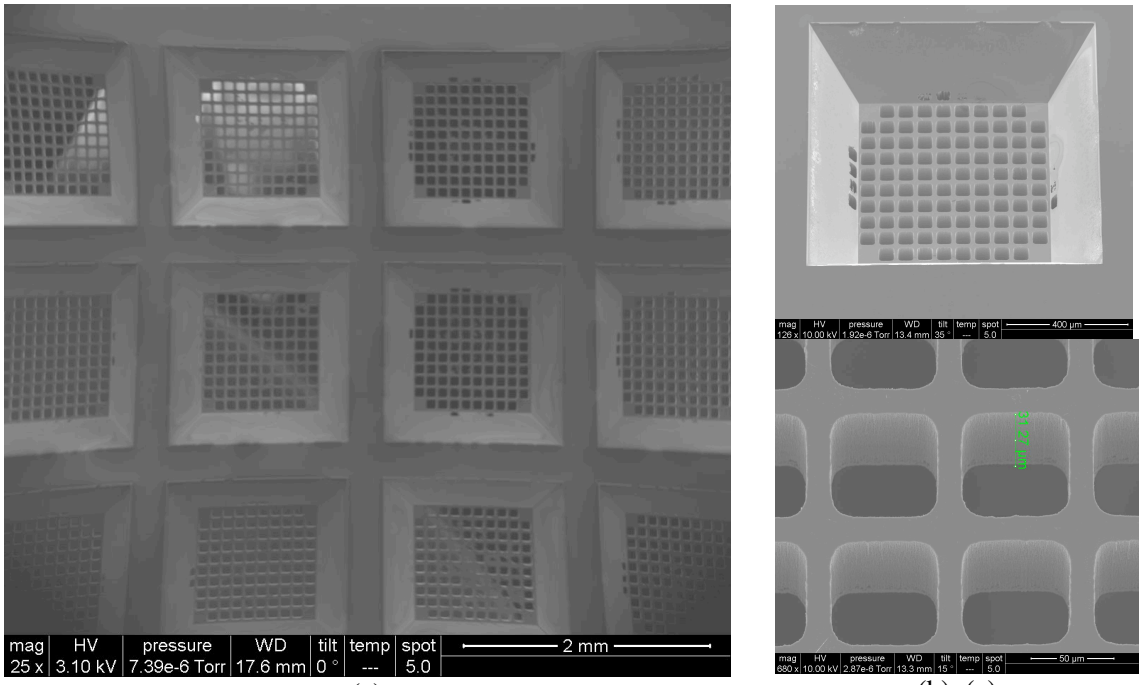

(a) (b), (c)

Figure 5.3: (a) SEM image overview of a 3x4 area of the 5x5 matrix of the gate mesh array. (b) SEM image of a tilted single gate mesh showing the area etched via KOH and a fully etched mesh. (c) Higher mag SEM image of the gate mesh tilted to show the sidewall of the etched holes; the depth is measured to be ~31.3 um with a tilt angle of 15°, the actual depth and the thickness of the remaining Si layer is 121 um.

Because we were only able to perform this fabrication process once as a result of time constraints no optimization of the design of the silicon mesh was possible. However the structure represents the best first effort towards a custom gate structure. As mentioned the surface of this microfabricated mesh is extremely flat when compared with the tungsten mesh, and this provided one rationale for this method. In addition to this flatness the initial design attempted to maximize open area, achieve mechanical stability, and present a uniform

electric field over the cathode. In this case the design values were for 20 um beams with 60 um square holes. Given certain process biases the final dimensions as measured by SEM were ~15 um beams and ~ 65 um square holes. The as drawn open area would have amounted to 56%, but after the process bias that value was increased to 66%. As for mechanical stability the mesh structure appears adequately rigid. None of the beams were observed to break, although given their short spans as compared with their thickness this would have been unlikely. As a precaution against beam breakage or cleaving the corner of the square holes were filleted. Finally the relatively small size of the squares along with the regularly spaced and even beams should provide for a more uniform electric field than the tungsten mesh used, although part of this is achieved via loss of open area and consequently potential loss of electron flux to the anode. Given the fabrication of these and other components via DRIE near the end of the project field emission testing experiments were not completed. Nevertheless this technique demonstrates the capability of making custom mesh structures and patterns, which could be designed for special cathode shapes or cathode arrays in the future. Additionally custom patterns may be useful for optimizing electron beam focusing or transmission rates.

5.2.3.2 DRIE High Aspect Ratio Electron Collimator

Another area of potential improvement pursued is that of developing a better collimator for the electron beam. As seen in Chapter 4 the electron beam is prone to scattering and registers in the radiochromic film as much larger than the window size. In the multi-pixel case higher aspect ratio collimation using thinner pieces of silicon should better eliminate pixel-to-pixel cross talk as compared with the double-stacked KOH etched collimator. Also for any increase in the array density of pixels it will be insufficient to rely

on KOH etching techniques as the minimum spacing between pixels is much higher as compared to the use of DRIE methods. We therefore wanted to demonstrate high aspect ratio etching of small holes in the range of 10 um.

In this case two different samples were etched via the Bosch process. The first was a 500 um thick silicon nitride wafer, without the KOH processing steps previously performed. This wafer functioned as a test wafer to confirm and quantify the deep etching capabilities; it would also serve as a sacrificial sample to obtain cross-sectional images and data. For this wafer a chromium mask was formed with approximately fifteen 10 um holes per site. The wafer was etched for a total of 120 min, and then cross-sectioned to obtain profile views of the 10 um holes. An etch depth of 167 um was obtained with similar depths seen for other holes (Figure 5.4). The profile lacked complete verticality, but nonetheless demonstrated the desired effect.

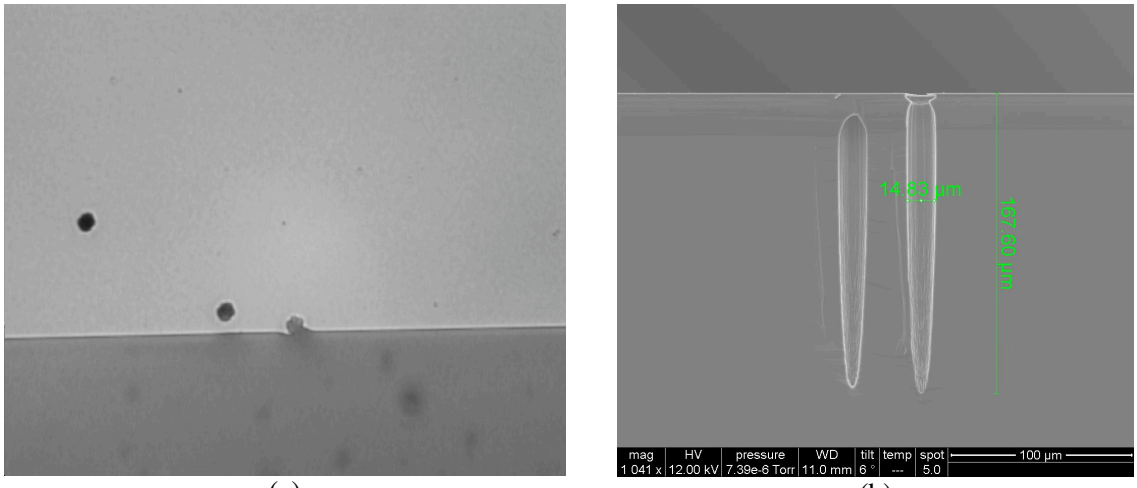

(a) (b)

Figure 5.4: (a) Top down, optical microscope view of cross section of wafer along 10 um holes. (b) SEM view of cross-sectioned wafer showing a pair of etch holes with a depth of 167.6 um. The width of this sample is 14.8 um at it's widest point, and shows some non-uniformity along the depth of the etch.

For the second sample in the collimator etch process a wafer that had been etched via KOH to a depth of ~240um was patterned in this case using the KMPR etch mask process.

The wafer was etched with DRIE for approximately 100 min, and a complete 5x5 array of collimator holes was produced. The hole size of 10um was not perfectly transferred throughout the full thickness of the etch, rather the etch profile is likely similar to that in Figure 5.4(b). This wafer was not cross-sectioned but images of the upper and lower surfaces of the holes were obtained along with an image of light transmitted through the etch holes. The top side and bottom side holes are approximately 10 um and 4 um respectively (Figure 5.5).

Hopefully samples such as these can be used as collimators with the current system or at minimum serve as an example of a first effort at better microbeam collimation. While some of the electron beam enlargement is unavoidable as a result of electron scattering, techniques like this may play a critical role in the straightforward fabrication of collimators of small diameter and high aspect ratio. From study and interpretation of the simulation data these two factors appear to provide the most hope for decrease in beam diameters outside of the more speculative approach of altering the beam energy.

5.2.4 Potential Process Improvements

A variety of improvements could be made to the etch processes and structures discussed here. Equipment, facilities, time, and cost were limited such that some problems in the process were observed. Photoresist and metal layer adhesion problems occurred necessitating reworks and switching over to the KMPR process. Also the photolithography exposure mask used was a printed silver mask on Mylar with limited resolution. The use of a conventional chrome on glass exposure mask with smaller feature write sizes would have

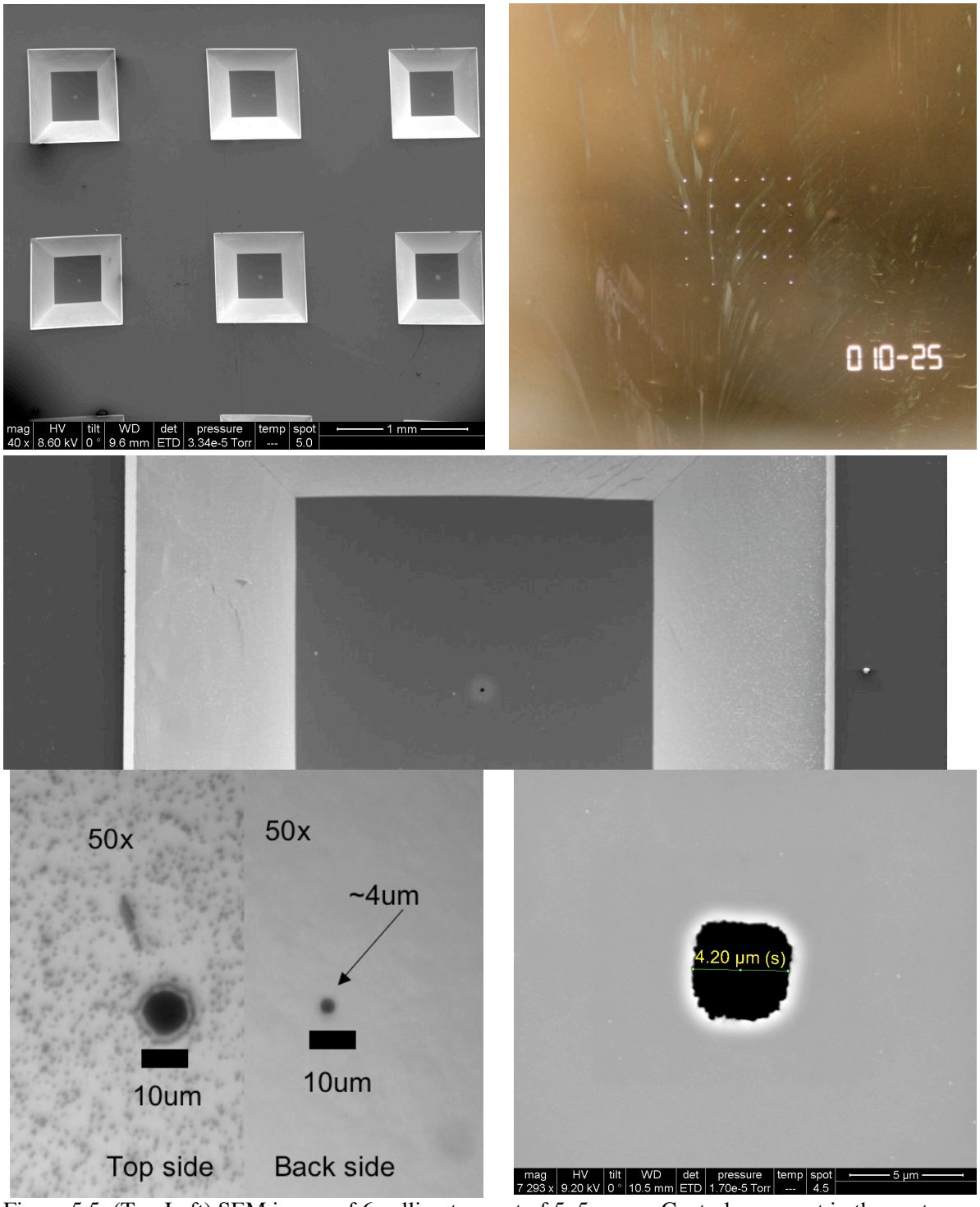

Figure 5.5: (Top Left) SEM image of 6 collimators out of 5x5 array. Central gray spot in the center of the KOH etch area is evidence of through etched DRIE hole. (Top Right) Photo of full 5x5 hole array illuminated from behind. (Middle) Higher mag SEM image showing centered etch hole. (Bottom Left) Optical images of top side and back side holes ~12 um and ~4 um respectively. (Bottom Right) SEM image of back side hole with 4.2 um diameter and somewhat irregular shape following DRIE.

allowed for better feature definition. The limitations of resolution are visible in the edges and sidewalls of the etch structures where protrusions and unevenness are visible.

As completed, this process requires two different etch steps, one with KOH and one with DRIE. By using thinner wafers the process could be completed with only DRIE, since the main purpose of the KOH etch is to thin the wafers in certain areas to facilitate a reasonable through wafer etch with the DRIE. For small feature sizes and for the gate mesh electrode structure the thickness of 150um was appropriate. A much thicker Si layer would cause the ~10 um holes to etch more poorly at greater depths. In the case of the gate mesh electrode the greater thickness would result in a lower electron transmission rate given non-orthogonal electron trajectories from the cathode.

The KOH processing could also be avoided by instead performing a DRIE from the backside of the wafer, eliminating the need for a wafer with a silicon nitride layer. While this process could be done on a standard silicon wafer, a silicon-on-insulator (SOI) wafer would be a more efficient method (Figure 5.6). SOI wafers consist of a silicon wafer with a grown silicon oxide layer on both sides. Next another wafer is bonded to the top surface of the wafer and the wafers are annealed to finalize the bond. This top layer is then polished back to a predefined thickness, ranging from a few to tens of microns thick with high uniformity. The wafer then has three main layers the silicon device layer (~ 5-100 um), the buried oxide layer (~1-3um), and the silicon handle wafer (e.g. 400-500 um). When these wafers are used in DRIE the backside and frontside can essentially be etched independently. When etching from either side of the wafer through the silicon with DRIE the etch eventually removes the silicon and exposes the buried oxide. The oxide has a very low etch rate with the DRIE etch chemistry so it functions as an etch stop layer, allowing all the devices to

maintain the same thickness and avoiding etching into the underlying silicon. This can be done from both sides of course. After etching is complete the buried oxide layer in between the device and handle silicon can be etched away in aqueous or vapor phase hydrofluoric acid, for example. A proposed process flow is depicted in Figure 5.6.

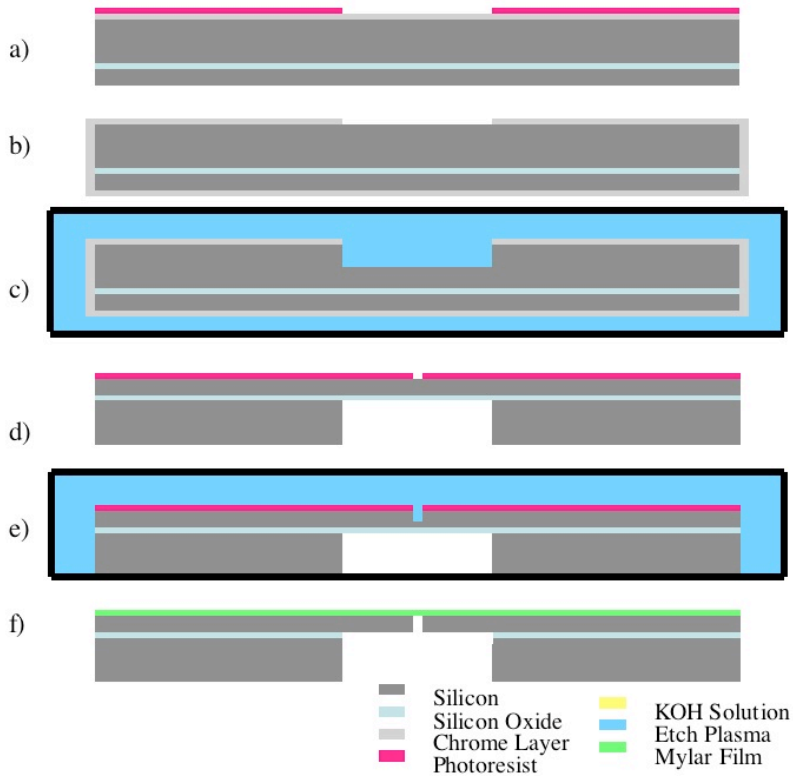

Figure 5.6: Collimator Fabrication Process based on SOI wafer. a) Sputter backside w/Cr and pattern via lithography. b) Sputter substrate front with Cr. c) DRIE of backside silicon. d) Remove Cr, flip, and frontside lithography. e) DRIE of device silicon f) HF removal of oxide and attach Mylar.

5.3 Double Slit Irradiation

Another area of investigation to which we have applied the UNC cellular irradiator is to its possible use in studying microbeam radiation therapy. In this case the irradiator would not be used for irradiation of a single cell or cluster of cells but rather irradiation of plated cells or even thin tissues via narrow slits.

5.3.1 Background

Some interest has been shown in the irradiation of tissues, in this case via X-ray in a mouse model, via two orthogonal, interleaved arrays of slit beams [2] as seen in Figure 5.7. In this case it is hoped that the irradiation of cells via thin slits will accomplish two things. First by having a high peak to valley dose ratio certain layers of tissue are heavily irradiated while adjacent layers see very low dose. Endothelial cells from areas seeing low dose can migrate into the damaged layers while the overlapping layers of radiation cause damage to

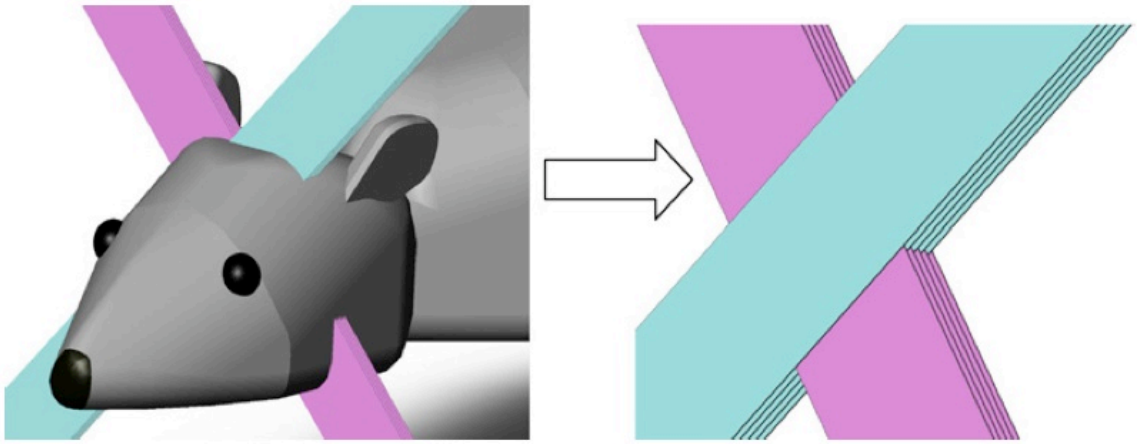

(a)

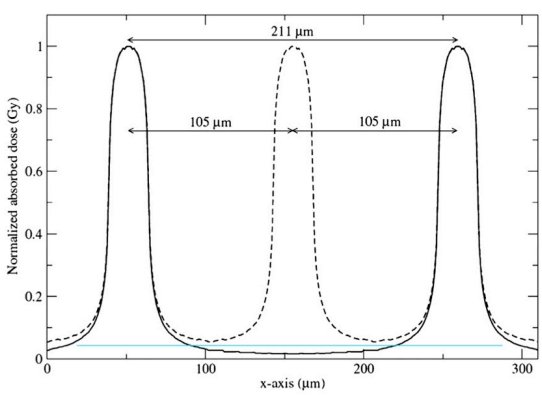

(b)

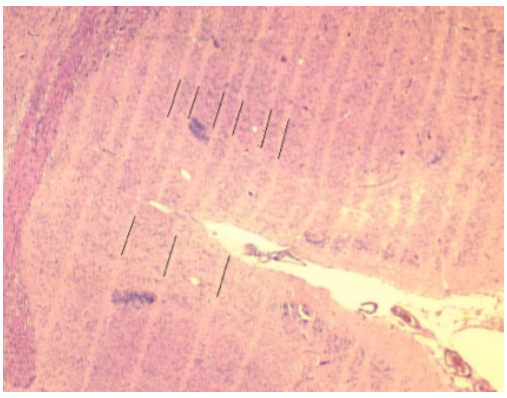

(c)

Figure 5.7: (a) Schematic of orthogonal interleaved slit array irradiation of mouse brain. (b) Graph of normalized dose deposition for single beam array (solid line) and interleaved beam arrays (dashed line). (c) Mouse brain tissue slice 3 wks post treatment showing lines of irradiation. Reproduced from reference[2].

the vasculature. Electron slit irradiation studies could serve as a complement or precursor to X-ray slit irradiation studies.

5.3.2 Slit Aperture Design and Results

To investigate the electron cell irradiator's capabilities for slit irradiation a double slit aperture was constructed through which cell monolayers could be irradiated. A laser drilled double slit in stainless steel foil was used to prepare the aperture. Mylar was attached to the top surface to form a window and vacuum seal the aperture, while the foil was glued to the mini-flange with silver epoxy, as seen in Figure 5.8. The slits were 2 mm long by 5 um wide and were separated by a 250 um gap.

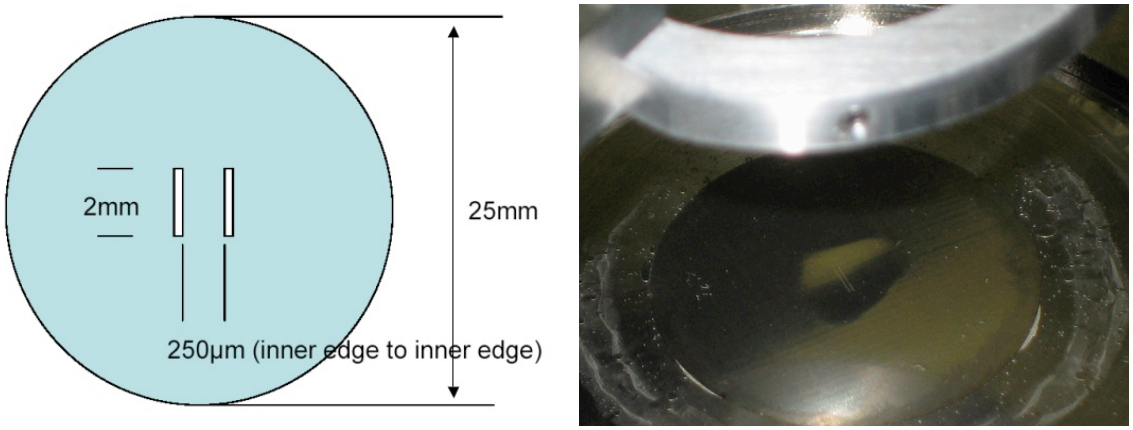

Figure 5.8: (Left) Schematic of double slit aperture in stainless steel foil. (Right) The double slit mounted to the irradiation flange, with a slight depression in the foil around the slit.

As a first test of its collimation capabilities the slit was used to irradiate radiochromic film. The irradiator was set up for a 30 kV acceleration voltage, 100 Hz pulse frequency, a 1 ms pulse width, and a ~3.5 uA beam current. The film was irradiated in eight locations with pulse counts of 200, 100, 50, 20, 10, 5, 2, and 1 pulse. The film was scanned and analyzed to find the deposited dose as seen in Figure 5.9. The 50 pulse pair of lines was chosen as it was unsaturated and yet adequately exposed to measure the peak the valley ratio.

The film data confirm a large peak to valley ratio capability using electron irradiation in conjunction with the 250 um spaced double slit collimator. A peak to valley ratio of 25:1 was obtained when the lower peak was compared with the minimum valley dose; the ratio

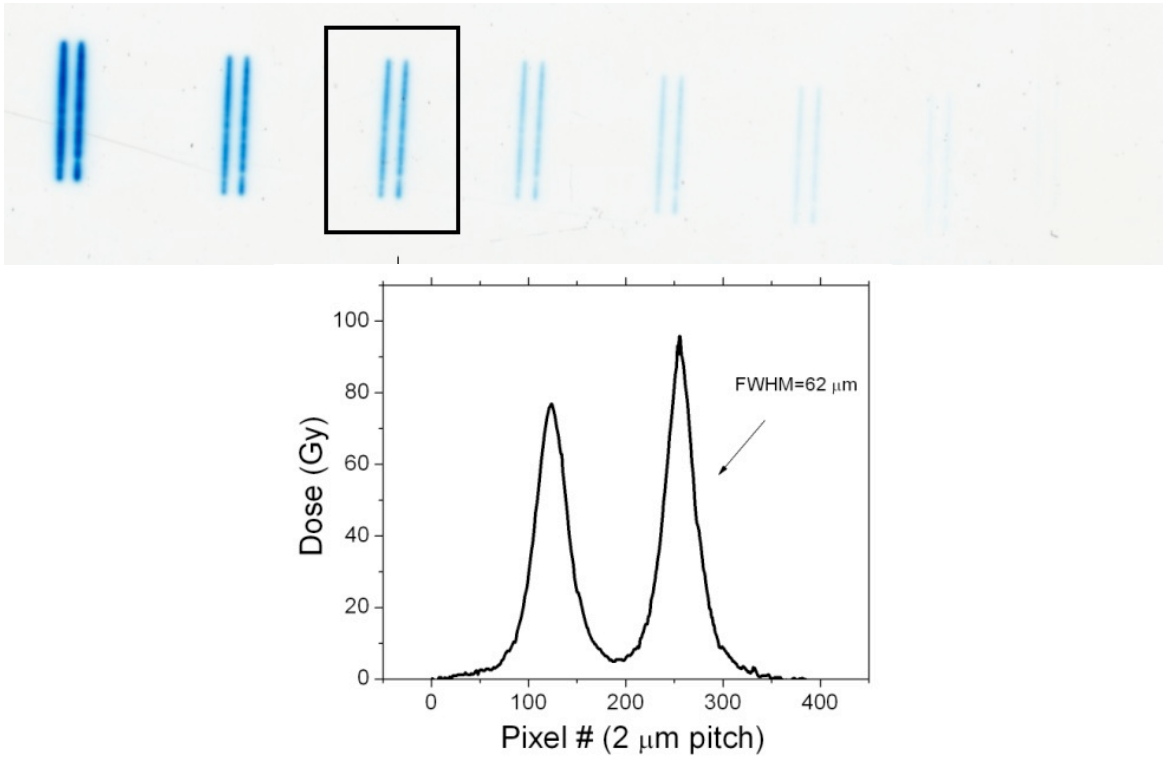

Figure 5.9: (Top) Scanned image of radiochromic film after electron exposure for from left to right: 200, 100, 50, 20, 10, 5, 2, and 1 ms pulses. (Bottom) Cross-sectional analysis of the dose distribution from the 50 pulse line pair, showing a minimum peak to valley ratio of 25:1.

would be slightly higher when using the higher dose peak.

The double slit was next used for cell irradiation to observe the biological irradiation capability. A cell monolayer was irradiated with the electron equivalent of 12 Gy calibrated from the radiochromic film. DNA double strand breaks were once again visualized via γ-H2AX, and multiple microscope images were compiled together to form a composite image (Figure 5.10). The image was evaluated for evidence of a bystander effect, but general agreement about the presence of a bystander effect was not reached. Unlike the film data two separate lines were not visible, but instead the fluorescence observed produced a large

rectangular area of apparent cell damage. In the film irradiation each peak had a FWHM of approximately 80 um, but in the case of the fluorescence no clear evidence can be seen of two separate peaks. By superimposing the expected locations of the slits over the image an argument could be made that some type of bystander effect is present in that the area of fluorescence extends between and on either side of the lines while the film irradiation so clearly shows two distinct irradiation areas. Also the maximum distance from the slit at which fluorescence is observed is on the order of 150 um or more. This extends far beyond the scattering distances observed in our small window experiments. On the other hand this may merely be the fluorescent evidence of a beam scattering effect. Therefore it was difficult to distinguish or prove a bystander effect as opposed to a general scattering effect, especially given the limited data on what fluorescent intensity to expect from various irradiation doses.

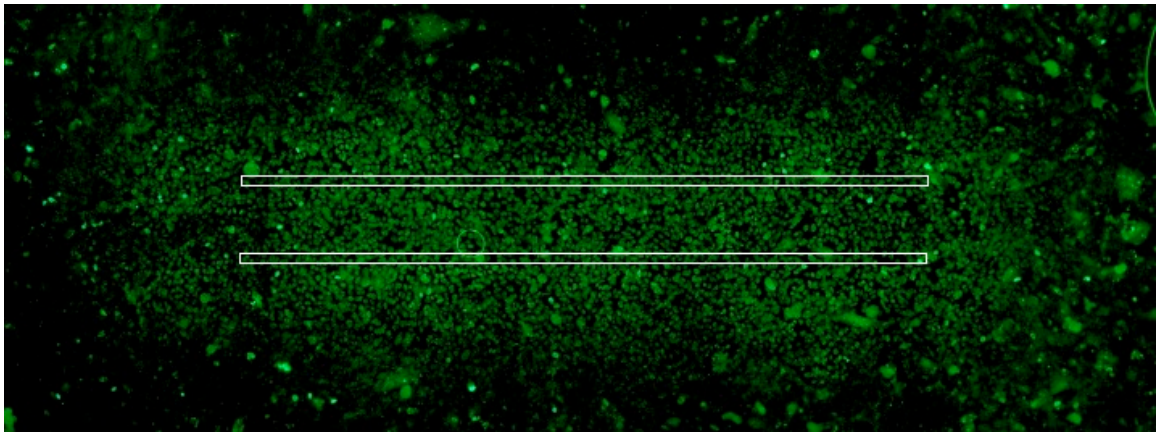

Figure 5.10: Composite image of γ-H2AX fluorescence following 12 Gy irradiation of cell monolayer via a pair of 5 um wide slits. The slits are 2mm long and spaced apart by 250 um. The white rectangles indicate the approximate locations of the slits.

5.3.3 DRIE Slit Aperture Fabrication

Given the interesting data obtained from the double slit irradiation and the desire to distinguish the slit beams from one another in a cell irradiation experiment and perhaps further investigate the presence of a bystander effect it was desirable to fabricate some alternate slit beams. Wanting to be able to test multiple slit array structures a wafer design was fabricated with three different designs with one of the designs appearing in two wafer quadrants. All of the designs consisted of slits ~ 1.2 mm long and 10 um wide. One design consisted of slit pairs in a 3x2 array with a 3 mm spacing between each slit pair; the spacings between the slit pairs in the array were 250, 400, 500, 600, 750, and 1000 um. Another design consisted of a similar 3x1 array with 250, 500, and 750 um spacings. The final design consisted of an array of 7 slits spaced successively by 250, 400, 500, 600, 750, and 1000 um. The first two designs of the paired slits were partially driven by the need to align paired slits to cathodes in the multi-pixel cathode array. The final design was centered on the chip so as to be used with the multi-pixel or single pixel irradiator. Particularly the first and last design were chosen to provide an increasingly wider range of slit pairs so as to determine the spacing at which separate peaks could be resolved in the fluorescence of the cell irradiation experiments. Given the fluorescence observed at a distance of 150 um or more from the slit the range of spacings, particularly in the first and last design, were designed to provide a full spectrum of irradiation peak interaction data from complete overlap to partial overlap, minimal valley dosage, and finally complete separation.

Two wafers intended for this purpose were started in the fabrication process, but unfortunately one was completely overetched in the DRIE as the result of a chromium mask failure. This resulted in the slit structures being etched to ~ 50 um wide while the wafer was

etched to an unusable thickness. The second wafer was damaged in a spin coater as a result of the wafer fracturing along the KOH etch trenches during high spin speed. One quadrant of the wafer survived, that being the third design. For this reason only a single collimator chip was able to complete the fabrication process. This new collimator is composed of the array of seven 10 um wide slits in an approximately 150 um thick silicon layer using the KOH and DRIE fabrication techniques described earlier in developing the gate mesh and the 10 um hole collimators. The slits in this design are ~1.2 mm long and have the successive 250, 400, 500, 600, 750, and 1000 um spacing. After the DRIE process the slits are ~10 um on the top side, but as a consequence of the etch process the slits are enlarged to almost 20 um on the backside. Figure 5.11 presents images of the new collimator pattern as well as metrology of the DRIE slits themselves.

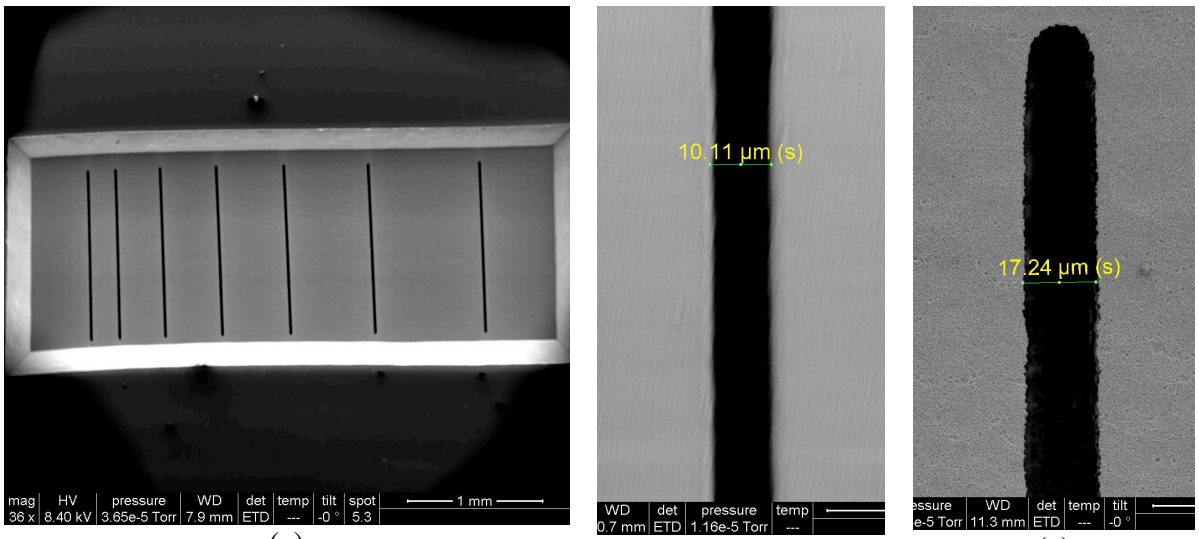

(a) (b) (c)

Figure 5.11: (a) SEM overview from the backside of the multi-slit (7 slit) collimator with successively increasing spacing, from 250 um to 1 mm. (b) SEM view from the topside of the wafer showing a 10.1 um slit width. (c) SEM view of the backside of the wafer showing a 17.2 um width, slightly enlarged following the DRIE process.

This new collimator will allow for simultaneous irradiation over several slits with increasing spacings. This should allow for the differentiation of two peaks in the cell

irradiation experiment and for the evaluation of the peak to valley response ratio at different slit spacings. This could lead to future experiments in which the effect on a cell monolayer of slit irradiation can be further investigated as well as the fabrication of a future round of custom slit collimators.

5.4 Summary and Conclusions

In conclusion we have constructed a novel CNT field emission based electron cellular irradiator. The system comprises a wide variety of components, and in particular has required the development of a CNT cathode. A first phase single microbeam has been developed, characterized, and used for a variety of cell irradiation procedures. The single beam system is capable of irradiating over very small areas (23 um diameter) and even single cells given adequate cell spacing. Better collimation techniques could produce slight enhancement of the current capability. Nevertheless given the scattering of electrons even out of small apertures there seem to be some fundamental limitations to the minimum beam size capability of electron irradiators operating in the 25-30 kV range. Despite these limitations the single pixel electron irradiator has demonstrated a high dynamic dose rate range, allowing for fast irradiation over several orders of dose magnitude. Additionally the system could be easily reproduced and installed for use more broadly than other types of irradiators.

For cell irradiation in general there is still much work to be done, both in biological experimentation and in determining what experiments to carry out. The presence of an irradiation bystander effect remains to be evaluated as evidence is present in some cases and not in others. It is not known whether the bystander response is merely an occasional

response to irradiation by some types of cells or whether it is merely an elusive effect. The UNC cell irradiator provides a demonstration of increased access to cell irradiation which could help elucidate some of the unknown inner workings of cells.

In addition to the achievements with the single pixel system and the potential contribution to research in radiobiology, the work done on the multi-pixel system has demonstrated the basis for a functioning multi beam system, a first in the microbeam research community. Although the current multi-beam system does not surpass the capabilities of many of the more advanced cell irradiators, particularly the ion beam systems, the introduction of a multi-beam system and the research completed have laid the groundwork for new types of experiments exploiting the multi-beam platform. This system introduces the capability of multiple parallel irradiations with dose and dose rate variability. Also future improvements could include the expansion of the system to an even larger number of beams, e.g. 10x10 or even 100x100. The engineering of the system still requires some improvement, but many of the basic challenges and requirements have been identified that will need to be overcome for a future system.

Finally over the course of the research and development of our microbeam systems other opportunities and avenues have been investigated as related to cell irradiation and fabrication of key components. While the single cell and even sub-cellular irradiation capabilities will remain in demand, the use of alternative radiation geometries, such as large apertures and slit irradiation, may also prove to be of interest. In addition new fabrication and engineering techniques, such as the DRIE-based components, can serve to advance the performance of various types of cellular irradiators. There is still a great amount of knowledge to be gained about cellular radiation response and a great need for radiation

therapy advances that will enhance the effectiveness of cancer treatment. The CNT field emission based electron cellular irradiator represents one step in that direction.

References

1. D. Modroukas, V. Modi, and L.G. Frechette, *Micromachined silicon structures for free-convection PEM fuel cells*. Journal of Micromechanics and Microengineering, 2005. **15**: p. S193-S201.

2. E. Brauer-Krisch, et al., *New irradiation geometry for microbeam radiation therapy*. Physics in Medicine and Biology, 2005. **50**: p. 3103-3111.

Publication List

Refereed Articles

1. **D. Bordelon**, J. Zhang, S. Graboski, A. Cox , E. Schreiber , O. Zhou , S. Chang. "A Nanotube Based Electron Microbeam Cellular Irradiator for Radiobiology Research." Rev. Sci. Instrum. 79, 125102 (2008).

2. Z. Liu, G. Yang, Y.Z. Lee, **D. Bordelon**, J.P. Lu, and O. Zhou. "Carbon Nanotube Based Micro-Focus Field Emission X-ray Source for Micro-Computed Tomography." Applied Physics Letters 89, 103111 (Sept 2006).

3. S. Chang, J. Zhang, **D. Bordelon**, E. Schreiber, A. Cox, and O. Zhou. "Development of a nanotechnology based low LET multi-microbeam array single cell irradiation system." Radiation Protection Dosimetry, 122(1-4), 323-326, 2006.

Abstracts

1. J. Zhang, **D. Bordelon**, J. Snider, E. Schreiber, A. Cox, O. Zhou, and S. Chang. "Feasibility Study of Microbeam Radiation Therapy Using a Carbon Nanotube Field Emission Based Electron Microbeam Irradiator." Medical Physics, 36(6): 2775-2775, 2009.

2. **D. Bordelon**, J. Zhang, S. Graboski, A. Cox, E. Schreiber, O. Zhou, and S. Chang. "Development of a carbon-nanotube field emission based multi-pixel microbeam cellular irradiation system." Medical Physics**,** 35(6): 2899, 2008

3. S. Chang, J. Zhang, **D. Bordelon**, S. Graboski, E. Schreiber, A. Cox, and O. Zhou. "Feasibility Study of a Carbon Nanotube Field Emission Microbeam System for Cellular Irradiation." Med. Phys. 34, 2455 (June 2007)

4. S. Chang, J. Zhang, **D. Bordelon**, E. Schreiber, A. Cox, O. Zhou. "Development of a carbon nanotube based low -LET multi-pixel microbeam array." Rad. Res 166, 658-659 (2006).

5. S. Chang, J. Zhang, **D. Bordelon**, E. Schrieber, A. Cox, O. Zhou. "A carbon nanotube based low LET multi-microbeam array singel cell irradiation system." Medical Physics (6): 2271, (June 2006)

Selected conference presentations

1. **D. Bordelon**, J. Zhang, S..Graboski, A. Cox, E. Schreiber, O. Zhou, and S. Chang. "Development of a carbon-nanotube field emission based multi-pixel microbeam cellular irradiation system"; The American Association of Physicists in Medicine (AAPM) 50th Annual Meeting, Houston, TX July 2008. (oral presentation)

2. **D. Bordelon**, J. Zhang, S. Graboski, E. Schreiber, A. Cox, O. Zhou, and S. Chang. "Development of carbon nanotube field emission multi-pixel electron beam cellular irradiation system"; The 8th International Workshop on Microbeam Probes of Cellular Radiation Response, Chiba, Japan, November 2008 (oral presentation)

3. S. Chang, J. Zhang, **D. Bordelon**, S. Graboski, E. Schreiber, A. Cox, and O. Zhou. "Feasibility study of a carbon nanotube field emission microbeam system for cellular irradiation"; The American Association of Physicists in Medicine (AAPM) 49th Annual Meeting, Minneapolis, Minnesota, July 2007. (poster)

4. J. Zhang, **D. Bordelon**, S. Graboski, E. Schreiber, A. Cox, O. Zhou, and S. Chang. "Development of a nanotechnology based low LET multi-microbeam array single cell irradiation system"; CCNE 2007 Cancer Nanotechnology Symposium, Chapel Hill, NC, November 2007. (poster)

5. J. Zhang, **D. Bordelon**, S. Graboski, E. Schreiber, A. Cox, O. Zhou, and S. Chang. "Development of a nanotechnology based low LET multi-microbeam array single cell irradiation system"; Materials Research Society (MRS), North Carolina Symposium, November 2006. (poster)

6. J. Zhang, **D. Bordelon**, S. Graboski, E. Schreiber, A. Cox, O. Zhou, and S. Chang. "Development of a nanotechnology based low LET multi-microbeam array single cell irradiation system"; CCNE 2006 Cancer Nanotechnology Symposium, Chapel Hill, NC, November 2006. (poster)

7. S. Chang, J. Zhang, **D. Bordelon**, E. Schreiber, A. Cox, and O. Zhou. "Development of a carbon nanotube based low LET multi-pixel microbeam array"; 7th International Workshop on Microbeam Probes of Cellular Radiation Response, New York City, New York, March 2006. (oral presentation)

8. S. Chang, J. Zhang, **D. Bordelon**, E. Schreiber, A. Cox, and O. Zhou. "Development of a nanotechnology based low LET multi-microbeam array single cell irradiation system"; 14th International Symposium on Microdosimetry, Venice, Italy, November 2005. (oral presentation)